



PON Ricerca e
2014- 2020 **Innovazione**



Ministero dell'Istruzione, dell'Università e della Ricerca

Dottorato di Ricerca in Ingegneria dei Prodotti e dei Processi Industriali

XXX cycle



Università degli Studi di Napoli Federico II

Scuola Politecnica e delle Scienze di Base

**Dipartimento di Ingegneria Chimica, dei Materiali e della Produzione
Industriale**

**NUCLEATION AND CHARACTERIZATION OF
COMBUSTION-GENERATED NANOPARTICLES:
A MOLECULAR DYNAMICS APPROACH**

By

Laura Pascazio

Supervisor:

Prof. Andrea D'Anna

Coordinator:

Prof. Giuseppe Mensitieri

Academic Year 2017/2018

UNIVERSITÀ DEGLI STUDI DI NAPOLI FEDERICO II

Dottorato di Ricerca in Ingegneria dei Prodotti e dei Processi Industriali

Date: December 2017

Author: Laura Pascazio

Title: Nucleation and characterization of combustion-generated nanoparticles: a molecular dynamics approach.

Department: Dipartimento di Ingegneria Chimica, dei Materiali e della Produzione Industriale

Degree: Philosophiae Doctor

Permission is herewith granted to university to circulate and to have copied for non-commercial purposes, at its discretion, the above title upon the request of individuals or institutions.



Signature of Author

THE AUTHOR RESERVES OTHER PUBLICATION RIGHTS, AND NEITHER THE THESIS NOR EXTENSIVE EXTRACTS FROM IT MAY BE PRINTED OR OTHERWISE REPRODUCED WITHOUT THE AUTHOR'S WRITTEN PERMISSION.

THE AUTHOR ATTESTS THAT PERMISSION HAS BEEN OBTAINED FOR THE USE OF ANY COPYRIGHTED MATERIAL APPEARING IN THIS THESIS (OTHER THAN BRIEF EXCERPTS REQUIRING ONLY PROPER ACKNOWLEDGEMENT IN SCHOLARLY WRITING) AND THAT ALL SUCH USE IS CLEARLY ACKNOWLEDGED.

Contents

<u>LIST OF FIGURES</u>	<u>IV</u>
<u>LIST OF TABLES</u>	<u>VIII</u>
<u>ABSTRACT.....</u>	<u>1</u>
<u>1. INTRODUCTION.....</u>	<u>3</u>
1.1 COMBUSTION-GENERATED PARTICLES.....	3
1.2 CLASSIFICATION	5
1.3 IMPACT ON EARTH’S LIFE	7
1.3.1 CLIMATE IMPACT.....	7
1.3.2 HEALTH IMPACT	8
1.4 APPLICATIONS IN NANOTECHNOLOGY.....	9
<u>2. AIM AND CONTENT OF THE THESIS.....</u>	<u>12</u>
<u>3. CARBON PARTICLES FORMATION IN FLAMES: STATE OF THE ART.....</u>	<u>14</u>
3.1 GAS PHASE REACTION MECHANISMS.....	15
3.2 NUCLEATION	18
3.2.1 CHEMICAL PATH FOR PARTICLE NUCLEATION	19
3.2.2 PHYSICAL PATH FOR PARTICLE NUCLEATION.....	20
3.3 SURFACE GROWTH.....	23
3.4 COAGULATION OF PARTICLE.....	24
3.4.1 COALESCENT COAGULATION	25
3.4.2 AGGREGATING COAGULATION.....	26
3.5 SOOT OXIDATION	26
<u>4. PHYSICAL AND CHEMICAL PROPERTIES OF COMBUSTION-GENERATED PARTICLES.....</u>	<u>29</u>
4.1 SOOT	29

4.2	NANOPARTICLE.....	32
5.	<u>MODELLING ASPECTS</u>	<u>34</u>
5.1	GAS PHASE KINETICS	34
5.2	MODELLING NANOPARTICLES.....	35
5.3	SEMI-EMPIRICAL METHOD	36
5.4	MOLECULAR DYNAMICS.....	38
5.4.1	FORCE FIELD.....	39
5.4.2	LIMITS AND ADVANTAGES OF EMPIRICAL FORCE FIELDS	42
5.4.3	FORCE FIELDS FOR PAHS	42
6.	<u>MD SIMULATIONS OF PAH STACKING: INFLUENCE OF STRUCTURE OF PRECURSOR PAHS</u>	<u>45</u>
6.1	METHODOLOGY	46
6.1.1	PRECURSOR MOLECULES	46
6.1.2	MD SIMULATIONS	47
6.1.3	INTERACTION POTENTIAL FUNCTION	48
6.1.4	SIMULATION OUTPUT AND CLUSTER IDENTIFICATION	49
6.1.5	STRUCTURAL ANALYSIS	50
6.2	RESULTS AND DISCUSSION.....	51
7.	<u>MD SIMULATIONS OF PAH STACKING: INFLUENCE OF THE INTERMOLECULAR POTENTIAL</u>	<u>59</u>
7.1	METHODOLOGY	60
7.1.1	MD SIMULATIONS	60
7.1.2	INTERACTION POTENTIAL FUNCTION	61
7.1.3	SIMULATION OUTPUT AND CLUSTER IDENTIFICATION	65
7.1.4	STRUCTURAL ANALYSIS	65
7.2	RESULTS AND DISCUSSION.....	65
8.	<u>COLLISION EFFICIENCY</u>	<u>75</u>
8.1	METHODOLOGY	75

8.1.1	MD SIMULATIONS	75
8.1.2	EVALUATION OF THE COLLISION EFFICIENCY	76
8.2	RESULTS AND DISCUSSIONS.....	77
8.2.1	INCREASE IN THE NUMBER OF STARTING MOLECULES	80
9.	<u>MECHANICAL PROPERTIES OF CROSS-LINKED PAHS.....</u>	<u>82</u>
9.1	METHODOLOGY	82
9.1.1	CONSTRUCTION OF THE STARTING GEOMETRY	83
9.1.2	UNIAXIAL TENSILE TEST.....	86
9.1.3	COMPARISON WITH EXPERIMENTAL VALUES	87
9.2	RESULTS AND DISCUSSIONS.....	89
10.	<u>SUMMARY AND CONCLUSIONS</u>	<u>94</u>
11.	<u>REFERENCES.....</u>	<u>97</u>

List of Figures

Figure 1.1 Atmospheric aerosol mass and number distribution (Cooke and Wilson, 1996).....	6
Figure 3.1 Schematic of carbon particles formation in flame (Bockhorn, 1994).....	15
Figure 4.1 Soot extracted from an ethylene flame. (a) particle agglomerate. (b) and (c) HR-TEM of the particle marked with an arrow in (a). (Bhowmick and Biswas, 2011).	31
Figure 6.1 Schematic representation of PAHs molecules used as input.	46
Figure 6.2 Starting simulation box: (a) coronene system (1000 molecules) (b) dicoronene system (500 molecules). The box length is 79.4 nm.	48
Figure 6.3 Percentage of clustered molecules vs MD time for pyrene (red line), coronene (blue line), dipyrene (green line) and dicoronene (black line) at 500 K (left), 1000 K (middle) and 1500 K (right). The error bars represent the deviation of the data sets from the mean values (deviation less than 12% in all the cases).	52
Figure 6.4 Number of clustered molecules vs MD time for pyrene (red line), coronene (blue line), dipyrene (green line) and dicoronene (black line) at 500 K (the deviation of the data sets from the mean values is less than 10% in all the cases).	53
Figure 6.5 CSDs for pyrene (top-left), coronene (top-right), dipyrene (bottom-left) and dicoronene (bottom-right) after 1 ns (red circles) and 6 ns (blue circles) of MD time at 500K.	54
Figure 6.6 IDDs after 6 ns of MD time at 500 K. From left to right: pyrene, coronene, dipyrene, dicoronene.	55
Figure 6.7 Cluster sections obtained with RasMol (Sayle and Milner-White, 1995) and HR-TEM image of nascent ethylene soot adapted from Ref. (Alfè et al., 2009).....	56
Figure 6.8 Structural parameter P for pyrene (blue), coronene (red), dipyrene (green) and dicoronene (black) after 6 ns of MD time at 500 K. Continuous line (top) represents parameter P for ordered stacked clusters; dashed line (bottom) represents the maximum value of parameter P for randomly generated clusters.	57

Figure 7.1 Investigated intermolecular potentials (U_{nb}) calculated for a face-to-face coronene dimer configuration. r_{CM} is the distance between centers of mass of the two coronene molecules. Normalized function of the repulsion branches are reported in the inset.	64
Figure 7.2 Percentage of clustered molecules vs MD time using iso-PAHAP potential, LJfit-iso potential, W potential and VdW potential at 500 K. The error bars represent the deviation of the data sets from the mean values (deviation less than 13% in all the cases).	66
Figure 7.3 Percentage of clustered molecules vs MD time using iso-PAHAP potential, LJfit-iso potential, W potential and VdW potential at 500 K. Filled and empty circles refer to the case of neglecting and considering the electrostatic term, respectively. The square and the triangle refer to the result reported by Kraft and co-workers (Totton, Misquitta and Kraft, 2012) and Violi and co-workers (Chung and Violi, 2011) in the same simulation conditions.	67
Figure 7.4 Number (top) and the mean size (bottom) of clusters formed vs MD time using iso-PAHAP potential, LJfit-iso potential, W potential and VdW potential at 500 K (the deviation of the data sets from the mean values is less than 8% in all the cases).	68
Figure 7.5 Number (left side) and the mean size (right side) of clusters formed as a function of percentage of molecules in clusters using iso-PAHAP potential, LJfit-iso potential, W potential and VdW potential at 500K.	69
Figure 7.6 CSDs obtained in systems using iso-PAHAP potential, LJfit-iso potential, W potential and VdW potential, at 1 ns (left side) and 3 ns (right side) of MD time at 500 K. Solid guidelines are also reported in the figure.	69
Figure 7.7 IDDs using iso-PAHAP potential, LJfit-iso potential, W potential and VdW potential at 3ns of MD time and at 500K. Coloured and grey lines refer to the case of neglecting and considering the electrostatic term, respectively.	70
Figure 7.8. Structural parameter P of coronene clusters formed in the system using iso-PAHAP potential, LJfit-iso potential, W potential and VdW potential, at 3ns of MD time at 500K. Solid line represents parameter P for ordered stacked clusters; dashed represents the maximum value of parameter P for randomly generated clusters.	72
Figure 7.9. Images of clusters with different sizes and structural parameters formed using the four investigated potentials at 3 ns of MD time.	73

Figure 8.1 Percentage of clustered molecules and number of clusters formed in pyrene systems vs MD time at 500 K, 750 K, 1000 K and 1500 K. Squares refer to the result reported by Kraft and co-workers (Totton, Misquitta and Kraft, 2012) at the same simulation conditions.	77
Figure 8.2 Percentage of clustered molecules and number of clusters formed in coronene systems vs MD time at 500 K, 750 K, 1000 K and 1500 K. Squares refer to the result reported by Kraft and co-workers (Totton, Misquitta and Kraft, 2012) at the same simulation conditions.	77
Figure 8.3 Sticking efficiency for sectional particle diameters used by D'Anna and Kent to model soot formation (D'Anna and Kent, 2008). Lines refer to smaller particle diameter (nm).	79
Figure 9.1 The simulation box of uncross-linked monomers after the first equilibration step.	84
Figure 9.2 The radical species obtained removing hydrogen atoms from every second carbon atom around the rim of the monomers.....	85
Figure 9.3 Crosslinking strategy to produce aliphatically linked PAHs.	85
Figure 9.4 The steps involved in the crosslinking simulations: 1. the aromatic molecules are packed into the simulation box; 2. hydrogen atoms are removed from every second carbon atom around the rim of the molecule; 3. a reactive forcefield simulation is run and halted at different times to provide varying degrees of crosslinking; 4. hydrogens are then added back to the sites that have not formed crosslinks; 5. the structure is uniaxially strained until failure.....	87
Figure 9.5 Degree of cross-linking (blue lines and left axes) and C/H ratio (red lines and right axes) as function of MD time for pyrene, coronene and ovalene systems.	89
Figure 9.6 A 5 Å slice of the simulation box before (a) and after (b) the cross-linking procedure for coronene system.....	90
Figure 9.7 Stress–strain curves for pyrene (left), coronene (middle) and ovalene (right) systems with varying degrees of cross-linking (CL). Red circles represent the yield point in each system.	90
Figure 9.8 Stress-strain loading and unloading curves to determine yield stress for the pyrene system with CL=3.40.....	91
Figure 9.9 Stress–strain curves, yield stress, hardness and empirical conversion constant K for HOPG (left) and diamond (right) systems.....	92

Figure 9.10 Hardness vs degree of cross-linking (CL) in the pyrene (red), coronene (blue) and ovalene (green) systems using $K=1.4$ (with error bars showing $K=1.2-1.6$). The hardness values determined for diesel soot and ethylene soot are also shown for comparison (Bhowmick, Majumdar and Biswas, 2011).....93

List of Tables

Table 6.1 LJ potential parameters.....	49
Table 7.1 Function forms and parameters of the four attractive-repulsive (U_{abVdW}) terms tested.....	63
Table 7.2. Values expressed in elementary charge (e) units used in charge sets.	63
Table 7.3. Intermolecular potentials, sum of dispersive forces reported in Table 7.1 and the electrostatic term in which one of three charge sets, listed in Table 7.2, is employed. The first column indicates the name that we use in the following to refer to different potentials.....	63
Table 8.1 Mean and maximum sizes, number of effective collision and collision efficiencies of pyrene after 1 ns, at 500 K, 750 K, 1000 K and 1500 K.	78
Table 8.2 Mean and maximum sizes, number of effective collision and collision efficiencies of coronene after 1 ns, at 500 K, 750 K, 1000 K and 1500 K.	79
Table 8.3 Number of clusters formed in the coronene system after 1 ns at 1500 K for all the five trajectories.	80
Table 8.4 Number of clusters and collision efficiencies of coronene after 1 ns at 1500 K for the five trajectories obtained starting from 1000 and 10000 molecules.....	81
Table 9.1 Carbon materials hardness values from nanoindentation experiments.	88
Table 9.2 Yield stress and hardness values for the investigated PAHs structures using an empirical conversion constant $K=1.4$	92

Abstract

Combustion-generated carbonaceous particles are generally considered as unwanted by-products of energy production and significant atmospheric pollutant. Several studies have been conducted, during last decades, on the chemical-physical mechanisms responsible for the formation of carbon compounds in flames, with the aim of improving the combustion efficiency and reducing the emission of pollutants from combustion devices. Moreover, since such species have many features similar to carbon compounds used in new technologies (fullerene, graphite, carbon blacks and so on), a deeply knowledge on the key steps that control the formation and growth of such species can be a starting point to develop new synthesis routes for specific and tailored carbonaceous structures designed for innovative technologies.

Nucleation of combustion-generated particles remains the least understood process in particle formation in combustion and it is a challenge for both experimental and modelling sides. The peculiar combustion environment, which is characterized by high temperatures and a large number of radicals, make the study of this process very complex. Despite of the efforts spent on the topic, a conclusive description of the process is not reached yet.

Molecular Dynamics (MD) approach allows to describe punctually the physical interaction and evolution of the particles and of their principal constituents, i.e., the polycyclic aromatic hydrocarbons (PAHs). Monitoring the internal coordinate of atoms in the system over the time, MD allows to predict qualitatively the behaviour of a system at conditions that cannot be accessed experimentally.

The objective of this study is to explore nucleation process and the properties of particles obtained by using MD.

Firstly, the role of different PAHs in the physical nucleation process is investigated using MD. Two different types of molecules present in a flame environment are studied: pericondensed aromatic hydrocarbons (PCAHs) and aromatic aliphatic-linked hydrocarbons (AALHs). MD allows to treat the nucleation in a physical way. However, the investigation of AALH evolution permits to treat indirectly also the chemical pathway because every ALLH molecule can be viewed as the result of a chemical reaction between PCAH molecules. The effect of different molecular masses and morphologies of precursor molecules as well as temperatures on the nucleation mechanism is analysed. Moreover, for the first time, statistical analysis of the

morphology of the formed clusters are reported, introducing the internal distance distribution and a structural parameter.

Successively, a study of the effect of the intermolecular potential function on MD simulation of PAHs stacking and cluster morphology is made. The accuracy and reliability of a MD simulation mainly depends on the quality of the force field employed to model the intra- and intermolecular interactions. Many intermolecular potential functions and parametrizations for PAH molecules have been proposed in literature. Four intermolecular potentials, which differ for their function forms and parametrizations used in other MD PAH evolution studies, are tested in order to analyse the difference not only in cluster formation but also in the formed cluster morphologies, an aspect never considered in this kind of studies. The use of a systematic approach to analyse the internal structure and shape of the formed clusters allowed to have a better comparison between the potentials and their capability to reproduce realistic configurations.

Collision efficiencies of pyrene and coronene are also determined from MD results, in order to relate the MD findings with soot formation kinetic models.

Finally, mechanical properties of cross-linked PAHs are tested. The mechanical properties of a material are strictly related to its internal structure. Many HR-TEM studies on soot have been carried on during the years, gaining new insights on its properties, but if its constituents are chemical or only physical bonded is still unclear. MD simulations of uniaxial tensile tests on PAHs boxes with different degree of cross-linking are made. Hardness of each sample is calculated and compared with nanoindentation experiments of soot particles. The results clearly show that the soot structure must present cross-links between its constituent PAH molecules to have a comparable value of the hardness found experimentally.

1. Introduction

1.1 Combustion-generated particles

At the present time, the combustion based on species containing carbon is the most important source of energy. Combustion of fossil fuels and biomass generates particles ranging from micrometer-sized aggregates down to fine and ultrafine particles in the nanometer-sized range.

The largest particles mainly derive from the physical transformation of the inorganic fraction of the fuel, or result from the agglomeration of fine and ultrafine particles nucleating from the gas-phase in the high temperature environment. In particular, the term ‘soot’ refers to carbonaceous particles generated from the incomplete combustion of hydrocarbons. These particles can be successfully removed from combustion exhausts in gas-cleaning devices.

The nanometer-sized particles are formed at high-temperature combustion processes from the transition of gas phase compounds present in a flame environment in form of condensed-phase compounds. The nanoparticles are dominant in the emissions in terms of number concentration.

Scientific studies have linked particles, especially nanoparticles, with a series of significant health and environmental problems. In fact, they are able to penetrate deeper than larger particles into the respiratory system (Oberdörster, Oberdörster and Oberdörster, 2005) (Osunsanya, Prescott and Seaton, 2001) (Kennedy, 2007) (Kumfer and Kennedy, 2009) and they could also affect the radiation balance of the atmosphere by serving as condensation nuclei for the formation of clouds and of contrails in the upper atmosphere (Karcher, 1999). Despite of the large reduction of total amount of combustion-generated particles in commercial devices none of the modern combustion systems can be considered particles emission free because of the difficulties of removing the nanoparticles using these devices.

Emission control from technical combustion processes constitutes a major challenge for industrialized countries. In recent years, there has been a great effort to improve air quality with remarkable results. Modern combustion technologies have significantly reduced air pollution (including NO_x, SO_x, and black smoke emissions) by orders of magnitude. The health and environmental problems related to the emission of nanoparticles in atmosphere have shifted the main concern for the emission control toward the reduction of the number of particles rather

than the total amount. Euro 6 legislation imposes a restriction on the number of solid particles a vehicle can emit.

On the other side, carbonaceous nanostructures (in particular graphene, fullerenes and nanotubes) have been recognized as versatile materials. Since these early days, the range of possible application has greatly expanded, including field emission, molecular electronics, solar cells and energy storage, scanning probe microscopy or sensing and biomedical applications. The huge field of possible applications is related to their particular structure, which ensures them extraordinary mechanical and electrical properties.

The potential impact on human health and the possibility of different applications of carbonaceous nanoparticles have focused the interest of many researchers for quite some time, in order to understand the conditions that lead to their formation. Most of the knowledge about carbonaceous particle in flame is due to the decennial studies conducted in order to strongly reduce the emissions, considered noxious for health and climate. The characterization of the entire size-distribution function of combustion-formed particulate matter and a quantitative understanding of the mechanism of formation of these particles may be critical to the development of strategies for reduction of particulate emission from technical combustion devices. However, to produce smart nanoparticles the knowledge of particle formation has to be shifted toward a deeper level. In fact, the attention has to be paid not only to the total amount produced but also to particle features such as mean size, size distribution, chemical composition, morphological aspect, and internal structure.

Nucleation of combustion-generated particles, in other word the transition from the gas-phase to first molecular cluster, has been highlighted as the key step for controlling both particle total amount and size distribution in modern combustion devices. This has moved the focus of the research toward the understanding of the nucleation process. Unfortunately, nucleation process is hard to be isolated in a real flame and thus systematically studied in an experimental way. The study of this process will be the focus of this study.

1.2 Classification

The particles suspended in the air are also designed as particulate matter or atmospheric aerosol. Atmospheric aerosol can be originated by natural sources, like volcanic eruptions, soil erosion by atmospheric agents, sea spray, etc., or by human sources (house heating, internal combustion engines, etc.), like fossil fuels use, various industrial processes (foundries, mines, cement factories, etc.).

Furthermore, the atmospheric aerosol is called primary if it is released directly into the atmosphere from different sources (wind, combustion processes, or human activities), secondary if it is composed of particles formed subsequently in the atmosphere through chemical and physical reactions. Particles of primary or secondary origin, and in particular those of small size, play an important role among the air pollutants because of their negative effects on human health and of the strong environmental impact.

US EPA reports an idealized classification based on particle modes, as first proposed by Whitby in 1978 (Whitby, 1978). Four particle modes are identified (see Fig. 1.1):

- Nucleation Mode: Freshly formed particles with diameters below about 10 nm, observed during active nucleation events. The lower limit is currently at about 3 nm;
- Aitken Mode: Larger particles with diameters between about 10 and 100 nm;
- Accumulation Mode: Particles with diameters from about 0.1 μm to just above the minimum in the mass or volume distributions which usually occurs between 1 and 3 μm ;
- Coarse Mode or Coarse Particles: Particles with diameters mostly greater than the minimum in the particle mass or volume distributions, which generally occurs between 1 and 3 μm .

Another way of classifying particulate matter (PM) based on the average aerodynamic diameter (d_{aer}), namely the diameter of a spherical particle of unit density having the same settling velocity as the particle in question, is the following:

- Coarse particulate: particulate with d_{aer} bigger than 10 μm ;
- PM₁₀: particulate formed by particles with d_{aer} lower than 10 μm ;
- PM_{2.5}: *fine particulate* with d_{aer} lower than 2.5 μm ;
- PM₁: particles with d_{aer} lower than 1 μm ;

- PM_{0.1} : *ultrafine particles* with d_{aer} lower than 0.1 μm ;
- Nanoparticles: particulate formed by particles with d_{aer} of the order of nanometers.

These may be further divided into:

Nano sized particles, whose diameter is lower than 70 nm.

Hyperfine particles, whose diameter is lower than 10 nm.

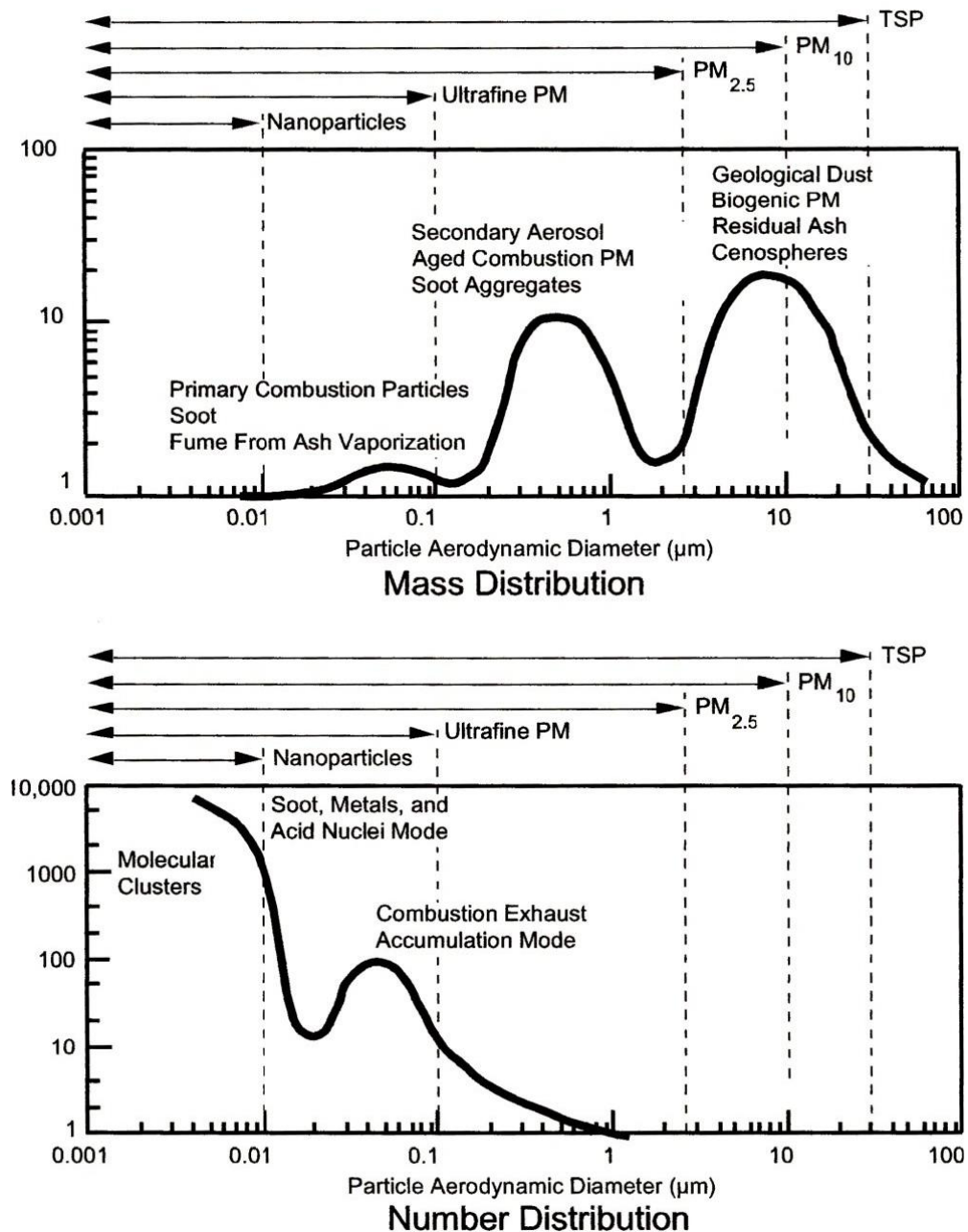


Figure 1.1 Atmospheric aerosol mass and number distribution (Cooke and Wilson, 1996).

1.3 Impact on Earth's life

The demographic growth and the increase of energy consumption have led to an increase in pollution mainly for combustion processes, which are the basis of most of the systems for the generation of energy and transport systems.

Air pollution is the modification of the normal composition of the atmospheric air through fumes, gases, dust and all those substances that cause health and climate issues, also damaging buildings, mainly due to emission of exhaust gases of motor vehicles, boilers, power plants, factories and incinerators. The most common pollutants in the atmosphere are sulphur dioxide (SO_2), nitrogen oxides (NO_x), carbon monoxide (CO), carbon dioxide (CO_2), ammonia, toxic metals, ozone, benzene, polycyclic aromatic hydrocarbons (PAHs), particulate matter (EEA, 2015). Particulate matter pollution is one of the most common problems of the big town and industrial areas. It also reduces visibility, damages buildings and structures, and causes adverse impacts to ecosystems, vegetation, and water quality.

The presence of suspended dust in the atmosphere is related to phenomena such as the mists and clouds formation (Karcher, 1999), variation of the optical properties of the atmosphere with effects on the visibility and the terrestrial energy balance (Horvath, 1993), contamination of water and soil through dry and wet deposition, catalysis of chemical reactions in the atmosphere and material damage.

1.3.1 Climate impact

Aerosols affect Earth's energy balance by scattering and absorbing radiation (the “direct effect”) and by modifying amounts and microphysical and radiative properties of clouds (the “indirect effects”).

Aerosols influence cloud properties through their role as cloud condensation nuclei (CCN) and/or ice nuclei (Karcher, 1999) (Gorbunov et al., 2001). Increases in aerosol particle concentrations may increase the ambient concentration of CCN and ice nuclei, affecting cloud properties. A CCN increase can lead to more cloud droplets so that, for fixed cloud liquid water content, the cloud droplet size will decrease. This effect leads to brighter clouds (the “cloud albedo effect”). Aerosols can also affect clouds by absorbing solar energy and altering the environment in which the cloud develops, thus changing cloud properties without actually

serving as CCN. Such effects can change precipitation patterns as well as cloud extent and optical properties.

The addition of aerosols to the atmosphere alters the intensity of sunlight scattered back to space, absorbed in the atmosphere, and arriving at the surface (Horvath, 1993) (Remer et al., 2009). Such a perturbation of sunlight by aerosols is designated aerosol radiative forcing (RF). Some types of PM, such as aerosols that contain sulphate, scatter sunlight back to space, thus cooling the atmosphere (negative aerosol RF). However, some other types of particles contribute to global warming (positive aerosol RF). Black carbon or “soot”, has been identified as a significant contributor to climate change (Service, 2008). When black carbon accumulates on snow or sea ice, it decreases the ability of the surface to reflect sunlight. By absorbing sunlight, black carbon accelerates the melting of glaciers and polar icecaps (Hansen and Nazarenko, 2004) and may have been responsible for as much as 94% of Arctic warming (McConnell et al., 2007), one of the most dramatic examples of how man-made emissions are changing the global climate.

Climatologists are still working to better understand the effects of various particle types and the net effect of PM on global climate change.

1.3.2 Health impact

Outdoor air pollution is a major environmental health problem affecting everyone in developed and developing countries alike. Numerous scientific studies have linked particle exposure to increased frequency and severity of asthma attacks, trigger heart attacks and cause premature death in people with pre-existing cardiac or respiratory disease. The size of the particles is an important parameter because the smaller particles (PM₁₀ and PM_{2.5}) are able to penetrate the deepest part of the lungs such as the bronchioles or alveoli, enter the bloodstream, and penetrate into cells (Oberdörster, Oberdörster and Oberdörster, 2005) (Osunsanya, Prescott and Seaton, 2001) (Kennedy, 2007) (Kumfer and Kennedy, 2009).

The World Health Organization (WHO, 2014) estimates that in 2012, some 72% of outdoor air pollution-related premature deaths were due to ischaemic heart disease and strokes, while 14% of deaths were due to chronic obstructive pulmonary disease or acute lower respiratory infections, and 14% of deaths were due to lung cancer. Some deaths may be attributed to more than one risk factor at the same time. For example, both smoking and ambient air pollution

affect lung cancer. Some lung cancer deaths could have been averted by improving ambient air quality, or by reducing tobacco smoking.

Outdoor air pollution in both cities and rural areas was estimated to cause 3.7 million premature deaths worldwide per year in 2012; this mortality is due to exposure to small particulate matter of 10 microns or less in diameter (PM₁₀), which cause cardiovascular and respiratory disease, and cancers.

People living in low- and middle-income countries disproportionately experience the burden of outdoor air pollution with 88% (of the 3.7 million premature deaths) occurring in low- and middle-income countries, and the greatest burden in the Western Pacific and South-East Asia regions.

In addition to outdoor air pollution, indoor smoke is a serious health risk for some 3 billion people who cook and heat their homes with biomass fuels and coal. Some 4.3 million premature deaths were attributable to household air pollution in 2012. Almost all of that burden was in low-middle-income countries as well.

The 2005 "WHO Air quality guidelines" offer global guidance on thresholds and limits for key air pollutants that pose health risks. About the particulate matter, the guidelines indicate that by reducing particulate matter smaller than 10 μm (PM₁₀) from 70 to 20 $\mu\text{g}/\text{m}^3$ we can cut air pollution-related deaths by around 15%. Small particulate pollution have health impacts even at very low concentrations – indeed no threshold has been identified below which no damage to health is observed. Therefore, the WHO 2005 guideline limits aimed to achieve the lowest concentrations of PM possible. In addition to guideline values, the Air Quality Guidelines provide interim targets for concentrations of PM₁₀ and PM_{2.5} aimed at promoting a gradual shift from high to lower concentrations.

1.4 Applications in nanotechnology

The use of carbon black goes back to thousands of years ago since men used this material to draw on the cavern walls. Today, the same material finds its use with versatility. Recent applications include the use of soot or carbon nanoparticles as a cathode catalyst (Kay and Gratzel, 1996), in dye-sensitized solar cells (Oregon and Gratzel, 1991) (Gratzel, 2003), and a catalyst support in direct methanol and other fuel cells (Bashyam and Zelenay, 2006).

Other condensed-phase materials form in flames often because of the presence of elements beyond the common constituents of gaseous hydrocarbon flames. As an example, metals or metal precursors can be present or added in unburned fuel–oxidizer mixtures to induce particle formation. Flame aerosol technology for the production of inorganic nanoparticles is used nowadays to realize a large variety of commodities (Stark and Pratsinis, 2002) such as (SRI International, 2001):

- Titania (2 Mt/year) is mainly used for pigments and as ultra-violet light photocatalyst (Madler et al., 2004) (Teleki et al., 2006) (Pratsinis, 1998);
- Zinc oxide (0.6 Mt/year) is an activator of rubber vulcanization and a pharmaceutical additive (Jang, Simer and Ohm, 2006);
- Fumed silica (0.2 Mt/year) is a powder flowing aid in cosmetics and pharmaceutical industries (Ulrich, 1984) (Pratsinis, 1998);
- Fumed alumina is used as solution for chemical mechanical polishing in microelectronics (Pratsinis, 1998).

More recently, flame synthesis have been widely adopted for fullerene production, since it was discovered and isolated in 1985 by Kroto et al (Kroto et al., 1985). The peculiar physical properties of fullerenes allow them to be used for several applications, including superconductors, sensors, catalysts, organic solar cells and medical applications (Thompson and Fréchet, 2008) (Anilkumar et al., 2011). Flame can easily provide both the high temperature and the hydrocarbon reactants for fullerenes synthesis. In order to have high yields low pressure conditions, a rich equivalence ratio close to stoichiometric are used, starting from precursors like highly unsaturated hydrocarbons such as acetylene and benzene (Pope, Marr and Howard, 1993).

The diffusion of carbon nanotubes (CNTs) came just after fullerenes discovery (Iijima, 1991). Flame configurations for CNTs involve the use of a metallic catalyst on which nanotubes grow, starting from many different fuels in both premixed and diffusion flames (Vander Wal, 2000).

Recently, great attention has been given by the scientific community to graphene during the last years, due to its unique two-dimensional structure (Novoselov et al., 2005). Since graphene is younger than the other related materials, growth mechanisms that can lead to the formation of isolated and stable graphene sheets in flame are not yet well understood, but some flames synthesis method for graphene films are already available (Memon et al., 2013).

The range of possible applications of carbon-based nanomaterials has greatly expanded, including various industrial applications, such as high-strength materials and electronics and biomedical applications (Thompson and Fréchet, 2008) (Anilkumar et al., 2011) (Yazyev and Louie, 2010). The huge field of possible applications is related to their unique combinations of chemical and physical properties (*i.e.*, thermal and electrical conductivity, high mechanical strength, and optical properties).

2. Aim and content of the thesis

Nucleation of combustion-generated particles, i. e. the transition from the gas-phase to first molecular cluster, has been highlighted as the key step for controlling both particle total amount and size distribution in modern combustion devices. This has moved the focus of the research toward the understanding of the nucleation process. Unfortunately, nucleation process is hard to be isolated in a real flame and thus systematically studied.

The aim of this PhD project is to investigate the carbonaceous nanoparticles nucleation process using a Molecular Dynamics (MD) approach. A deeper knowledge of nucleation process can be a fundamental step not only to reduce particle emission, but also to produce carbonaceous nanomaterial with tailored properties such as size, chemical composition and internal structure.

Brief descriptions of each chapter are presented below:

In Chapter 3, an overview of the current knowledge of carbonaceous particle formation and evolution in combustion environment is presented. The state of the art of the main processes involved in particle formation is briefly reviewed, focusing mainly on the nucleation process.

In Chapter 4, the properties of soot and nanoparticles are presented. The main differences between these two different classes of particles formed in a flame environment are also described.

In Chapter 5, gas phase kinetic is shortly commented highlighting its role and main challenges. An overview on different approaches for particle formation modelling is also given. After that, the attention is paid on the MD approach, which has been used during this work.

In Chapter 6, the role of different PAHs in the physical nucleation process is investigated using MD. Two different types of molecules present in a flame environment have been studied: pericondensed aromatic hydrocarbons (PCHs) and aromatic aliphatic-linked hydrocarbons (AALHs). Specifically, we will address the effect of different molecular masses and morphologies of precursor molecules as well as temperatures on the soot nucleation process, and on the morphology of the formed clusters.

In Chapter 7, a study of the effect of the intermolecular potential function on MD simulation of PAHs stacking and cluster morphology has been made. The accuracy and reliability of a MD simulation mainly depends on the quality of the force field employed to model the intra- and

intermolecular interactions. Many intermolecular potential functions and parametrizations for PAHs molecules have been proposed in literature and they lead to different results.

In Chapter 8, collision efficiencies of pyrene and coronene has been determined from MD results, in order to relate the MD findings with soot formation kinetic models. The role of small PAHs (pyrene and coronene) in the soot formation process is investigated. The MD results are used to obtain collision efficiency to assess the feasibility of the physical agglomeration of these molecules. In fact, the dimerization of PAHs has been regarded as one of the most important physical agglomeration processes in soot formation. In particular, the dimerization of pyrene is widely used as a nucleation process in many soot-modelling studies. However, recent findings indicate that the dimerization of small PAHs, as pyrene and coronene, may not be a key step in soot formation.

In Chapter 9, mechanical properties of cross-linked PAHs has been tested. The mechanical properties of a material are strictly related to its internal structure. MD simulations of uniaxial tensile tests on PAHs boxes with varying degree of cross-linking have been made. Hardness of every sample has been calculated and compared with hardness obtained with nanoindentation experiments of soot particles.

In Chapter 10, the most important results of this thesis are highlighted and conclusions are given.

3. Carbon particles formation in flames: state of the art

In this chapter, an overview of the current knowledge of carbonaceous particle formation and evolution in combustion environment is presented.

The formation of particles in combustion, particularly soot particles, has been subject of many research papers, comprehensive reviews (Haynes and Wagner, 1981) (Howard, 1991) (D'Anna, 2009a) (Wang, 2011) and published round-table discussions on soot in the last 30 years (Bockhorn, 1994) (Bockhorn et al., 2007). Although much progress has been made during the years, a deep and complete knowledge of all mechanisms involved in particle formation is not achieved yet.

The mechanisms of carbonaceous particle formation in flame are schematically represented in Figure 2.1. Soot formation is a complex process that involves many chemical and physical reactions. It has been viewed as having the following major processes (Bockhorn, 1994) (Frenklach, 2002) (D'Anna, 2009a) (Wang, 2011) that will be described with more details in the next subsections: gas-phase reactions (see 2.1), particle nucleation (see 2.2), particle surface growth (see 2.3), particle coagulation (see 2.4), and particle oxidation (see 2.5).

The process starts with gas phase pyrolysis and oxidation of the hydrocarbon fuel, moving in some conditions toward the formation of large gas-phase polycyclic aromatic hydrocarbon (PAHs). These compounds have been identified as precursor molecules of nanoparticle formation and growth (Richter et al., 2005) (Sirignano, Kent and D'Anna, 2010).

PAHs are subjected to molecular mass growth in the post-flame region, leading these molecules to form larger structures. These structures are later transformed into incipient organic nanoparticles through a molecule-to-cluster nucleation process. The transition from the gas phase PAHs to compounds that present a condensed-phase behaviour (e.g., density, viscosity, plasticity) is called inception mechanism and it remains the less understood topic.

Once the first clusters/particles are nucleated, a series of high-temperature chemical and physical processes lead to particle mass/size growth, and chemical transformation (D'Anna, 2009b).

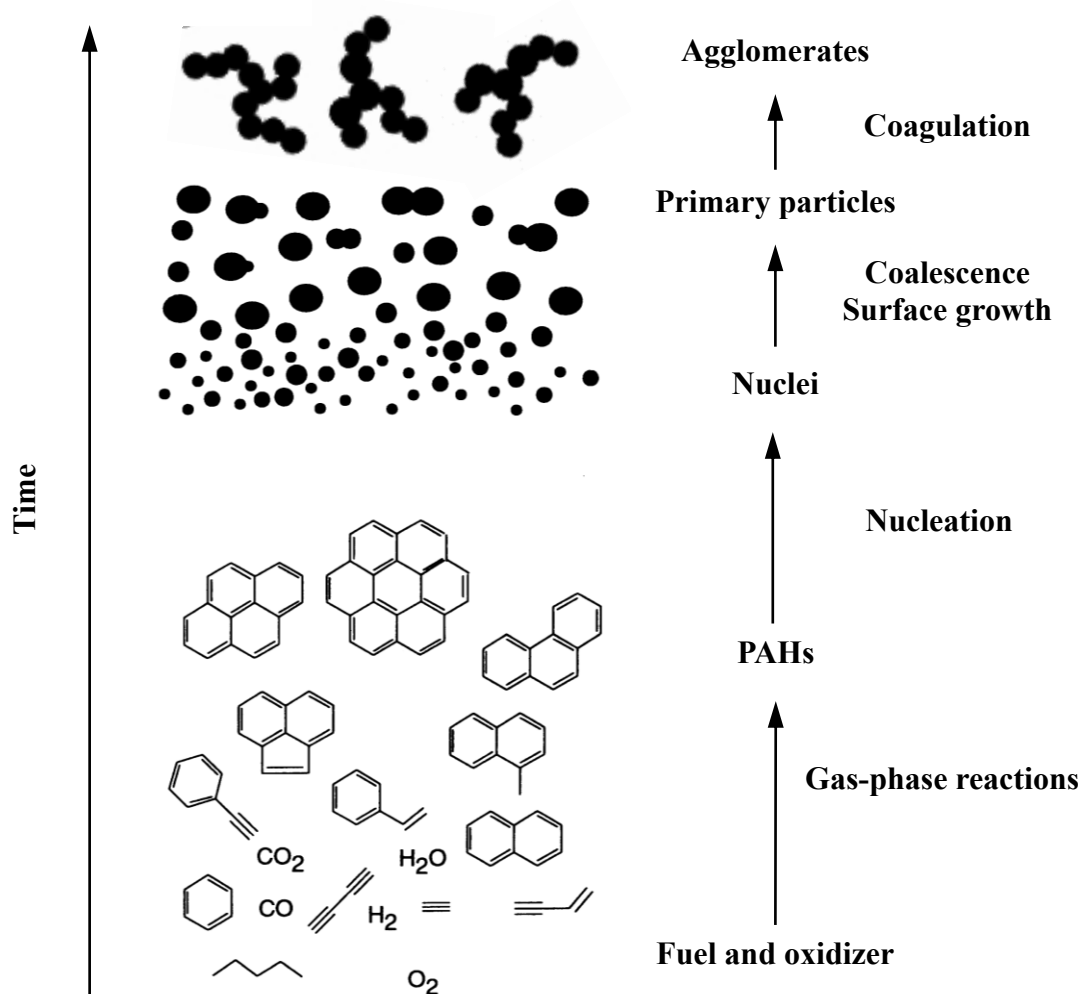


Figure 3.1 Schematic of carbon particles formation in flame (Bockhorn, 1994).

3.1 Gas phase reaction mechanisms

The formation of large molecular weight compounds, in particular PAHs, is strongly related to the formation of incipient particles and soot growth. Nowadays PAHs are universally recognized as the precursor of soot particles (D'Anna, 2009b) (Wang, 2011) and their kinetics have been extensively studied and reviewed in the last decades (Richter and Howard, 2000) (Frenklach, 2002). The main formation pathways of benzene, the first aromatic compound, is of fundamental importance for the understanding of the multi-ring structure formation, that can be seen as an extension of the same mechanism (Frenklach, 2002).

Two main reaction routes have been individuated for the formation of first aromatic ring: the first one involves C_2H_2 , whereas the other involves radical species. In both cases, the formation of benzene comes from a sequential addition of small molecules.

The acetylene pathway for benzene formation goes back to 1980's (Frenklach et al., 1985) (Bittner and Howard, 1981) and it has been studied for more than 10 years in order to catch correct values for thermodynamic properties and rate constants (Frenklach, 2002). After all, this pathway has been found to be determinant at medium-low temperature regime (Frenklach, Yuan and Ramachandra, 1988) (Miller and Melius, 1992), which is not typical of a premixed rich flame of aliphatics.

On the other hand, to fill this gap another route has been proposed by Miller and Melius (Miller and Melius, 1992). The self-recombination of propargyl radicals has been proposed as key step in first aromatic ring formation. Successive studies have recognized this reaction and some similar (Colket and Seery, 1994) (Marinov et al., 1998) to be predominant in high temperature environment.

Multi-ring formation has been almost immediately seen as the limiting step in particulate formation due to its low rate. As for the first aromatic ring, many pathways have been proposed through the years (Frenklach and Wang, 1991) (Melius et al., 1996) (Marinov et al., 1998) (D'Anna, Violi and D'Alessio, 2000) and some of them have been found to be more reliable for the prediction of these high molecular mass compounds. Moreover, a general expression for the molecular growth has been found out with possible application to larger compounds (Frenklach, 2002). Mechanisms can be again divided on the base of the molecules involved.

Acetylene is again one of the fundamental reactants for the formation of PAHs. The idea of using a sequential addition of acetylene goes back to Frenklach and Wang paper, presented at the Twenty-third International Symposium on Combustion (Frenklach and Wang, 1991). They used for the first time the acronym HACA (H-abstraction- C_2H_2 -addition) to provide for word limit of the conference paper, but its appeal made it a worldly known term to define this process. As suggested by the extended name, this reaction pathways starts with an abstraction of a hydrogen atom to form a radical activated species. Successively the addition of an acetylene molecule increases the molecular weight of the species. These two steps have been widely studied. A brief discussion of these mechanisms will be useful for the successive description of the larger aromatic compounds growth.

The formation of radical through the loss of a hydrogen atom can be addressed in different ways: the abstraction can be driven by another radical such as H or OH, largely abundant in flame conditions, or by other gaseous species or via unimolecular reaction. In dependence on the temperature and species concentration, these pathways can have a different relevance. However, the abstraction driven by H and OH atoms has been found to be dominant for a large number of flame conditions (Wang and Frenklach, 1997). Of course, the reversibility of the process is of fundamental importance since it balances the formation of radical species (Mauss, Schafer and Bockhorn, 1994). It has been found that the reverse reaction step is important when the recovery of energy is not addressed. Otherwise the reaction can be considered almost irreversible; this is the case of the formation of a series of PAHs, which minimize the energy, called stabilomer series (Stein and Fahr, 1985).

Another important aspect of the growth through acetylene is the edge migration. This phenomenon has been deeply investigated by Frenklach, Moriarty and co-workers in several papers (Frenklach, Moriarty and Brown, 1998) (Moriarty, Brown and Frenklach, 1999). The final finding has suggested the possibility to have a formation of a closed ring after the formation of a 5-ring structure. The reverse reaction has been taken into account finally sketching a continuous change in the edge of a large aromatic structure. Indeed, the larger is the aromatic multi-ring structure, the higher is the migration rate (Frenklach, 2002).

The other route to form multi-rings species involves resonantly stabilized free radicals (RSFR) (Castaldi et al., 1996) (Marinov et al., 1998). Resonantly stabilization is typical of aromatic species due to their high capability to delocalize the unpaired electron through all the electronic clouds. Radical recombination is favoured by the low activation energy; at same time they can reach considerable high concentration in flame environment. From the radical recombination many different PAHs can be formed. Naphthalene, whose formation has been firstly explained with HACA mechanism, has been found to be formed through the cyclopentadienyl recombination or through benzyl and propargyl radicals (Marinov et al., 1998) (D'Anna, Violi and D'Alessio, 2000). These routes are fast enough to provide large amount of naphthalene in flame environment. Phenanthrene and biphenyl are formed in similar way involving cyclopentadienyl-propargyl and cyclopentadienyl-indenyl recombination respectively (Marinov et al., 1998).

Past and more recent literature is still debating on the relative importance of the HACA and RFSR mechanism for the formation of PAHs in combustion environment (Richter and Howard,

2000) (Frenklach, 2002). Since the combustion conditions can be quite different in terms of gas phase species concentration and temperature history, very often some extreme conditions have been analysed drawing generally valid conclusions. As for other steps in particle formation, it is very likely that these mechanisms take place simultaneously.

3.2 Nucleation

Nucleation, or also called inception, is the fundamental step that, moving from two dimensional structures, leads to the formation of three dimensional ones. This definition tries to be as wide as possible, since any restriction could affect the general validity of some considerations around this process. In fact, the individuation of the first particle, which belongs to the class of particulate matter, can be far enough from the gas phase products and some important species and processes could be missed (D'Anna, 2009a) (Wang, 2011). Moreover, the hardness of defining this “first particle”, in terms of size, morphology, thermodynamic and physical properties, makes the task of finding the missing link between particles and gas phase even harder. Indeed, a clear distinction between these two classes of compounds has been somewhat ruled out by recent findings in this field.

Nearly three decades ago, Stein and Fahr (Stein and Fahr, 1985) analysed the stability of hydrocarbon molecules and concluded that PAH is the most stable bonding configuration at typical flame temperatures. At present, aromatic nature of high molecular mass compounds found in flame has been universally recognized. Small gas phase PAHs have been individuated as main precursors of these compounds (D'Anna, 2009a) (Richter and Howard, 2000) (Bockhorn, 1994) (Bockhorn et al., 2007). However, the growth process of PAHs can lead in principle to very different compounds. The acetylene growth described for gas phase is thought to form always a closed ring, enlarging the wideness of aromatic island and leading towards larger graphene-like sheet with a high degree of aromatization. In fact, after pyrene formation, this growth mechanism would lead to the formation of larger pericondensed aromatic hydrocarbon (PCAH) (Frenklach, 2002). The first aromatic in this series is coronene followed by larger molecules such as circumcoronene. These very large structures would remain in the two dimensional world, until some other process occurs. The detection of similar species in flame has helped in drawing the conclusion that these species could explain the gas-to-particle transition.

The nucleation process will be treated separately for chemical and physical pathways. The first one is quite similar to the steps described above for multi ring formation (see 3.1), whereas the physical one is somewhat different in terms of interaction forces involved.

3.2.1 Chemical path for particle nucleation

In an early modeling work of soot formation by Frenklach et al. (Frenklach et al., 1985), soot nucleation was described as a purely chemical growth of PAHs, and this model significantly under-predicted the corresponding particle size.

In 1988, Homman proposed a bending of the structure on the base of morphological similarity between soot particles and fullerenes to justify the three-dimensional structure formation (Homann, 1998). The presence of five-member ring necessary to bend the structure, present also in fullerenes, was linked to the relevant amount of this kind of compounds in flame. This hypothesis appears now overcome. This kind of so large molecules can be hardly found in flame environment, probably just as trace species and in particular conditions (Wang, 2011). Moreover, recent thermochemical calculation almost ruled it out (Wang, 2011). However, acetylene addition and the PCAHs formation are still reliable up to certain molecular weight. It means that certain species, such as pyrene-to-coronene PAHs can play an important role in inception process (Schuetz and Frenklach, 2002) (Herdman and Miller, 2008).

A possible chemical pathway, that has to be considered within inception process, involves the PAHs radical recombination. Based on the similarity for the formation of the first and the second aromatic ring this process has been described for the first time by D'Anna and co-workers (D'Anna et al., 2001). The main idea is that the formation of aromatic aliphatic linked hydrocarbons (AALHs) overtakes the large pericondensed ones. AALHs can be formed through the combination of an aromatic radical with another radical or its stable form. The formation of an aliphatic bond, or sigma-bond, within the structure introduces a non-rigidity point. The structure can rotate around this bond according with the laws of free energy and quantum mechanics. This biphenyl-like structure can go from very simple interconnection between PAHs, such as the formation of bi-pyrene, up to very complex geometry, which involves tens of PAHs.

These structures can grow by chemical addition of PAHs or acetylene. The final compound would have memory of the different species added since it was formed. In fact, since the first

aliphatic bond is introduced within the structure, the planarity is lost due the free rotation around the axis of this bond. However, topologically speaking, these structures are more like a large irregular surface which is bent into itself, rather than a real three dimensional structure. In fact, in the above description no growth mechanism out of plane occurs. However, the original hypothesis takes these structures as the only responsible for the formation of first compounds, which can be considered a particle.

In several conditions this pathway has been demonstrated to be dominant and several experimental and numerical investigations have found that small particles can effectively look like a hank of relatively small PAHs (D'Anna, 2009a) (D'Anna, 2009b) (D'Anna, Violi and D'Alessio, 2000) (D'Anna et al., 2001). However, these findings are not matching the final form of soot particles, suggesting that some other process induces higher degree of aromatization in the structure during the evolution in flame. This process is mainly linked not only with the final form of the structures but also with their inception mechanism. Hence, aromatization, or graphitization process (Dobbins et al., 1996) can form a stronger linked and more stable structures able to survive for a long enough time in flame conditions (see also section 3.3).

In conclusion, chemical pathways are not completely explaining the inception process. Large efforts in small particle characterization have furnished lot of clues for the understanding the first moments in particles formation. These features have revealed that large macromolecules can be formed and grow. Due to chemical nature of the process, high temperature and concentration of precursors (small gas phase PAHs) can strongly favour this pathway. A significant large presence of acetylene can influence this route moving toward a more aromatized structure.

3.2.2 Physical path for particle nucleation

Physical path involves different forces with respect to chemical reactions and the final product is not a chemically bonded structure. The base of this process is linked with the van der Waal intermolecular forces. These forces are responsible for the attraction of instantaneous and/or permanent dipoles present in the molecules. Moreover, they are not anisotropic and thus depend on molecule orientation beside of the chemical nature of the molecules involved (Schuetz and Frenklach, 2002) (Herdman and Miller, 2008) (Chung and Violi, 2011). In the PAH molecules, the pi-electron cloud extends over the aromatic island formed by the condensed aromatic rings.

This large electronic structure can behave as a part of the dipole attraction involving van der Waal forces. Indeed, the attraction between two PAHs is strongly linked to the interaction of the pi-electron planes and thus to the orientation these planes. Once the two planes are parallel oriented, the attraction between two planes can be enough strong to hold together the molecules. In graphite, the out of plane interaction is due only to these forces and the strength is around 5kJ/mol per carbon atom (Donchev, 2006). The extension of the plane of interaction up to hundreds of atoms might make this interaction as strong as a chemical bond.

Out of plane interactions of gas phase PAHs and their stacking have been supposed to be the key step for the formation of three dimensional structures (Miller, 1991) (Frenklach and Wang, 1994) (Frenklach and Wang, 1991). Through years, the PAHs considered for this process ranged from very large molecule with more than 7 rings to very small PAHs like naphthalene.

Frenklach and co-investigators first proposed that the dimerization, the formation of a compound by the union of two molecules, of PAHs as small as pyrene was necessary to correctly reproduce soot particle size distributions (Frenklach and Wang, 1991) (Frenklach and Wang, 1994). Miller and co-workers (Miller, Smyth and Mallard, 1985) (Miller, 1991) (Herdman and Miller, 2008) also tested the importance of PAH dimerization in soot nucleation process. They initially ruled out the possibility that soot nucleation can begin with PAH dimerization (Miller, Smyth and Mallard, 1985) but later revisited the problem from a kinetic perspective and concluded that the process can occur when the PAH size is four times larger than pyrene (Miller, 1991). In this later analysis, the lifetimes of dimers under flame conditions were calculated by assuming that the energy of the initial collision could be either accommodated by the PAH molecules themselves or removed by molecules in the bath. However, Schuetz and Frenklach (Schuetz and Frenklach, 2002) re-emphasized the role of pyrene by investigating the collision of two pyrene molecules using semi-empirical molecular dynamics method. By comparing the lifetime of pyrene dimer with the collision time with gas molecules in the bath, they concluded that aromatic dimers of species as small as pyrene can survive long enough to evolve into soot nuclei. As a result, pyrene dimerization as a soot nucleation step has been widely accepted and adopted by many current soot-modelling studies (Appel, Bockhorn and Frenklach, 2000) (Kazakov, Wang and Frenklach, 1995) (Mosbach et al., 2009).

However, there is still no definitive experimental data to support the dimerization of pyrene as a key soot nucleation step and great attention has been paid to pyrene stacking, considered the

first of aromatic with a high sticking efficiency. Recent experimental and theoretical studies indicate that pyrene dimerization might not be an important step in soot formation process. For example, Chung and Violi (Chung and Violi, 2011) observed pyrene dimers or trimers using MD simulations and concluded that they are not stable enough to grow into soot nuclei at soot generating temperature conditions. Kraft and co-workers (Totton, Misquitta and Kraft, 2012) studied the physical nucleation of several PAHs using MD simulations and they conclude that in low-temperature regions of the flame (500 K– 1000 K), physical nucleation may still be a competitive route for particle inception and growth for molecules larger than pyrene and only circumcoronene was found to dimerise at 1500 K (Totton, Misquitta and Kraft, 2011). Sabbah et al. (Sabbah et al., 2010) also presented experimental measurements and theoretical study on the kinetics of pyrene dimerization. They demonstrated that the reaction strongly favours the dissociation of the pyrene dimer at high temperature and concluded that the dimerization of pyrene may not be a key nucleation step.

Lot of studies has been conducted to experimentally evaluate the concentration of PAHs in flame and to numerically test the influence of the stacking on the final concentration of small and large particles. For many PAHs, which can be found in flame environment, the calculated strength of interaction is smaller than kinetic energy of the molecules. This mismatching is the weak point of the theory of stacking. However, the calculation of the interaction results not easy. Many side effects have to be considered to correctly represent the real situation. Presence of other molecules, residual charge on the molecules involved (ions), correct method of calculation of potential involved in the process with Density Function Theory (DFT) and ab initio calculation, dispersion of energy due to intramolecular forces and re-arrangement, additional vibrational level due to the presence of side chain in the colliding molecules are the main issue that still remain unsolved in this investigation field. On the other hand, experimental evidences of the presence of interacting planes within the first particles have been recognized and are pushing the scientific community toward filling this gap (Grotheer et al., 2004) (Grotheer, Wolf and Hoffmann, 2011).

Despite of this lack of knowledge, many semi-empirical methods for the evaluation of this process have been carried out and implemented in numerical models. Most of reaction rate expressions come from some evaluation on the sticking efficiency of similar species with some assumption on the potential of interaction. Further discussion on numerical models and way of threat this delicate issue will be given further on (see Chapter 5).

In conclusion, most part of the scientists believes that stacking is fundamental in the inception process but the exact mechanism is still under debate.

3.3 Surface growth

Once formed the first particle or, more correctly, the first species which no longer behaves like a gas phase compound, its evolution is driven by some specific processes. One of these processes is the molecular or surface growth. The term surface growth immediately refers to the fact that the addition of molecules from gas phase to existing condensed compounds can occur preferentially on the surface. Although particles exhibit some nanoporosity, the addition rate is generally fast compared to diffusion inside the particle.

The most important species involved in molecular growth is acetylene (Frenklach and Wang, 1994). Molecular growth is responsible for the soot loading, i.e. the formation of large amount of particulate in terms of volume fraction. In particular, the addition of acetylene follows a reaction pathway similar to the HACA mechanism found and described for the gas phase (Frenklach and Wang, 1991).

Together with acetylene, other gas phase species can contribute to the growth of particles. In particular, aromatic compounds have been individuated as alternative route to acetylene pathway. These compounds can be chemically linked to particles forming aliphatic linked structure similar to those found in the very first particles (D'Anna, Violi and D'Alessio, 2000) (D'Anna et al., 2001). Similarly, aromatic growth can lead to the formation of larger particles independently from acetylene addition. Aromatization process can form larger aromatic islands and, thus, a more packed structure (Dobbins et al., 1996).

Finally, we can conclude that, as for the inception process, in most part of the combustion conditions, particles come from both pathways: surface growth by acetylene and by aromatics contribute together for the final form and amount of particles (D'Anna et al., 2009).

However, in both cases reactions are depending on the active sites on particle surface. In fact, the reactions involve molecular species and particles with active sites.

Radical formation on soot surface is the limiting step for the surface growth. Aromatization process changes the physical properties together with reactivity of particles and, indeed, the number of active sites on the surface. It consists of dehydrogenation reaction and consequently

reduces the number of active sites on the surface. Hence, we can understand that the knowledge of the number of molecular sites on the reacting surface is a fundamental parameter to estimate the growing rate of the particle. From this point of view, molecular growth is depending on aging process occurring on surface (Blanquart and Pitsch, 2009) (Sirignano, Kent and D'Anna, 2010).

These studies are not conclusive for the understanding of the aromatization process since it is not possible to isolate this process. However, actual knowledge suggests that the aromatization can be driven by very high temperature environment and, more important by some radical species, able to extract hydrogen from particles. This extraction makes the particles more aromatic and reduces the number of active sites on the surface.

Recent experimental studies evidenced the aliphatic content in soot particles (Cain et al., 2010) (Cain et al., 2011). The role of aliphatic seems to be predominant on the surface of the final form of soot particles. However, great uncertainty is still present for the results. Since most of studies has been conducted on sampled material, artefacts due to sampling system are still possible and can significantly affect the conclusions.

3.4 Coagulation of Particle

Coagulation processes controls the numerical concentration, the size and final morphology of the soot particles (Smoluchowski, 1916). Soot is emitted generally in form of large aggregates of a hundred nanometers. Despite of these relatively large compounds, particles formed in combustion range from tens of nanometers for primary soot particles down to few nanometers for the very small particles. This process is strongly controlled by the physical characteristics of particles. Properties of particles and their coagulation efficiency have been correlated on the base of experimental evidence and numerical calculations. Indeed, the combustion conditions, which are responsible for the nature of the particles and control the inception process, indirectly affect also the coagulation rate and, thus, the surface growth (D'Alessio et al., 2005).

It is possible to distinguish two different coagulation ways: coalescent coagulation and aggregating coagulation.

3.4.1 Coalescent coagulation

Coalescent coagulation takes place with different final products. Very small particles or condensed species, due to their viscoelasticity during coagulation act like small droplets and tend to form a single larger particle. This process can be associated with coalescence and after that the identity of the colliding particles is lost (Dobbins and Megaridis, 1987). This process is quite similar to what happens during physical inception process. Also in this case van der Waals forces are responsible for the attraction of the species and the formation of intra- and intermolecular bonds. Comparing this process to those studied in metal nanoparticles formation, it is possible to see many similarities. In metal nanoparticles usually sintering process is used to explain the phenomenon that leads to the formation of a new larger particle from the collision of two smaller ones (Camenzind, Caseri and Pratsinis, 2010). Sintering time scale is short compared with contact time when this process is effective. Changing the properties of the particles sintering time scale can change moving toward conditions unfavourable for coalescence.

Looking at the results on the dimension of primary particles and very small nanoparticles, it is almost universally accepted that size dependent coagulation is driving toward a bimodal distribution in particle formation during combustion (Zhao et al., 2003) (Sgro et al., 2007). The small mode is due to particles as small as 2-4 nm whereas large primary particles with sizes of 15-30 nm can be found in the larger mode. Sticking coefficient measured for small nanoparticles is temperature dependent and in flame conditions can be up to three orders of magnitude smaller than at room temperature. This very low sticking efficiency makes these nanoparticles a not negligible intermediate state from gas phase to large particles. They survive along the flame reactor and can be emitted (Minutolo et al., 2008). The exact value of coagulation efficiency depends on the internal structure of these nanoparticles, as stated before. However, for a large number of flame conditions, efficiency relies in a narrow range of values.

Coalescence efficiency increase reaching almost the unity for particles around 7-10 nm, which can be seen as primary soot particles (D'Alessio et al., 2005). Coalescence efficiency of large primary particles decreases rapidly with increasing size. In flame environment, it is not easy to find isolated primary particles with size larger than 40 nm. On the other hand, particles as small as 10 nm can still coalesce forming larger ones. This means that primary particles can rely just in a narrow range of values as found in flame. These particles are hard to be found as isolated ones because, even if the coalescence efficiency is low, the total coagulation efficiency

is high. Indeed, large aggregates are immediately formed and the final form of soot is reached (Mitchell and Frenklach, 1998).

3.4.2 Aggregating coagulation

Aggregates are formed from coagulation of two primary particles, or smaller aggregates, which have no longer the capability to give coalescent coagulation. However, the definition of the starting point of aggregating coagulation, after coalescence stops, is harder. Probably there is not a break point in this process but, more likely, there is a large moiety of intermediate situations. It means that some particles have a partial capability of giving coalescence coagulation or, more correctly, they partially coalesce. The result is a compound in which traces of the identity of colliding particles can be still observed but a new species is formed at same time. Hence, the main constituent of soot is large aggregates usually in fractal form. Into these aggregates there is a large variety of particles in terms of structure and size due to the fact the final form is usually the result of a continuum process occurring along the flame. The mean dimension of aggregates and their molecular weight is thus dependent on the flame history, which these aggregates undergo (Puri et al., 1993) (Balthasar and Frenklach, 2005) (Mitchell and Frenklach, 1998).

3.5 Soot oxidation

Oxidation process of large soot particles and small nanoparticles has been studied in past years. A first great distinction can be done between gas phase oxidation and catalytic oxidation. The latter is widely diffused in after treatment system, e.g. in engine particulate filter stages, due to the possibility to reduce emissions of the largest particle formed in combustion (Messerer, Niessner and Poschl, 2006) (Choi and Foster, 2006) (Seipenbusch et al., 2005). In the last years, combustion technology demonstrated to be able to produce much less amount of soot reducing this problem at source stage. The mean size of particle produced in combustion is decreasing and their number concentration is increasing. Oxidation of these new particles can represent a new border line problem for the after treatments systems (Vander Wal and Tomasek, 2003).

Gas phase non-catalytic oxidation has been on the contrary studied as a limiting stage during soot formation (Neoh, Howard and Sarofim, 1985). The influence on total amount of soot

produced depends on the oxidation resistance of soot itself and on the capability of the combustion environment to give place to oxidation process. The first problem is linked with the characteristic of the particles produced and in particular with the possible points of attack by oxidant species (Vander Wal and Tomasek, 2003).

Molecular oxygen, O_2 , and hydroxyl radical, OH , are the main oxidant species in combustion environment. Molecular oxygen is not easy to be found in rich environment and thus is generally more effective in lean conditions. OH radical instead is always effective due to his presence in almost all combustion conditions, becoming the most important and almost the only one present in rich conditions (Neoh, Howard and Sarofim, 1985).

Oxidation process is always active and thus intimately linked with growth process. This makes the correct evaluation of growth process even harder. An underestimation in oxidation process can easily lead to an overestimation in total soot amount.

In order to better study oxidation process a sort of decoupling has been tried in the past. In particular, Sarofim group used a combustion generated soot aerosol as feed for a secondary combustion process (Neoh, Howard and Sarofim, 1985) (Echavarria et al., 2011). The secondary process was conducted in an environment where particle formation does not occur, i.e. lean, stoichiometric or slightly rich conditions. In these conditions, the oxidation of the fed particles could be systematically studied. However, even this smart attempt suffers of some problems linked to sampling process and evaluation of the particle size. This latter is quite hard to be correctly evaluated with conventional and commercial systems when sizes approach molecular regime.

A global evaluation of reaction rate based on this and other experiments, together with numerical prediction for kinetic expressions, represents the actual knowledge of oxidation process (Kazakov, Wang and Frenklach, 1995) (Harris and Maricq, 2002). However since the first studies on the oxidation process two kind of oxidation steps were individuated: surface oxidation and oxidation-induced fragmentation (Neoh, Howard and Sarofim, 1985) (Echavarria et al., 2011).

Surface oxidation is the process by which oxidizing species from the gas phase (predominantly hydroxyl radicals and molecular oxygen) react with the surface of soot particles, removing carbon mass. This process is always active and is due to all oxidant species.

Oxidation-induced fragmentation is the process by which particles break apart into small pieces, presumably after the structure has been weakened by oxidation. This process regards both aggregates and primary particles and has been found to be active in some conditions and mainly driven by molecular oxygen. Fragmentation has received much less attention in the literature than oxidation. It was first experimentally observed by Neoh et al. (Neoh, Howard and Sarofim, 1985). More recently, a similar configuration has been studied by Echavarria et al (Echavarria et al., 2011).

Surface oxidation limits the total amount of particles and reduces their size. Oxidation-induced fragmentation mainly affects the number concentration of particles and their size. This aspect indirectly affects soot reactivity: an increase in number concentration and surface area enhances all the processes, included surface oxidation. This phenomenon can strongly affect evaluation of global oxidation rate in lab-scale and real combustion systems. Moreover the smaller particles produced by oxidation-induced fragmentation can be emitted. These will have the same dimensions of small nanoparticles produced in combustion after inception process. On the contrary, their characteristics can be similar to those of mature soot particles, from which they come from.

4. Physical and chemical properties of combustion-generated particles

Whenever in a combustion process the amount of oxygen is insufficient to completely burn the hydrocarbons to CO₂ and water (rich combustion), or when the flame temperature is low, carbonaceous particulate matter is produced. As already reported in Chapter 3, the study of particulate matter formation in combustion systems had several progresses during the last decades. Modeling and experimental activities have demonstrated that fuel-rich flame conditions produce particles with a wide size range roughly grouped, on the basis of the bimodal shape of the size distribution function, in two classes of nanoparticles (Bockhorn, 1994) (D'Anna, 2009a) (Wang, 2011). In addition to their sizes, these two classes of particle has different properties, such as chemical structure, morphology, optical and spectroscopy behaviours. The first class of particles, which are usually referred to as organic carbon nanoparticles (NOC), has a mean size approximately in the range 2-4 nm which remains almost constant changing the fuel equivalence ratio and the flame residence time, and possesses intermediate properties between gas-phase compounds and solid particles. The second class of particles has a mean size which shifts from about 4-10 nm to 10-100 nm and more as the flame equivalence ratio and the flame residence time are increased. The larger size particles, those with sizes in the range 10-100 nm, are usually referred to as soot particles.

4.1 Soot

Soot particles are formed in quite fuel-rich flame conditions characterized by a strong yellow-red luminosity (sooting fuel-rich flames, $\Phi > 2.1$).

Soot can be defined as a mix of large single particles and aggregates of particles composed prevalently by large aromatic carbon compounds (Haynes and Wagner, 1981). Other principal constituents are hydrogen and oxygen; occasionally soot may contain sulphur or nitrogen, especially if these were present within the fuel composition.

The particle size is dependent on many factors such as fuel, flame, engine, injector types and operating conditions, where and how the soot particles have been sampled and measured.

Primary, or single particles, can go from 20 nm to 40 nm whereas aggregates can reach sizes from 100 nm to 2 μm as the flame equivalence ratio and the flame residence time are increased. These primary particles are agglomerated in clusters and can contain between 10^5 to 10^6 carbon atoms. The soot measured equivalent mass range from 10^6 to 10^{10} amu. Soot density is estimated to be close to the graphite, around 1.8 g/cm^3 (Haynes and Wagner, 1981).

From electron microscopy studies, soot particles have a chain structure composed up to 4000 of smaller spherical particles (spherules) (Fig 4.1a). The spherules (Fig. 4.1b) are composed of a graphitic outer shell (Fig. 4.1c) exhibiting short range crystalline order in small crystallites, roughly parallel and equidistant. Such structure of a shell which has amorphous material as its core has been designated as ‘turbostratic graphitic’ (Fig. 4.1c). (Palotas et al., 1996) (Chen et al., 2005) (Ishiguro, Takatori and Akihama, 1997).

Structure of soot was originally compared to structure of graphite due to this turbostratic disposition of the aromatic plane within the particles. Hydrogen atoms are generally found to be up to 30% of the carbon ones (H/C molar ratio ranging from 0.05 to 0.33). They can be responsible for the incomplete aromatization of aromatic compounds and the introduction of defects within the structure with respect to graphitic one. Internal arrangement of the structure depends from fuel nature and temperature history. Interdistance between planes in the turbostratic structure and medium size of these planes have been investigated and values have found to rely within a narrow range. Mature soot particles can exhibit a plane interdistance of 0.35 nm, (slightly higher than graphite 0.33 nm), with an average size of length of the aromatic islands around 1 nm. These values can reach 0.5 nm for the interdistance and below 1 nm for the aromatic island.

Recently an analysis of soot surface has evidenced the presence of aliphatic more than in the core of the particles. However, these studies are still ongoing and conclusions are still under debate

Soot particles absorb light in the visible. Soot particles at high temperature environment become incandescent and start emitting. In fact, soot is responsible for the large emission and, due to this important property, soot is desired when high heat transmission radiation coefficient is needed. Hence, laser induced incandescence has been used as system to detect particles in combustion environment (Shaddix, Harrington and Smyth, 1994) (Shaddix and Smyth, 1996).

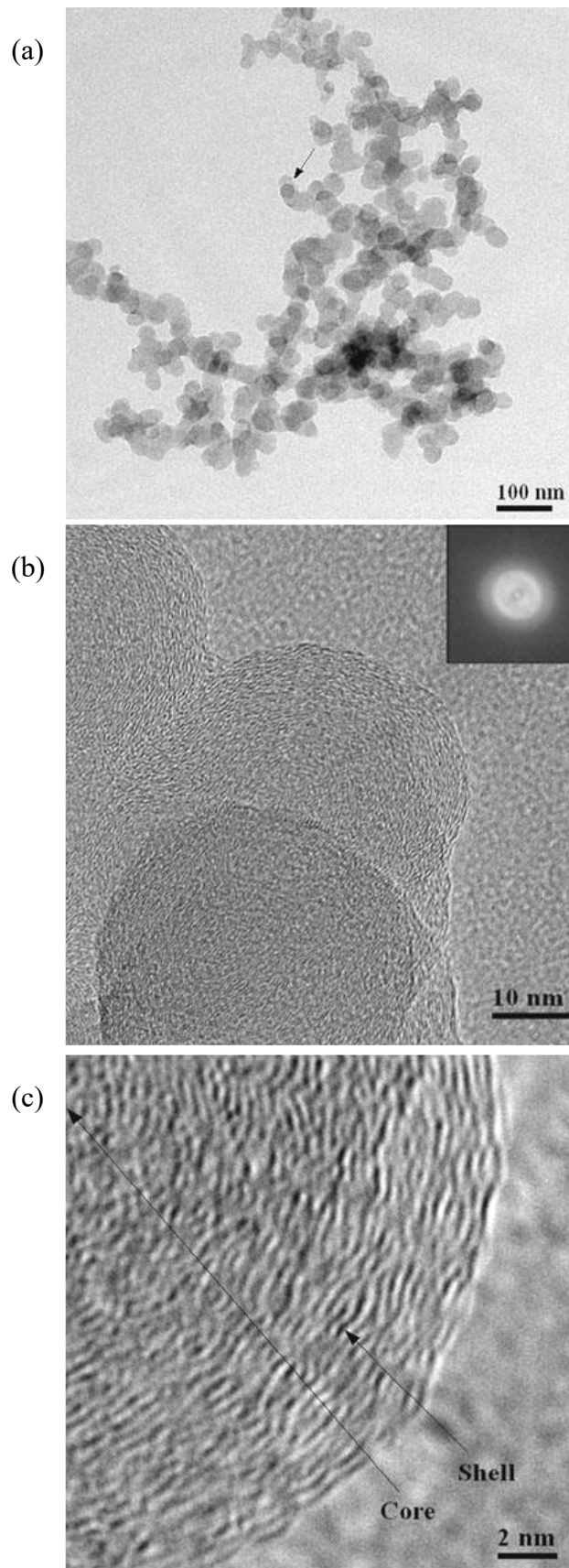


Figure 4.1 Soot extracted from an ethylene flame. (a) particle agglomerate. (b) and (c) HR-TEM of the particle marked with an arrow in (a). (Bhowmick and Biswas, 2011).

However, in the beginning soot was studied taking sample from deposited material or, similarly, directly from the flame, eventually extracting it in solvents (Haynes and Wagner, 1981).

Measurements were conducted by using microscopy techniques or mass spectrometry on sampled material and by measuring absorption and scattering properties by in situ measurement (Richter and Howard, 2000a). These techniques have been used since the first 1960's whereas scanning electron microscopy (SEM), high-resolution transmission electron microscopy (HR-TEM), atomic force microscopy (AFM), differential mobility analysis (DMA), size exclusion chromatography (SEC) have recently given more information on mean size, size distribution, morphology and internal structure of soot particles. Moreover, gravimetric and elemental analysis give quantitative information about total production and composition of soot in flame (Bockhorn et al., 2007) (D'Anna, 2009a).

Due to chemical composition and morphological arrangement, soot is not soluble in water and in main organic solvents. One of the possible definitions of soot is based on this property. However some stable suspensions used to analyse soot with ex-situ techniques have been made using N-methylpyrrolidone.

4.2 Nanoparticle

Carbonaceous nanoparticles, or also called nanoparticles of organic carbon (NOC), can be defined as a class of compounds within carbonaceous material produced in combustion. Particles belonging to this class show intermediate properties between gas phase molecules and solid particles. They maintain molecular characteristics in terms of chemical reactivity, but at the same time exhibit transport and surface related phenomena typical of particles. Their existence was initially detected through optical diagnostic. Many new diagnostic tools (such as laser induced emission, atomic force microscopy and differential mobility analysis), which allow analysis on an almost atomic level have been developed, or borrowed from molecule-based natural sciences. Their use improves our knowledge about the physical and chemical properties of combustion-formed nanoparticles and also about the kinetics of particle formation in combustion environments.

NOC have a mean size approximately in the range 1-4 nm, which remains almost constant changing the fuel equivalence ratio (the ratio of the fuel-to-oxidizer ratio to the stoichiometric

fuel-to-oxidizer ratio, ϕ) and the flame residence time. NOC are generated both in sooting conditions, where they coexist with larger primary soot particles and soot aggregates, and in less fuel-rich bluish flame conditions (non sooting fuel-rich flames, $1.7 < \phi < 2.1$), where they are formed alone or coexist with the larger 4-10 nm particles (Dobbins, 2007) (Maricq, 2004) (Commodo et al., 2015). Isolated nanoparticles with larger diameters are quite hard to be found, due to their rapid coagulation toward soot particles.

Nanoparticles have molecular-like spectroscopic behaviour, absorbing in the Ultra Violet region, giving fluorescence and small scattering signals when excited with a laser source (Commodo et al., 2007). Wavelength peaks in fluorescence signal can be correlated to the extension of the aromatic islands within the particles. A signal typical also of gas phase PAHs, which are the constituent of nanoparticles has been detected. Moreover, nanoparticles exhibit an H/C molar ratio ranging from 0.5 to 1, typical of small gas phase PAHs. Due to their chemical composition and morphological arrangement, these particles are partially soluble in water and soluble in some organic solvents, such as dichloromethane.

Despite of these similarities with gas phase compounds some differences have been individuated. Analysis of quantum yield has evidenced the condensed phase nature of nanoparticles. Nanoparticles do not exhibit a solid-state character typical of soot particles. However, recent studies have confirmed that particles as small as 1.5 nm has a condensed phase feature with some viscoelastic properties. This behaviour has induced the scientific community to define these particles as liquid-like compounds. Because of this behaviour, they also assume an atomically thin disk-like shape when deposited on a substrate (Dobbins, 2007) (Minutolo et al., 2014). Their mass density is approximately 1.5 g/cm^3 (Zhao, Uchikawa and Wang, 2007), which is notably smaller than that of mature soot.

In dependence on combustion conditions and temperature history, nanoparticles can reach relatively extreme features as some high level of organization or low H/C molar ratio making them more similar to very small soot particles rather than completely different compounds. (Bockhorn et al., 2007).

5. Modelling aspects

In this chapter, details of modelling attempts of particle formation prediction will be presented. Particle formation remains one of the most challenging subjects in combustion science. The peculiar combustion environment, which is characterized by high temperatures and large pools of radicals, make the study of this process very complex. The complexity of its study is mainly related to the wide range of length scales and time scales involved. The huge number of species that take part in the process have sizes starting from small molecules, to large soot particles of sizes in the order of few micrometers; the relevant time scale also ranges from a few nanoseconds in case of intramolecular interactions to a few seconds for convective transport of soot particles. Moreover, unlike other gaseous combustion-generated pollutants (CO, CO₂, and NO_x) that have a well-defined chemical composition, each soot particle has its unique chemical composition, size, and morphology (see Chapter 4) (Palotas et al., 1996) (Vander Wal et al., 2007).

A detailed kinetic model of soot formation can be viewed as comprised of two principal components: gas-phase chemistry and soot particle dynamics.

Starting with a short comment on gas phase kinetic, its role and main challenges, a brief overview on different approaches for particle modelling will be furnished. After that, the attention will be paid to the molecular dynamics (MD) method, which has been used during this work.

5.1 Gas phase kinetics

Gas phase kinetic is of fundamental relevance for getting correct prediction of particle formation and growth in flame (D'Anna, 2009a). Incorrect gas phase kinetics could lead to wrong conclusion, underestimating or overestimating some reaction pathways.

Gas-phase chemistry models use a large set of gas-phase species and reactions. Many efforts have been spent in this field in order to have a precise tool to apply in several conditions. Although the behaviour of some reactions is still under debate in the limit of high and low pressure (Li, Kazakov and Dryer, 2004), the atmospheric conditions are quite well managed by

scientific community. In literature, large number of comprehensive kinetic scheme are presented (Sheen et al., 2009) (Frenklach et al., 2011) (CRECK Modeling Group Polimi, 2017). Hydrocarbon oxidation and pyrolysis is mainly modelled with a detailed kinetic mechanism built onto the Gas Research Institute (GRI) mechanism for C1 and C2 species (Frenklach et al., 2011). In aliphatic fuel flames acetylene and methane are the most abundant, gaseous, unburned hydrocarbons and benzene is the first product of the molecular growth process (Ciajolo et al., 1994). Benzene formation is considered to occur by the addition of n-C4 radicals to C₂H₂ (Frenklach et al., 1985) and the self-combination of propargyl radicals (Miller and Melius, 1992). The sequential addition of C₂H₂ to phenyl radical (HACA mechanism) (Frenklach and Wang, 1991) and the combination of resonantly stabilized radicals, RSFR (Castaldi et al., 1996) (Colket and Seery, 1994), are the pathways considered for the growth of aromatic cycles up to pyrene. All these mechanisms rely in a short error bar, at least for the major species involved in combustion process. Ethylene, methane, acetylene, benzene and their related radical and stable species are quite well determined in terms of formation and evolution during combustion conditions. However, small differences in gas phase kinetic are still present.

5.2 Modelling Nanoparticles

During the years, semi-empirical models have been mainly used to predict the soot formation. In these models, the evolution of the particle ensemble is treated using the Smoluchowski coagulation equation (Smoluchowski, 1916). Particle dynamics has been modelled in these semi-empirical methods by using the discrete-sectional method (Kazakov, Wang and Frenklach, 1995) (Pope and Howard, 1997) or the method of moments (Frenklach and Harris, 1987) (Appel, Bockhorn and Frenklach, 2000). In the discrete-sectional method, the particle ensemble is divided into sections and the particle properties are averaged within each section. In the method of moments, the particle dynamics is rewritten in terms of moments of the particle size distribution function. While we need the infinite set of these moments to solve the problem, the determination of just the first few derivatives is sufficient for most practical applications, such as obtaining soot volume fraction, specific surface area, light absorption, and light scattering. These methods are the mainly used to have particle formation prediction.

Although these models are the most efficient for prediction of number of particles effectively formed in a combustion environment, they are unable to describe at a deep level the real interaction

that link the gas-phase chemistry and soot particle dynamics, in other word the nucleation process. Moreover, the experimental findings are limited and the process still remains the least understood step within the soot formation process.

As a result, it is necessary to use more advanced molecular modeling approaches to have a deeper knowledge of the process. Among the modelling methods, MD allow to predict qualitatively the behaviour of a system at conditions that cannot be accessed experimentally. In fact, MD simulations represent a simple and efficient method to explore the evolution of complex systems composed by many interacting atoms.

Ab initio calculation (Kubicki, 2006) and MD simulations with on-the-fly quantum forces (Schuetz and Frenklach, 2002) (Wong et al., 2009) have been used to simulate PAH dimerization and to understand if this step can be a key one in particle formation. However, these methods have to face against the computing capacity. Classical MD have been done to study the evolution of PAHs in controlled temperature environment. Violi and co-workers modelled the clustering behaviours of small aromatics, aromatics with an aliphatic chain and fullerenes at different temperatures providing information on the clustering behaviour of the different aromatic structures (Chung and Violi, 2010) (Chung and Violi, 2011). Kraft and co-workers has performed simulations on clustering of different PAHs (Totton, Misquitta and Kraft, 2010). Iavarone et al. have simulated the nucleation behaviour of six organic molecules in a range of sizes (pyrene and coronene) and molecular structures (single molecules, covalent-bonded dimers and covalent-bonded trimers) (Iavarone et al., 2017).

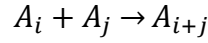
Molecular dynamics is the method used in this thesis to treat particle formation and properties. A detailed description of MD method is presented further on (see 5.4).

5.3 Semi-empirical method

Semi-empirical methods used a detailed kinetic mechanism that includes a reaction pathway for the aromatic growth and a reaction pathway leading to the formation of nanosized particles and their coagulation and growth to larger soot particles. One of the key model quantities, which determines the soot inception and growth rates, is the probability that PAH molecules, or clusters, will stick upon collision. This quantity is termed the collision efficiency and is defined as the ratio of successful collisions (i.e. collisions which form clusters) to the total number of collisions.

According to the collision theory, the rate at which a reaction proceeds is equal to the frequency of effective collisions. We can define the nucleation rate through dimerization in terms of the collision frequency and the collision efficiency of two molecules.

Considering the reaction:



The nucleation rate can be expressed as:

$$r_{\text{nuc}} = \sum_{i=1}^N \sum_{j=1}^N K_{ij} \gamma N_i N_j \quad (5.1)$$

where r_{nuc} is the nucleation rate, K_{ij} is the collision frequency, γ is the collision efficiency, N_i and N_j are the number density of i and j species, N is the number of species in the system. Assuming a free-molecular regime, K_{ij} is:

$$K_{ij} = \sigma_{ij} \sqrt{\frac{8k_B T}{\pi \mu_{ij}}} \quad (5.2)$$

where, σ_{ij} is the reaction cross section between species i and j , k_B is the Boltzmann constant, T is the system temperature and μ_{ij} is the reduced mass of species i and j . It should also be mentioned that γ is not a constant, but highly dependent on temperature and dimension of colliding species. In fact, the energy level of two colliding molecules is one of the important factors that determines γ . (D'Alessio et al., 2005) (D'Anna and Kent, 2008).

If the colliding species are the same, the nucleation rate can be expressed as:

$$r_{\text{nuc}} = \frac{dN_{\text{dimer}}}{dt} = \gamma \pi d_{\text{PAH}}^2 \sqrt{\frac{4\pi k_B T}{m_{\text{PAH}}}} N_{\text{PAH}}^2 \quad (5.3)$$

where d_{PAH} is the diameter of the PAH molecule, m_{PAH} is the mass of the PAH molecule, and N_{PAH} is the PAH number concentration. While all these parameters can be obtained from the reactants and flame conditions, determining the collision efficiency is not straight forward.

D'Alessio et al. proposed an empirical function to determine the collision efficiency (D'Alessio et al., 2005):

$$\gamma(D, T) = 1 - \left(1 + \frac{\Phi(D, Ha)}{k_B T}\right) \exp\left(-\frac{\Phi(D, Ha)}{k_B T}\right) \quad (5.4)$$

where Φ , the minima of the interaction potential of the system, can be considered as a function of the equivalent diameter D of the nanoparticles and of their Hamaker constant. Comparing with the sticking efficiency obtained experimentally using AFM and optical diagnostic for nanoparticles formed in premixed ethylene–air flames, the interpolation is quite good when an Hamaker constant of $3 \cdot 10^{20}$ J is used. This value of the Hamaker constant is intermediate between those for aliphatic and benzenic rings. D’Anna and Kent used this simple model proposed for premixed flame coagulation, to model also nonpremixed flames (D’Anna and Kent, 2008). The particle size distribution of premixed and non-premixed flame is reproduced quite well using this model.

Recently, Raj et al. (Raj et al., 2010) also studied PAH collision efficiency and presented it as an empirical function of molecular mass and diameter. While temperature is a major factor that influences collision efficiency, the empirical relation presented by the authors does not include the effect of temperature.

5.4 Molecular dynamics

Molecular dynamics (MD) is a computer simulation method for studying the physical movements of atoms and molecules in a N-body system. The method was originally developed within the field of theoretical physics in the late 1950s (Metropolis et al., 1953) (Alder and Wainwright, 1957), but is applied today mostly in chemical physics, materials science and the modelling of biomolecules.

The atoms and molecules are allowed to interact for a fixed period of time, giving a view of the dynamic evolution of the system. A MD simulation produce a dynamical trajectory for a system composed of N interacting atoms by integrating Newton’s equations of motion, where forces between the atoms and their potential energies are calculated using interatomic potentials:

$$\mathbf{f}_i = m_i \frac{d^2 \mathbf{r}_i}{dt^2} = -\frac{\partial}{\partial \mathbf{r}_i} U(\mathbf{r}_1, \mathbf{r}_2, \dots, \mathbf{r}_N) \quad (5.5)$$

$U(\mathbf{r}_1, \mathbf{r}_2, \dots, \mathbf{r}_N)$ is the potential energy depending on the coordinates of the N particles. This is a system of N coupled second order non-linear differential equations that cannot be solved exactly, so Eq. (5.5) has to be solved numerically step by step using an appropriate integration algorithm.

The choice of a good model to represent the interatomic forces acting between the atoms composing the system is the most important thing to consider in an MD simulation. There are different methods to obtain a good representation of forces acting among the atoms in the system.

Ideally, this can be done from first principles, solving the electronic structure for a particular configuration of the nuclei, and then calculating the resulting forces on each atom (Martin, 2004). Since the pioneering work of Car and Parrinello (Car and Parrinello, 1985), the development of *ab initio* MD (AIMD) simulations has grown steadily and today the use of the density functional theory (DFT) (Deutsch and Genovese, 2011) allows to treat systems of a reasonable size (several hundreds of atoms) and to achieve time scales of the order of hundreds of ps, so this is the preferred solution to deal with many problems of interest. However quite often the spatial and/or time-scales needed are prohibitively expensive for such *ab initio* methods. In such cases, it is necessary to use a higher level of approximation and make recourse to empirical force field (FF) based methods. They allow to simulate systems containing hundreds of thousands of atoms during times of several nanoseconds or even microseconds. On the other hand, the quality of a force field needs to be assessed experimentally.

The choice of the method mainly depends on the area of intended application and on the information that would be obtained from MD. High accuracy is typically required in Computational Chemistry, computational speed is often critical in Materials Science where processes have a collective character and big systems should be simulated for long times. (González, 2011).

5.4.1 Force field

A force field is a mathematical expression describing the dependence of the interatomic potential energy U of a system of N atoms on the coordinates of the atoms $\mathbf{r}_1, \mathbf{r}_2, \dots, \mathbf{r}_N$. It consists of an analytical form of the interatomic potential energy, $U(\mathbf{r}_1, \mathbf{r}_2, \dots, \mathbf{r}_N)$, and a set of parameters entering into this form. The parameters are typically obtained either from *ab initio*

or semi-empirical quantum mechanical calculations or by fitting to experimental data such as neutron, X-ray and electron diffraction, NMR, infrared, Raman and neutron spectroscopy, etc. The FF replaces the true potential with a simplified model valid for the simulated system. Ideally, it must be simple enough to be evaluated quickly, but sufficiently detailed to reproduce the properties of interest of the system studied. There are many force fields available in the literature, having different degrees of complexity, and oriented to treat different kinds of systems (González, 2011). However the general expression for a FF is:

$$U = U_{\text{bonded}} + U_{\text{non-bonded}} \quad (5.6)$$

where the first terms refer to intramolecular or local contributions to the total energy and the second term serve to describe the intermolecular interactions.

The intramolecular potential term considers interactions within a molecule. It comprises bond stretching, angle bending, torsional-angle rotation, and improper dihedral angle distortion. Generally, the bonded term is expressed as in Eq. (5.7):

$$U_{\text{bonded}} = \sum_{\text{bonds}} \frac{1}{2} K_b (b - b_0)^2 + \sum_{\text{angles}} \frac{1}{2} K_\theta (\theta - \theta_0)^2 + \\ + \sum_{\text{torsions}} \frac{1}{2} \sum_{i=1}^4 C_i (1 + (-1)^{n+1} \cos(n\phi)) + \sum_{\text{improper}} \frac{1}{2} K_\xi (\xi - \xi_0)^2 \quad (5.7)$$

The letters b , θ , ϕ , and ξ are the bond lengths, bond angles, torsional dihedral angles, and improper dihedral angles. The variables with a 0 as subscript are the reference or ideal values and are parameters of the force field. Generally, all interactions have a harmonic functional form as in Eq. (5.7), except for the torsional dihedral-angle term. The labels K indicate force constants. The harmonic function implies that the bond cannot be broken, so no chemical processes can be studied. This is one of the main limitations of FF based MD simulations compared to *ab initio* MD. Occasionally some other functional forms (in particular, the Morse potential or trigonometric potential) are employed to improve the accuracy. However as those forms are more expensive in terms of computing time and under most circumstances the harmonic approximation is reasonably good, most of the existing potentials use the simpler harmonic function. As regard the torsional dihedral-angle term, many representations can be found in the literature. In Eq. (5.7) the OPLS potential the following expression has been used.

The intermolecular potential act between any pair of atoms belonging to different molecules, but they also intervene between atoms belonging to the same molecule that are sufficiently separated (usually more than three bonds).

$$U_{\text{non-bonded}} = \sum_A \sum_B \sum_{a \in A} \sum_{b \in B} U_{ab}(r_{ab}) \quad (5.8)$$

Molecules are indicated by symbols A and B and atoms of these molecules are indicated by symbols a and b , respectively. The pairwise atomic interaction, U_{ab} , is function of the atom-atom separation r_{ab} . It describe the Van der Waals interactions and Coulomb interaction:

$$U_{ab}(r_{ab}) = U_{ab}^{\text{VdW}}(r_{ab}) + U_{ab}^{\text{Coulomb}}(r_{ab}) \quad (5.9)$$

Van der Waals interactions between two atoms arise from the balance between repulsive and attractive forces. Repulsion is due to the overlap of the electron clouds of both atoms, while the interactions between induced dipoles result in an attractive component that varies as r^{-6} . The 12-6 Lennard-Jones (LJ) potential is very often used to represent these interactions, but it is not uncommon to find some “softer” terms to describe the repulsive part, in particular the exponential function, which is used in the Buckingham potential and is preferred over the LJ function in some studies. Other functions are also used occasionally.

The Coulomb term serves to describe the electrostatic interactions. While the molecular electronic density can be obtained with a high accuracy by means of high-level quantum-mechanical calculations, the problem of reducing such density to a manageable description to be used in a MD simulation is not trivial. The usual choice is to assign a partial atomic charge to each nucleus and use Coulomb’s law to compute their contribution to the total energy:

$$U_{ab}^{\text{Coulomb}}(r_{ab}) = \frac{q_a q_b}{r_{ab}} \quad (5.10)$$

where q_a and q_b are the partial charges of atom a and b and they are force-field parameters. The partial charges can be derived from a fit to experimental thermodynamic data, but this approach is only practical for small molecules. The most common way to obtain reliable partial charges consists of performing an *ab initio* calculation and then deriving them from the quantum mechanical potential calculation (González, 2011).

5.4.2 Limits and advantages of empirical force fields

Compared to AIMD, the use of empirical force field based simulations has some intrinsic limitations. In particular, they cannot provide any information about the electronic structure and they are unable to handle reactions such as the breaking and formation of bonds, electron excitations, charge transfers, etc. their accuracy depends on the quality of its parametrization. Their transferability is also limited, so great care is needed when applying a potential to simulate a system under conditions that differ strongly from the conditions used in the parametrization (e.g. different solvent, pressure, temperature, etc.). Finally, we must not forget that any FF is based on numerous approximations and derived from different types of data. This is the reason why they are called empirical and thus any simulation should be validated by an appropriate comparison with experimental results (González, 2011).

On the other hand, force field based simulations are several orders of magnitude faster than AIMD simulations, due to the simplicity of the force calculation using an expression like equation reported above compared to the huge problem of solving the electronic structure to obtain the interatomic forces. Consequently, it is possible to simulate much larger systems containing millions of atoms and explore much longer simulation times until the order of microseconds (González, 2011).

Many specialized groups are working actively in developing new methods to overcome some of the limitations of empirical force fields. For example, reactive force fields allows chemical reactivity to be treated (van Duin et al., 2001) (Stuart, Tutein and Harrison, 2000) or another popular approach consists of combining quantum mechanical and molecular mechanical potentials (QM/MM) (Lin and Truhlar, 2007).

5.4.3 Force fields for PAHs

As already reported in the previous sections, the accuracy and reliability of a MD simulation mainly depends on the quality of the force field employed to model the intra- and intermolecular interactions.

In seeking to model the physical nucleation of PAH molecules it is important to ensure the intermolecular interactions are modelled accurately. This issue has been covered in literature by different research groups. Advances in processing power have enabled intermolecular

interactions to be studied in PAH molecules up to the size of coronene (Janowski and Pulay, 2007) (Janowski, Ford and Pulay, 2010) (Podeszwa, Bukowski and Szalewicz, 2006) with accurate quantum chemistry methods. Whilst in many cases these studies represent benchmarks in intermolecular interaction energies, they remain impractical for the study of systems of many large molecules. Semi-empirical potential, such as the PM3 potential (Stewart, 1989a) (Stewart, 1989b), used by Frenklach and co-worker to model PAH dimerization (Schuetz and Frenklach, 2002) (Wong et al., 2009), has been also presented in literature. They are based on a quantum mechanical model and their use is limited to small size systems and short timescales, of the order of picoseconds, due to computational costs.

The formation of clusters and their morphologies, i.e., bigger size systems evolving on longer timescales, can be studied with reasonable computational costs only by using empirical atom-atom potentials. Different empirical potentials for PAHs are reported in the literature. A Buckingham potential (exp-6 potential) parametrization has been proposed by Williams (Williams and Starr, 1977) and has been used for the calculation of the intermolecular interactions of homo-molecular and hetero-molecular clusters of PAHs by Miller and co-workers (Miller, Mallard and Smyth, 1984) (Herdman and Miller, 2008). A Lennard-Jones (LJ) type parametrization has been proposed by Van de Waal (Van de Waal, 1983). It was calculated by fitting the position and depth of the minima of the Buckingham potential sets of Williams (Williams and Starr, 1977). Violi and co-workers have used this LJ-type potential to model the clustering behaviors of small PAHs and fullerenes at different temperatures (Chung and Violi, 2010) (Chung and Violi, 2011). Rapacioli et al. also used this potential to study the most stable configurations of clusters of PAHs using a global optimization approach (Rapacioli et al., 2005). Both empirical potentials proposed by Williams (Williams and Starr, 1977) and Van de Waal (Van de Waal, 1983) are parametrized to match the heat of sublimation of aromatic hydrocarbons and crystallographic data.

An anisotropic potential developed by Kraft and co-workers has been parametrized using ab initio results, to model interactions between PAHs (PAHAP potential) (Totton, Misquitta and Kraft, 2010). In the PAHAP potential the short-range exchange-repulsion was modelled using an anisotropic Born-Mayer term and the long-range dispersion was modelled with a damped isotropic C6 term. Comparing with the reference energies taken from ab initio symmetry-adapted perturbation theory -SAPT(DFT)- calculations performed by Podeszwa and Szalewicz (Podeszwa and Szalewicz, 2008), the PAHAP potential accurately models interaction energy

for a variety of dimer configurations for different PAH molecules. An isotropic form of the PAHAP potential (iso-PAHAP potential) was developed successively by the same group, in order to use it in MD softwares. It differs from the PAHAP potential because it is no longer orientation-dependent. This potential has been used to perform MD simulations on clustering of PAHs with sizes ranging from pyrene ($C_{16}H_{10}$) to circumcoronene ($C_{54}H_{18}$) in a wide range of temperatures (500 K-1500 K) (Totton, Misquitta and Kraft, 2012). Recently, Iavarone et al. have used the iso-PAHAP potential (Iavarone et al., 2017) to simulate the organic molecules in the same range of temperatures.

As reported in the previous section, these potential can be used only to model the physical nucleation of PAH molecules, because they are unable to handle reactions such as the breaking and formation of bonds. These limitations has been overcome with the reactive force fields. Some reactive force fields to model hydrocarbon and amorphous carbon has been developed in the last years, as Tersoff (Tersoff, 1988), REBO (Brenner et al., 2002), ReaxFF (van Duin et al., 2001), AIREBO (Stuart, Tutein and Harrison, 2000). Tersoff and REBO potentials does not include van der Waals interactions, while ReaxFF and AIREBO potential contain van der Waals interactions. ReaxFF is the only one among the potential mentioned above that include the Coulomb interactions and it is the most computationally expensive.

6. MD simulations of PAH stacking: influence of structure of precursor PAHs

The presence of stacked PAH molecules was revealed by HR-TEM (Palotas et al., 1996) (Ishiguro, Takatori and Akihama, 1997) (Vander Wal et al., 2007) (Alfè et al., 2009) and AFM (De Falco et al., 2015) in nascent soot particles. These particles are characterised by the concurrent presence of well-organised and amorphous regions. Many hypotheses have been advanced (see 3.2). The most intriguing one is that the order arises due to stacking of planar PAHs to form parallel atomic layers; the disorder is due to the presence of randomly oriented and/or non-planar PAHs. The hypothesis is also corroborated by the evidence that the combustion environment, in which particles are formed, produces different amounts and types of PAHs, including large amount of non-planar PAHs, i.e. those containing a 5-membered ring or an alkyl-side chain or covalent σ -bonds, so that their role in soot inception cannot be excluded a priori (Ciajolo, D'Anna and Barbella, 1994) (Ciajolo et al., 1998).

In this chapter, a study of the evolution of different PAHs and additional analysis to obtain information on the morphology of the forming clusters were made using a molecular dynamics (MD) approach. Simulations of homomolecular systems of PAHs were performed using a MD software (GROMACS), at temperatures of 500 K, 1000 K and 1500 K.

Two different types of PAH molecules were analysed in order to understand if they exhibit a different clusterization propensity: peri-condensed aromatic hydrocarbons (PCAHs), namely pyrene ($C_{16}H_{10}$) and coronene ($C_{24}H_{12}$), and aromatic molecules containing pyrene and coronene connected with a σ -bond, dipyrene ($C_{32}H_{18}$) and dicoronene ($C_{48}H_{22}$), representative of aromatic aliphatic linked hydrocarbons (AALHs). Moreover, MD can help understanding if the clustering of these two types of PAH molecules results in different morphologies of the nascent particles.

MD allows to treat the nucleation in a physical way; however, the investigation of AALH evolution permits to treat indirectly also the chemical pathway because every ALLH molecule can be viewed as the result of a chemical reaction between PCAH molecules. In fact, the stacking of PAHs could play an important role in particle inception, but, during combustion, a rich radical chemistry takes place, with formation of free radicals, radical additions and

abstractions, hence bond formations that could open the way to possible bridge formations between aromatic parts (see also 3.2).

6.1 Methodology

6.1.1 Precursor molecules

Two different types of PAHs have been detected experimentally in flame environment: Pericondensed aromatic hydrocarbons (PCHs), solely constituted by fully-condensed aromatic islands, and aromatic aliphatic linked hydrocarbon (AALHs), constituted by aromatic molecules linked by σ -bonds (D'Alessio et al., 1992) (Ciajolo et al., 1998). Both classes of molecules were used as starting molecules in the MD simulations. Particularly, the attention was focused on two representative PCHs, pyrene ($C_{16}H_{10}$) and coronene ($C_{24}H_{12}$), and on aromatic molecules containing pyrene and coronene connected by a σ -bond, dipyrene (1,1-pyrenilpyrene, $C_{32}H_{18}$) and dicoronene (1,2-coronilcoronene, $C_{48}H_{22}$), as representative of AALHs (Fig. 6.1).

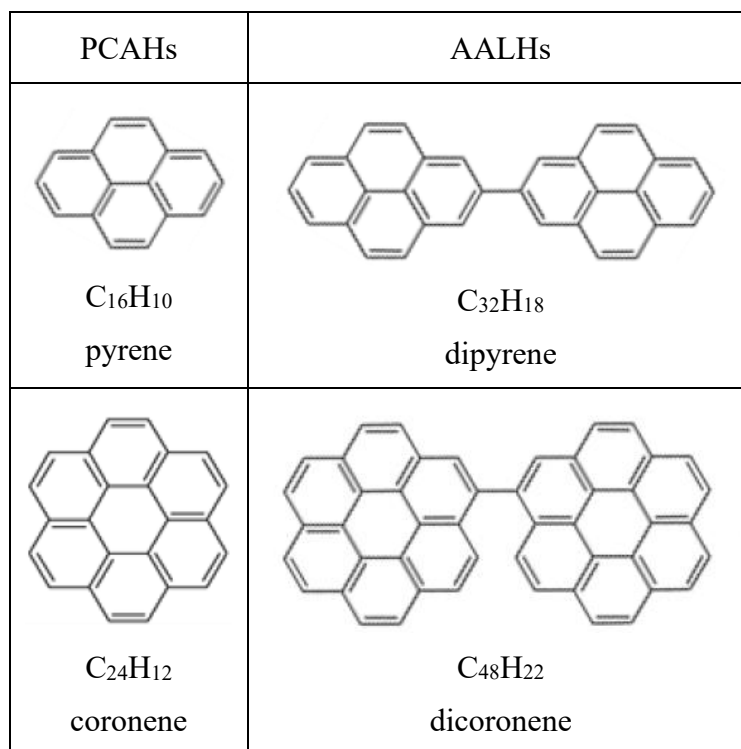


Figure 6.1 Schematic representation of PAHs molecules used as input.

In the following they are indicated as pyr (pyrene), cor (coronene), dpr (dipylene) and dcr (dicoronene). The presence of the σ -bond allows the relative bending and rotation of the aromatic sub-units in the AALH molecules, giving a more flexibility to the structure.

These four molecules are characterized by different masses and molecular structures. They were chosen in order to understand the effect of size and type of precursor molecules on the clusterization and on different morphology of the nascent particles.

6.1.2 MD simulations

MD simulations were performed using GROMACS v4.6 (Hess et al., 2008). Homomolecular systems of the four different aromatic molecules were simulated at temperatures of 500 K, 1000 K and 1500 K using the canonical NVT ensemble (Number, Volume and Temperature) that ensures a constant temperature during the simulations. Velocities and positions of all atoms in the system were obtained solving Newton's equation of motion. The simulations were performed by using the velocity Verlet algorithm (Verlet, 1967) as integration method, with an integration time step of 1 fs, coupled with a Nosè-Hoover thermostat (Nosè, 1984) with a time constant of 0.05 ps, according to best practice in literature for these systems (Totton, Misquitta and Kraft, 2012).

In each simulation, 1000 molecules of pyrene or coronene or 500 molecules of dipylene or dicoronene were initially casually located in a cubical box (Fig. 6.2). The different number of initial molecules ensured a constant number of aromatic sub-units in the systems because dipylene and dicoronene have both two aromatic sub-units inside the molecule.

The molecule concentration was $2 \cdot 10^{18}$ PAHs/cm³. This concentration value is not reasonable; it is much higher than that found in a flame environment but allows us to follow the clusterization events on a much shorter timescale. Indeed, according to the Eq. (6.1) (Chung and Violi, 2010):

$$\Delta t_{real} \approx \Delta t_{MD} \left(\frac{n_{MD}}{n_{real}} \right)^2 \quad (6.1)$$

each nanosecond of simulation at $2 \cdot 10^{18}$ PAHs/cm³ corresponds to 4 ms for a concentration of $1 \cdot 10^{15}$ PAHs/cm³, typical of rich hydrocarbon flames (Chung and Violi, 2007).

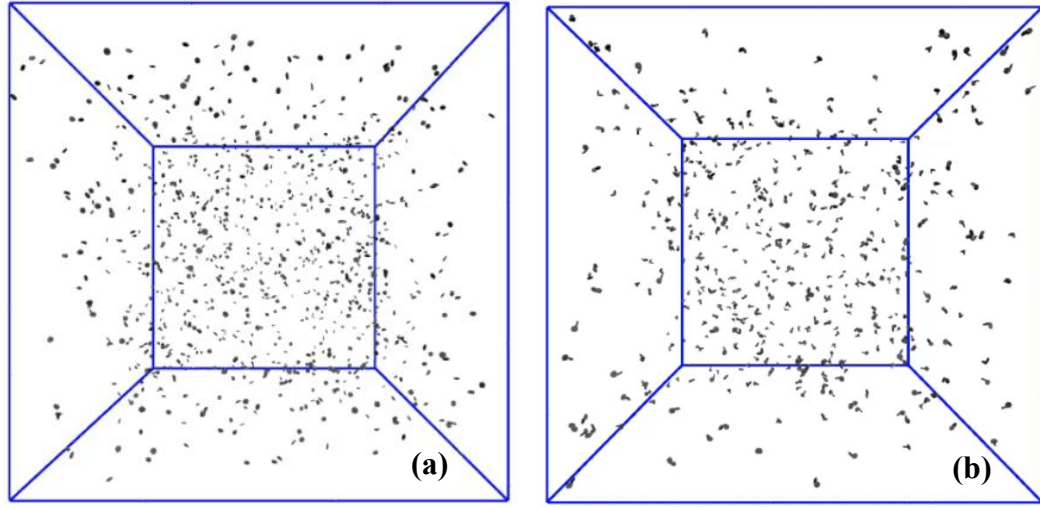


Figure 6.2 Starting simulation box: (a) coronene system (1000 molecules) (b) dicoronene system (500 molecules). The box length is 79.4 nm.

The initial velocities were generated by a Maxwell-Boltzmann distribution at the reference temperature. Simulations were run for 6 ns. The chosen simulation time allows the formation of the dimers and their evolution towards larger clusters, differently from other MD works where the simulation time adopted is 1 ns (Chung and Violi, 2011) (Totton, Misquitta and Kraft, 2012).

6.1.3 Interaction potential function

The interaction potential U were computed as sum of the non-bonded and the bonded terms (Eq. 5.7). For the intramolecular interactions, the OPLS-AA (optimized potential for liquid simulations-all atom) force field parameters for bonds, angles and dihedrals were used (Kaminski et al., 2001). The non-bonded term ($U_{\text{non-bonded}}$) is sum over all pairwise atomic interaction, U_{ab} , between molecules (Eq. 5.8). U_{ab} , is function of the atom-atom separation r_{ab} . It contains a repulsion term and a dispersion term expressed as Lennard-Jones (LJ) potential form (Eq. 6.2):

$$U_{ab}(r_{ab}) = 4 \epsilon_{ab} \left(\left(\frac{\sigma_{ab}}{r_{ab}} \right)^{12} - \left(\frac{\sigma_{ab}}{r_{ab}} \right)^6 \right) \quad (6.2)$$

The parameters σ_{ab} and ϵ_{ab} used for the Lennard-Jones potential are reported in Table 1. These parameters were calculated by fitting the position and depth of the minima of the iso-PAHAP potential of Kraft and co-workers (see also 5.4.3) (Totton, Misquitta and Kraft, 2012).

Table 6.1 LJ potential parameters.

parameters	C-C	C-H	H-H
σ_{ab} [nm]	0.3516	0.3029	0.3
ϵ_{ab} [kJ/mol]	0.2599	0.2257	0.0729

The electrostatic interactions were neglected. This choice is related to the long simulation time performed (6 ns) and the high computational cost that the calculation of the long-range electrostatic term requires. In this way, the computational cost of each trajectory is about 24 h on four-processor machine. As it will be possible to see in Chapter 7 comparing the results obtained considering and neglecting the electrostatic term, the electrostatic interactions did not remarkably affect the cluster formation propensity. The percentage of clustered molecules considering the electrostatic term is slightly lowered (Fig.7.3) and morphological aspects of cluster formed present some differences (Fig. 7.7). However, the approximation introduced when the electrostatic term were neglected, allowed to significantly speed up the simulations that would require many days when the electrostatic interactions are considered.

6.1.4 Simulation output and cluster identification

The output of the simulations is a trajectory up to 6 ns that represented the time evolution of all the atoms locations and velocities. Five trajectories for each PAHs system were run and all the data were averaged over these runs. The number of runs allowed to have a statistically converged mean; a larger number of runs did not significantly change the results or reduce the error bars. Once the spatial location of all atoms, hence of all molecules, was known from trajectories, clusters were identified. For identifying a cluster, it was necessary to define a cut-off distance (r_{crit}) measured between molecule centers of mass and a critical period of time (t_{crit}).

Two molecules were considered in the same cluster if the distance of their centers of mass was lower than r_{crit} for a time longer than t_{crit} . If the distance of their centers of mass was lower than r_{crit} for a time shorter than t_{crit} , the cluster was considered unstable and not counted for. In this work, according to literature (Totton, Misquitta and Kraft, 2012), stable clusters were identified by using $r_{\text{crit}}=1.2$ nm and $t_{\text{crit}}=16$ ps. Larger critical distances and interaction times did not modify significantly the results. The count of the clusters allowed to track total clustering vs time and to evaluate the cluster efficiency for the given system.

6.1.5 Structural Analysis

Despite of the large efforts in the understanding PAH clustering with MD approaches, there is a lack of systematic structural analysis of the formed clusters. A systematic analysis of the cluster morphology and of the internal structure was performed by introducing new tools and parameters. The internal structure of the clusters was analysed by calculating the distances between centres of masses of molecules in the same clusters. It was possible to retrieve an internal distance distribution (IDD). IDD is a good indicator of the internal structure but does not give information on the morphology of the formed clusters, as better evidenced in the next section. In order to gain insights on the cluster morphology, a structural parameter obtained from the inertia tensor was introduced. The inertia tensor can describe cluster structure because cluster can be viewed as a rigid discrete assembly of point masses, corresponding to the single atoms. The inertia tensor was easily calculated for all the clusters since each one can be calculated by fixing the Cartesian coordinate system to be the principal axes of the structure; in these conditions, the inertia tensor is diagonal and the values on the diagonal represent the principal moments of inertia (I_a , I_b , and I_c). The principal moments of inertia assume specific values depending on the shape of the masses distribution of the three dimensional system considered. Particularly, in the case that the assembly of the points reflects a regular geometrical shape, the principal moments of inertia (I_a , I_b , and I_c) assume specific reciprocal value. As examples, if the discrete system assumes the shape of a cylinder, the principal moments of inertia results $I_a \neq I_b = I_c$, i.e., one preferential direction; if the discrete system assumes the shape of a sphere, the principal moments of inertia results $I_a = I_b = I_c$, i.e., no preferential directions. In order to plot and analyse simultaneously the principal moments of inertia, a structural parameter, P , was introduced, defined as:

$$P = \frac{I_b - I_a}{I_c} \quad \text{where} \quad I_a < I_b < I_c \quad (6.3)$$

It is worth to note that it is always possible to reorder the three moment of inertia in order to obtain $I_a < I_b < I_c$, without affecting the results (it is equivalent to rotate the Cartesian coordinate system). By definition, P approaches the unit value for a cylinder with height (H) much bigger than the diameter (D), i.e., $H/D \gg 1$, and it is zero for a perfect homogenous sphere. As for the IDD, there is no other way reported in literature to systematically compare the morphology of the formed clusters rather than presenting some selected images. The use of the P parameter allowed us to gain information and easily visualize morphology of the clusters.

6.2 Results and discussion

Figure 6.3 reports the percentage of stable clustered molecules as a function of MD time for the four different systems investigated at temperatures of 500 K, 1000 K and 1500 K.

As temperature increases, the percentage of stable clustered molecules decreases for all the systems simulated. In the pyrene, dipyrene and coronene cases, this percentage is negligible already at 1000 K, whereas the dicoronene system shows a significant, although low, clusterization even at 1500 K. This first result evidences the weak capability of small PAHs to form stable clusters at high temperature. On the other side, all the considered PAHs show a fair capability to form clusters at 500 K.

In all the systems at 500 K the percentage of clustered molecules increases with time and with the size of the analysed molecules. This latter result is a consequence of the higher interaction potential for coronene with respect to pyrene.

In the coronene system, the amount of clustered molecules grows approximately linearly up to 70% of cluster formation and it reaches a value around 90%, after 6 ns. For amount larger than 70% of clustered molecules, the linearity is lost, probably due to the lack of free molecules to add to the clusters. As regards pyrene, very few pyrene dimers form (8%), even at 500 K.

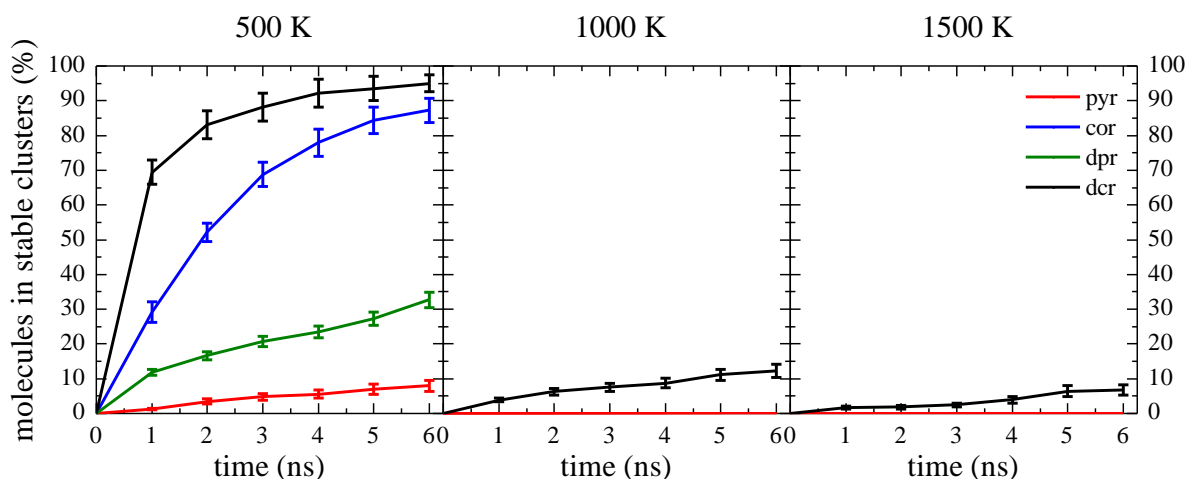


Figure 6.3 Percentage of clustered molecules vs MD time for pyrene (red line), coronene (blue line), dipyrene (green line) and dicoronene (black line) at 500 K (left), 1000 K (middle) and 1500 K (right). The error bars represent the deviation of the data sets from the mean values (deviation less than 12% in all the cases).

The σ -bonded molecules show a higher clusterization propensity than the respective PCAHs. The percentage of clustered molecules are more than two times higher in the dipyrene system with respect to pyrene and it is slightly higher in dicoronene with respect to coronene. The strongest clusterization of σ -bonded molecules (AALHs) with respect to PCAHs is probably associated with the capability of the σ -bond to accommodate the collision energy through vibrations, bending and rotations around the σ -bond increasing the lifetimes of formed cluster. Comparing the results of coronene and dipyrene at 500 K, it appears that dipyrene has a lower clusterization propensity respect to coronene. Both molecules have a comparable number of aromatic rings, although dipyrene has a mass larger than coronene (402 amu and 300 amu, respectively). This result suggests that σ -bond although having a positive effect on the clustering, however cannot overtake the effect of the size of aromatic sub-units in the clustering molecules. In fact, despite of the larger mass, in the dipyrene the presence of two smaller aromatic sub-units with respect to the aromatic unit of coronene reduces the capability of molecules to interact.

All the systems, except for dicoronene system, do not form clusters at 1000 K and 1500 K; for this reasons all the other results are presented at 500 K in order to have a comparison of the obtained results between of all the systems investigated.

Figure 6.4 reports the number of stable clusters formed as a function of MD time for the four different systems investigated at 500 K.

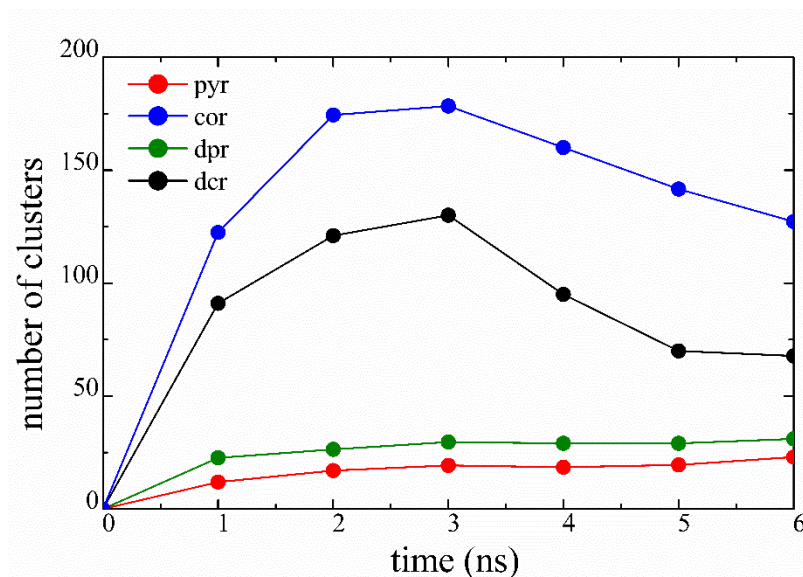


Figure 6.4 Number of clustered molecules vs MD time for pyrene (red line), coronene (blue line), dipyrene (green line) and dicoronene (black line) at 500 K (the deviation of the data sets from the mean values is less than 10% in all the cases).

The number of clusters formed in the coronene and dicoronene systems initially rapidly increases, reaching a maximum at 3 ns of simulation and successively it slowly decreases. The decrease of the number of clusters is a net result of cluster formation and cluster coagulation. Cluster formation, i.e., when two free molecules stack together, increases the number of clusters, while cluster coagulation, i.e., the collision between two clusters to form a bigger one, decreases the number of clusters. Initially cluster formation prevails over cluster coagulation, due to the large amount of free molecules in the system. Successively, when cluster coagulation becomes predominant, due to the increase in number of formed clusters, the number of clusters decreases.

Figure 6.5 shows the cluster size distribution (CSD) defined as:

$$CSD(x) = \frac{\text{number of cluster with size } x}{\text{total number of clusters in the system}} \cdot 100 \quad (6.4)$$

The cluster size is equal to the number of monomers present globally in the cluster. The aromatic sub-unit is considered as monomer to distinguish them from molecules, that can be composed by one (PCAHs) or two (AALHs) monomers.

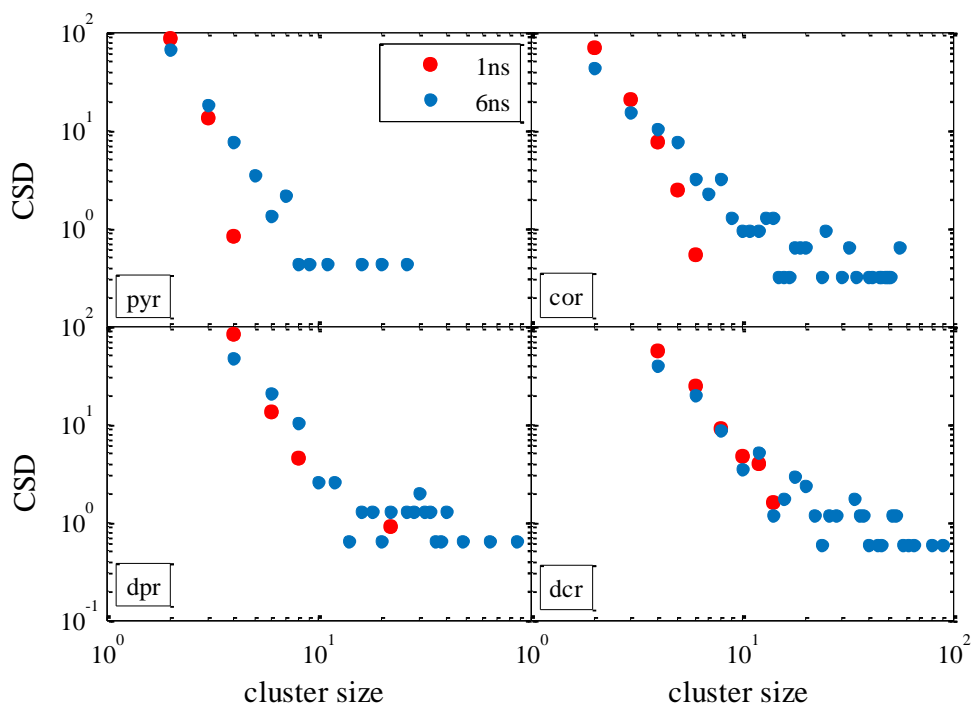


Figure 6.5 CSDs for pyrene (top-left), coronene (top-right), dipyrene (bottom-left) and dicoronene (bottom-right) after 1 ns (red circles) and 6 ns (blue circles) of MD time at 500K.

It is possible to note that in the coronene and dicoronene systems, clusters reach larger sizes up to 50 monomers and 100 monomers, respectively, after 6 ns of MD time, suggesting a more effective coagulation process taking place. In the pyrene and dipyrene systems, the number of clusters increases continuously with time (Fig. 6.4) suggesting that cluster formation rate is always faster than cluster coagulation. CSD confirms this behaviour showing values significantly smaller comparing pyrene with coronene and dipyrene with dicoronene.

In all systems, CDSs evolve towards the formation of clusters of increasing sizes. For the pyrene system, the amount of particle larger than 10 monomers remains negligible also after 6 ns. On the contrary, in the other systems, the formation of clusters of larger size is clearly visible, although a large part of the clusters is mainly constituted by 2-4 monomers.

Additional analysis have been made to have a quantitative description of cluster internal structure and shape. Cluster morphology has been analysed by calculating the distances between centers of mass of monomers in the same clusters. Figure 6.6 reports the IDD of the clusters formed after 6 ns for all PAHs at 500 K.

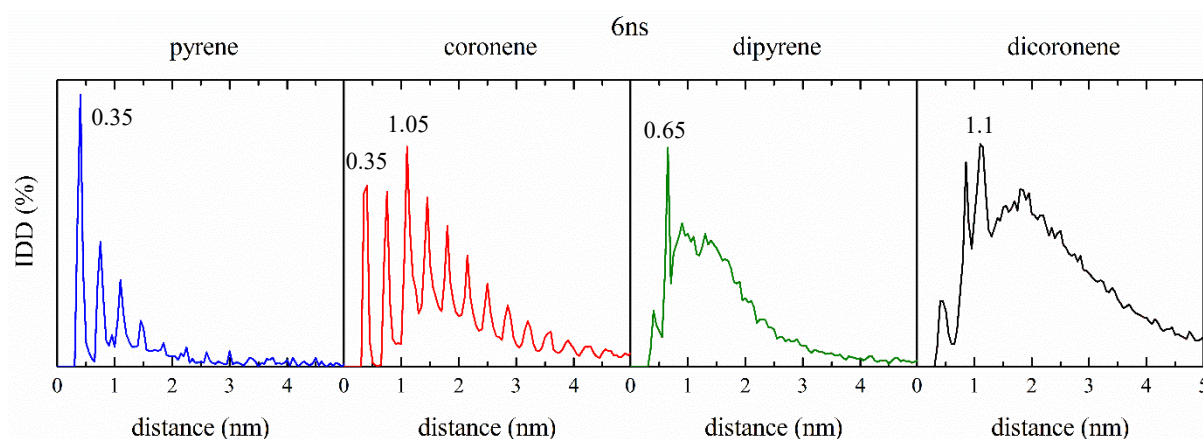


Figure 6.6 IDD after 6 ns of MD time at 500 K. From left to right: pyrene, coronene, dipyrene, dicoronene.

In PCAH clusters (pyrene and coronene), the presence of recurring peaks in the IDD can be linked with an ordered structure. The characteristic distance is 0.35 nm, i.e., the distance where the minimum of the LJ interaction potential is located. In the pyrene system, the major peak is at 0.35 nm. Peaks recur every 0.35 nm in the IDD with an intensity that decreases with distance. This is due to a stacked arrangement of the molecules in the structure. Coronene shows a similar trend; the peaks are located at the same distances as pyrene. However, in the coronene system, the major peak is located at around 1.05 nm, which is a multiple of 0.35 nm and incidentally also corresponds to the distance between two coronene molecules placed side by side. Looking at the distance distribution function for σ -bonded molecules in Fig. 3, the peaks mostly disappear and a broad IDD can be seen. It is still possible to see the peak at 0.35 nm due to the LJ interaction potential; also, the peaks of the internal distance of the monomer (0.6 nm for pyrene and 1.1 nm for coronene) are evident. Finally, in the coronene case, a peak at 0.7 nm can be distinguished, suggesting that a large number of stacks of 3 monomers are still present within the clusters. This latter result suggests that in dicoronene the cluster structure is characterized by the concurrent presence of well-organized regions (clearly identified distances among molecules) and amorphous regions (broad distribution of the IDD).

In Fig. 6.7, clusters sections obtained using RasMol software (Sayle and Milner-White, 1995) are compared to HR-TEM images of a nascent soot particle (Alfè et al., 2009). The σ -bonded molecule clusters show a good similarity with experimental images. From the images of the clusters, it is clearly visible that PCAHs form more organized structures and they tend to assume

cylindrical shape. On the contrary, the σ -bonded molecules clusters exhibit a more spherical morphology.

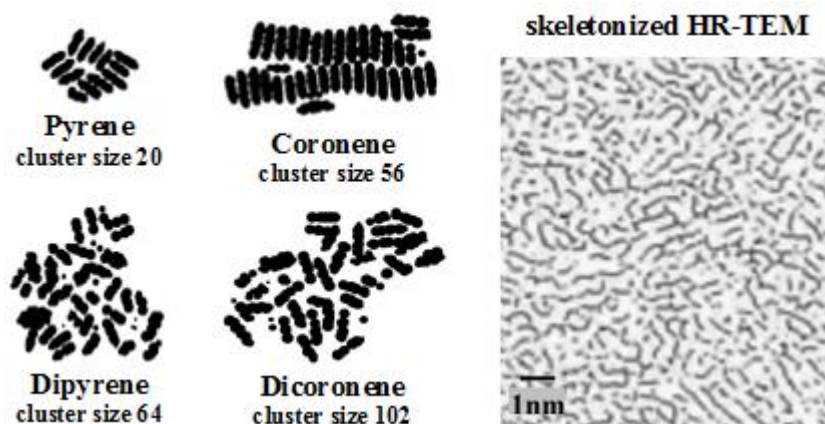


Figure 6.7 Cluster sections obtained with RasMol (Sayle and Milner-White, 1995) and HR-TEM image of nascent ethylene soot adapted from Ref. (Alfè et al., 2009).

As indicator of shape of clusters, in Fig. 6.8 the structural parameter P , defined in section 6.1.5, is reported for the clusters formed in all the examined conditions after 6 ns at 500K. In the same figure, the parameter P calculated for clusters perfectly stacked and hence arranged in a cylindrical shape (solid) and disordered (dashed) clusters are reported to help in discerning the shape of the analysed clusters.

The perfectly stacked clusters can be viewed as the most ordered structure possible to achieve; as expected, the parameter P tends to 1 for larger sizes of the clusters, i.e., as H/D increases and the cylindrical approximation is approached.

Differently from the cylindrical shape for the ordered structures, it is not possible to uniquely define a structure for the disordered clusters. In order to overtake this problem, for each cluster size a hundred randomly clusters have been generated. These clusters have been generated starting from a pyrene (pyrene and dipyrene cases) or a coronene (coronene and dicoronene cases) molecule and randomly adding the same molecules to the clusters assigning the position of the center of mass and the molecule orientation. Every new molecule so added is hence effectively considered in the cluster if it follows these two conditions:

- all the atoms of the molecule added to the cluster must stay at a minimum distance of 0.2 nm respect to all the other atoms of the molecules already present in the cluster;

- at least one atom of the new added molecules must stay at a distance lower than 0.4 nm respect to at least one atom of the molecules already present in the cluster.

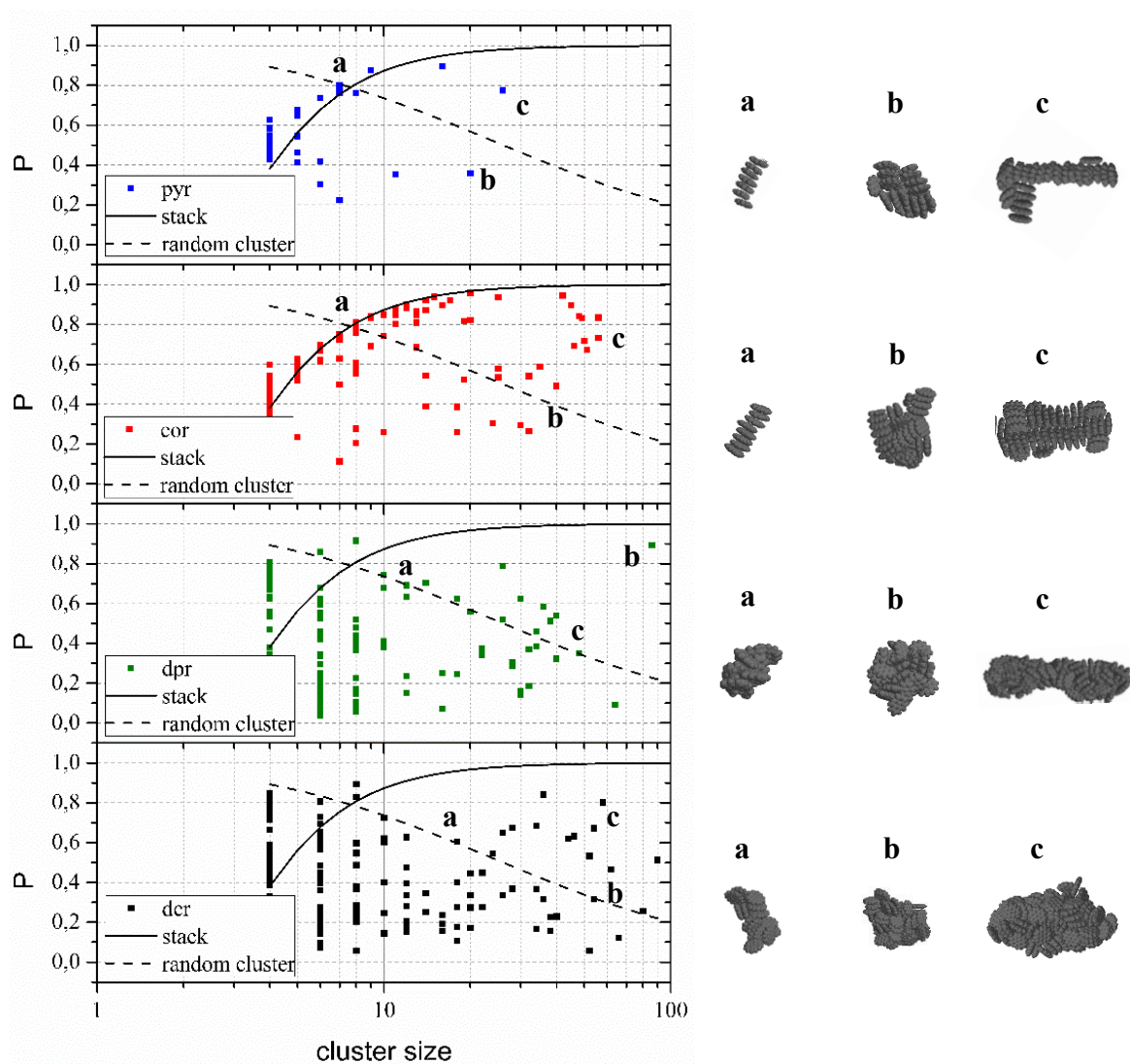


Figure 6.8 Structural parameter P for pyrene (blue), coronene (red), dipyrene (green) and dicoronene (black) after 6 ns of MD time at 500 K. Continuous line (top) represents parameter P for ordered stacked clusters; dashed line (bottom) represents the maximum value of parameter P for randomly generated clusters.

The P parameter so evaluated represents the maximum value of the structural parameter P calculated for all the clusters randomly generated for each cluster size. For a small cluster size (up to 10 molecules) the arrangement can vary in a big range of possible shapes, and P assumes values as large as 0.8. As the size increases, the arrangements approach spherical shapes, and

the value of P approaches zero. The choice of the two distances in the cluster random generation (0.2 and 0.4 nm), although affecting the shape of each individual cluster generated, does not significantly change the trend of the dashed line reported in Fig. 6.8. It is worth to remind that the randomly generated clusters have not a physical meaning but are used here only to generate a guideline to compare the structure of the cluster effectively formed during the MD simulation.

The P values of PCAHs clusters are mainly located around the continuous line confirming a “stacked” or cylindrical shape. This is in accordance with the images showed in Fig. 6.7 and in Fig. 6.8. For clusters larger than 20 monomers, P decreases: this behaviour is linked to the presence of bi-cylindrical clusters or clusters including small stacks that approach a spherical shape. The P of σ -bonded molecules clusters is mainly located below the dashed line of randomly generated clusters. This suggests that their arrangement rapidly approaches a spherical shape as confirmed from cluster images in the insets. Some clusters show a P value above the dashed line, due to the presence of elongated structure, probably a result of coagulation of smaller spherical clusters not completely merged.

In conclusion, the presence of the σ -bond in the starting monomers not only increase the clusterization propensity of the investigated system (dicoronene molecules are the only one to clusterize at flame temperature) (Fig. 6.3), but also increases the amount of disorder and the sphericity of the formed particles (Fig 6.6 and 6.8), making their structure more similar to the one found experimentally (Fig. 6.7). Therefore, it appears that the chemical structure of precursor PAH molecules controls the morphology of the particles, suggesting that AALHs can play an important role in the nucleation process.

7. MD simulations of PAH stacking: influence of the intermolecular potential

The choice of the intermolecular potential to use in the MD simulations is critical. Different results are in fact mainly affected by this choice, as it is possible to see in similar works of combustion-generated particle nucleation using MD (Chung and Violi, 2011) (Totton, Misquitta and Kraft, 2011).

The aim of this Chapter is hence to study the effect of intermolecular forces with different function forms and parametrization not only on the global clustering behaviors but also on the morphology of the formed clusters. Four intermolecular potentials, which differ for their function forms and parametrization of the interaction involved, were selected in order to outline the difference results obtained.

For the first time, statistical analysis of the morphology of the formed cluster were reported. The homo-molecular coronene ($C_{24}H_{12}$) cluster formation at a temperature of 500 K were analysed using a MD software (GROMACS). The internal organization and shape of the clusters were systematically analysed to show the main differences related to the intermolecular potential function used. The use of a systematic approach to analyse the internal structure and shape of the formed cluster allowed to have a better comparison between the potentials and their capability to reproduce realistic configurations.

Few works on cluster morphology are present in the literature. Rapacioli et al. have studied the most stable configurations of clusters of PAHs using a global optimization approach (Rapacioli et al., 2005). Clusters of PAHs have been modelled using the LJ potential parametrization of Van de Wall (Van de Waal, 1983). Kraft and co-workers have done a similar work where they presented a study of the clusters assembled from PAHs molecules similar in size to small soot particles using a stochastic ‘basin-hopping’ global optimization method (Totton et al., 2010). Most of these studies report calculations of potential energy of pre-assembled PAH clusters to outline what are the lowest-energy cluster structures. Systematic or statistic studies of the morphology of the clusters dynamically formed from PAH clustering has not been done, yet. Cluster morphology represents a key aspect and it is crucial in determining the reactivity of the formed condensed structures.

7.1 Methodology

7.1.1 MD simulations

Cluster formation and evolution from a gas-phase homo-molecular system of coronene molecules at fixed temperature of 500 K were simulated using the canonical NVT ensemble (Number, Volume and Temperature). Coronene ($C_{24}H_{12}$) was selected as starting molecule instead of pyrene ($C_{16}H_{10}$), due to the low clusterization propensity of the latter also at low temperature (see Chapter 6). A low temperature (500 K) was chosen to simulate the systems, in order to have a large number of formed clusters, necessary to carry out a statistical analysis of the cluster morphology. As reported in Chapter 6 and in other papers (Chung and Violi, 2011) (Totton, Misquitta and Kraft, 2012), the choice of a higher temperature does not lead to the formation of a significative number of clusters; a good analysis of cluster morphology is hence not allowed.

MD simulations were performed using GROMACS v4.6 (Hess et al., 2008). Velocities and positions of all atoms in the system were obtained solving Newton's equation of motion. The simulations were performed by using the velocity Verlet algorithm (Verlet, 1967) as integration method, with an integration time step of 1fs, coupled with a Nosé-Hoover thermostat (Nosé, 1984) with a time constant of 0.05 ps, according to best practice in literature for these systems (Totton, Misquitta and Kraft, 2012).

In each simulation, 1000 molecules of coronene were initially casually located in a cubical box. The molecule concentration was $2 \cdot 10^{18}$ PAHs/cm³, a concentration value not reasonable, but as already described in section 6.1.2, each nanosecond of simulation at $2 \cdot 10^{18}$ PAHs/cm³ corresponds to 4 ms for a concentration of $1 \cdot 10^{15}$ PAHs/cm³, typical of rich hydrocarbon flames (Chung and Violi, 2007).

Simulations were run for 3 ns and the initial velocities were generated by a Maxwell-Boltzmann distribution at the reference temperature. The chosen simulation time allows the formation of the dimers and their evolution towards larger clusters.

7.1.2 Interaction potential function

The interaction potential is sum of a bonded term and a non-bonded term (see also 5.4.1). For the bonded term, i.e. the intramolecular interactions, the OPLS-AA (Optimized Potential for Liquid Simulations-All Atom) force field parameters for bonds, angles and dihedrals were used (Kaminski et al., 2001). The non-bonded term ($U_{\text{non-bonded}}$) is sum over all pairwise atomic interaction, U_{ab} , between molecules (Eq. 5.8). U_{ab} is function of the atom-atom separation r_{ab} and it contains a repulsive term and attractive term that describe the Van der Waals interactions ($U_{\text{ab}}^{\text{VdW}}$) and an electrostatic interaction term ($U_{\text{ab}}^{\text{Coulomb}}$) (Eq.5.9).

To explore the effect of intermolecular potentials on the dimerization of coronene and on larger cluster formation, four intermolecular pairwise atomic interaction, U_{ab} , were compared.

To describe the Van der Waals interactions, three of the four intermolecular potential investigated were used in literature papers (Chung and Violi, 2010) (Chung and Violi, 2011) (Iavarone et al., 2017) (Totton, Misquitta and Kraft, 2012); the forth one has been introduced in this study.

The four intermolecular potentials $U_{\text{ab}}^{\text{VdW}}$ are listed below:

- f_1 : a Buckingham potential form (exp-6 potential) developed by Williams (Williams and Starr, 1977) and used by Miller and co-workers to calculate binding energies of homo-molecular and hetero-molecular dimers and homo-molecular clusters of eight PAH molecules ranging from 128 to 666 Da, arranged in stacks containing from two to nine molecules (Herdman and Miller, 2008);
- f_2 : a Lennard-Jones (12-6 potential) parametrization developed by Van de Waal (Van de Waal, 1983) by fitting the position and depth of the minima of the Buckingham potential sets of Williams (Williams and Starr, 1977) and used by Violi and co-workers to simulate by MD the clustering behaviour of several aromatic molecules at different temperatures (Chung and Violi, 2010) (Chung and Violi, 2011);
- f_3 : the iso-PAHAP potential developed by Kraft and co-workers has been used to simulate by MD the clustering behaviour of several PAHs with sizes ranging from pyrene ($\text{C}_{16}\text{H}_{10}$) to circumcoronene ($\text{C}_{54}\text{H}_{18}$) at different temperatures (Totton, Misquitta and Kraft, 2012);
- f_4 : a Lennard-Jones potential which parameters are calculated by fitting the position and depth of the minima of the iso-PAHAP potential of Kraft and co-workers (this work). This

potential has also been used to study the evolution of PCAHs and AALHs in the previous Chapter.

The parameters and the form of the interaction potentials are reported in Table 7.1.

Explicit electrostatic models were added to the potential forms based upon partial atom-centered point charges, q_a and q_b . The electrostatic potential (U_{ab}^{Coulomb}) between pairs of atoms is calculated from Eq. (7.3).

$$U_{ab}^{\text{Coulomb}} = \left(1389.963 \frac{\text{kJ } \text{\AA}}{\text{mol } e^2} \right) \frac{q_a q_b}{r_{ab}} \quad (7.3)$$

The electrostatic interaction is a long range potential and Particle Mesh Ewald (PME) method was used to compute this term (Darden, York and Pedersen, 1993). Three charge sets, reported in Table 2, were taken from classical MD works, where the evolution of coronene was studied; the calculation method adopted for each set is described in the respective references (Table 7.2).

The global interactions tested in this paper, sum of attractive-repulsive forces and the electrostatic contribution, are reported in Table 7.3. The choice of the combinations was made in order to reproduce the same intermolecular potential used in similar MD works on coronene clusterization (Herdman and Miller, 2008) (Chung and Violi, 2011) (Totton, Misquitta and Kraft, 2012). For the potential adopted in this work, because it was built on the fitting of the iso-PAHAP, the correspondent electrostatic interaction has been chosen.

The resulting intermolecular potentials $U_{\text{non-bonded}}$ are reported in Fig. 7.1 for a face-to-face coronene dimer configuration in order to have a first comparison between the intermolecular potential functions considered.

The potential well depths of iso-PAHAP and LJfit-iso functions are equal. They show differences in the repulsive branch which results in a weaker repulsive interaction in the iso-PAHAP potential. This difference is mainly due to the different form used in the two potentials. The LJfit-iso we have introduced in this paper is used to examine differences and similarities on the clustering behaviour and on cluster morphology using two potential functions with equal potential depths and different forms. It is beyond the purpose of this paper to introduce a new intermolecular potential, knowing how important it is to replicate the intermolecular interactions.

Table 7.1 Function forms and parameters of the four attractive-repulsive (U_{ab}^{VdW}) terms tested.

Name	Intermolecular potential form	Parameter	CC	CH	HH	Ref.
f ₁	$U_{ab}^{vdw}(r_{ab}) = B_{ab}\exp(-C_{ab}r_{ab}) - \frac{A_{ab}}{r_{ab}^6}$	A _{ab} [kJnm ⁶ /mol] B _{ab} [kJ/mol] C _{ab} [1/nm]	2376.5 349908 0.360	523.0 36677 0.367	114.2 11104 0.374	(Williams and Starr, 1977)
f ₂	$U_{ab}^{vdw}(r_{ab}) = 4\varepsilon_{ab}\left(\left(\frac{\sigma_{ab}}{r_{ab}}\right)^{12} - \left(\frac{\sigma_{ab}}{r_{ab}}\right)^6\right)$	σ_{ab} [nm] ε_{ab} [kJ/mol]	0.3475 0.3926	0.3208 0.1435	0.2937 0.0543	(Van de Waal, 1983)
f ₃	$U_{ab}^{vdw} = Ge^{-\alpha_{ab}(r_{ab}-\rho_{ab})} - f_6(r_{ab})\frac{C_{6ab}}{r_{ab}^6}$ $f_6(r_{ab}) = 1 - e^{-\beta r_{ab}}\sum_{k=0}^6\frac{(\beta r_{ab})^k}{k!}$	β [1/nm] G [kJ/mol]	31.1521 2.6255			(Totton, Misquitta and Kraft, 2012)
		ρ_{ab} [nm] α_{ab} [1/nm] C _{6ab} [kJnm ⁶ /mol]	0.3198 35.4947 0.00174	0.2623 33.1836 0.00072 7	0.218 26.5374 0.00030 1	
f ₄	$U_{ab}^{vdw}(r_{ab}) = 4\varepsilon_{ab}\left(\left(\frac{\sigma_{ab}}{r_{ab}}\right)^{12} - \left(\frac{\sigma_{ab}}{r_{ab}}\right)^6\right)$	σ_{ab} [nm] ε_{ab} [kJ/mol]	0.3516 0.2599	0.3029 0.2257	0.3 0.0729	this work

Table 7.2. Values expressed in elementary charge (e) units used in charge sets.

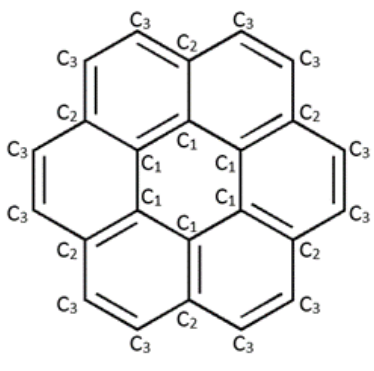
	Name	C ₁	C ₂	C ₃	H	Ref.
	q ₁	-0.003	0.051	-0.126	0.099	(Herdman and Miller, 2008)
	q ₂	-0.016	0.1	-0.143	0.085	(Chung and Violi, 2011)
	q ₃	-0.01	0.182	-0.240	0.154	(Totton, Misquitta and Kraft, 2011)

Table 7.3. Intermolecular potentials, sum of dispersive forces reported in Table 7.1 and the electrostatic term in which one of three charge sets, listed in Table 7.2, is employed. The first column indicates the name that we use in the following to refer to different potentials.

intermolecular potential (U_{ab})	repulsive and attractive terms (U_{ab}^{VdW})	electrostatic term ($U_{ab}^{Coulomb}$)
W	f1	q1
VdW	f2	q2
iso-PAHAP	f3	q3
LJfit-iso	f4	q3

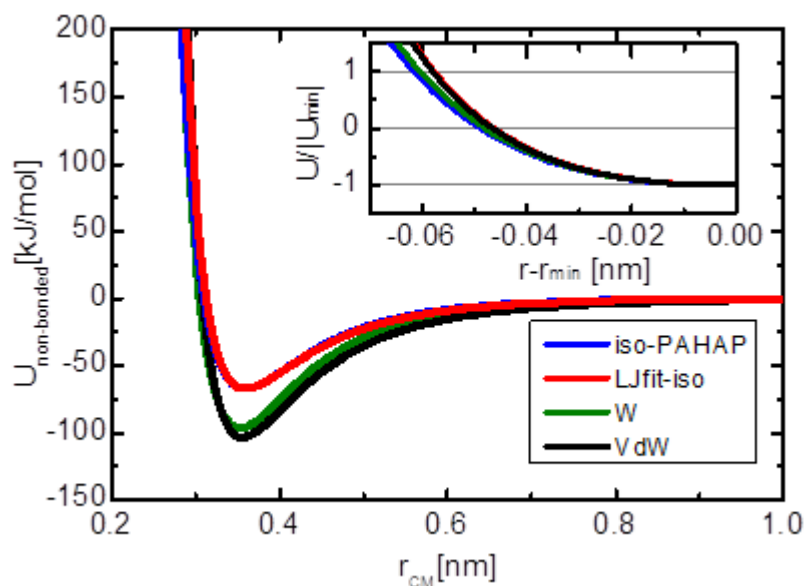


Figure 7.1 Investigated intermolecular potentials (U_{nb}) calculated for a face-to-face coronene dimer configuration. r_{CM} is the distance between centers of mass of the two coronene molecules. Normalized function of the repulsion branches are reported in the inset.

The W and VdW potentials, taken from the literature (Williams and Starr, 1977) (Van de Waal, 1983), are quite similar and the different values of the potential wells are related to the different charge sets employed in the intermolecular potential calculation. These two potentials also show differences in the repulsive branch, resulting in a weaker contribute of the repulsive force in the case of W potential. In both cases, the repulsion term is weaker when a repulsive exponential term is used.

Normalized function of the potential used are reported in the inset in Fig. 7.1. The potential functions were divided for the absolute value of the minimum of the potential functions and reported against the difference between the distance of the two coronene molecules, r , and the distance where the minimum of the potential function is located r_{min} . With this normalization all the minimum values of potential wells coincide and a quick comparison of the repulsive branches is possible. It is possible to see that iso-PAHAP shows the weakest repulsive branch and that the LJfit and the VdW potential are equivalent in the repulsive branch. The relative change of the repulsive branch can be analysed to evaluate its effect on clustering behaviours.

7.1.3 Simulation output and cluster identification

The output of the simulations was a trajectory up to 3 ns that represented the time evolution of all the atoms locations and velocities. Five trajectories for each PAHs system were run and all the data were averaged over these runs. Clusters were identified as described in 6.1.4.

7.1.4 Structural Analysis

Despite of the large efforts in the understanding PAH clustering with MD approaches, there is a lack of systematic structural analysis of the formed clusters. A systematic analysis of the cluster morphology and of the internal structure was performed by introducing new tools and parameters. The internal structure of the clusters was analysed by calculating the distances between centres of masses of molecules in the same clusters. It was possible to retrieve an internal distance distribution (IDD). IDD is a good indicator of the internal structure but does not give information on the morphology of the formed clusters, as better evidenced in the next section. In order to gain insights on the cluster morphology, a structural parameter obtained from the inertia tensor was introduced. This parameter has been described in section 6.1.5.

7.2 Results and discussion

Figure 7.2 reports the percentage of clustered molecules as a function of MD time for the four selected global intermolecular potentials at the temperature of 500 K. The percentage of clustered molecules increases with time and it grows approximately linearly up to 50% of cluster formation, regardless of the potential function used. For larger amount of clustered molecules, linearity is lost, probably due to the lack of free molecules to add to the cluster. The results are similar comparing the iso-PAHAP potential with LJfit-iso potential, and comparing the W potential with VdW potential, suggesting that the clusterization propensity is not affected by the function of intermolecular potential used. The percentage of clustered molecules is 1.5 times higher in the W and VdW potential cases than in the iso-PAHAP and LJfit-iso cases after 3 ns of simulation. The larger cluster formation is directly related to the stronger interaction potential of the W and VdW with respect to the iso-PAHAP and LJfit-iso potentials (see Fig. 7.1).

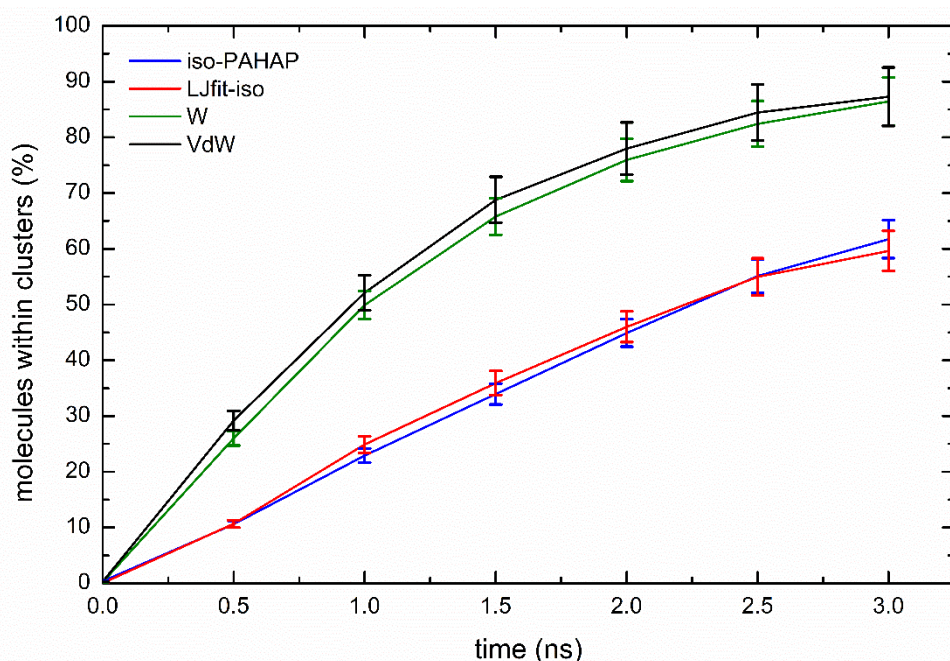


Figure 7.2 Percentage of clustered molecules vs MD time using iso-PAHAP potential, LJfit-iso potential, W potential and VdW potential at 500 K. The error bars represent the deviation of the data sets from the mean values (deviation less than 13% in all the cases).

As already reported in the literature (Chung and Violi, 2011) (Totton, Misquitta and Kraft, 2012), our results show that the cluster formation is strongly dependent on the magnitude of potential interaction, while appears to be weakly dependent of the kind of the adopted potential functions. In fact, iso-PAHAP and LJfit-iso, which share a very similar depth of the intermolecular interaction well (Fig. 7.1) but have two slight different repulsive branch (Fig. 7.1 and Table 7.1), exhibit very similar percentage of clustered molecules. Similar considerations can be carried out on W and VdW potentials.

The total amount of clustered molecules seems to be not remarkably affected by the electrostatic potential as shown in Fig. 7.3 where the percentage of clustered molecules for the four different potentials is reported and compared with the potentials, which neglect the electrostatic forces.

The percentage of clustered molecules considering the electrostatic term is slightly lower in iso-PAHAP and LJfit-iso cases, and it is almost the same in W and VdW systems. The major impact of the electrostatic term in iso-PAHAP and LJfit-iso cases is related to the weaker intermolecular potential. Results obtained by Kraft and co-workers (Totton, Misquitta and

Kraft, 2012) and Violi and co-workers (Chung and Violi, 2011) in the same conditions are also reported in Fig. 7.3 for comparison.

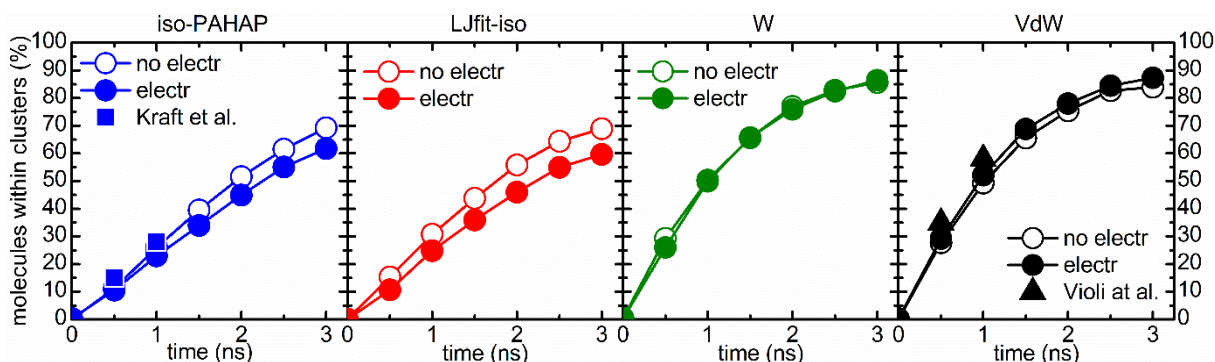


Figure 7.3 Percentage of clustered molecules vs MD time using iso-PAHAP potential, LJfit-iso potential, W potential and VdW potential at 500 K. Filled and empty circles refer to the case of neglecting and considering the electrostatic term, respectively. The square and the triangle refer to the result reported by Kraft and co-workers (Totton, Misquitta and Kraft, 2012) and Violi and co-workers (Chung and Violi, 2011) in the same simulation conditions.

Figure 7.4 reports the number and the mean size of formed clusters as a function of the MD time for the four different potential functions investigated at the temperature of 500 K. The size of a cluster is defined as the number of molecules present in the cluster.

The number of clusters increases rapidly and linearly with the MD time in the first nanoseconds and successively it slowly decreases. The number of clusters formed by using VdW and W potentials increases faster reaching a maximum at 1.5 ns with respect to iso-PAHAP and LJfit-iso in which it reaches the maximum at 2.5 ns. The decrease of the number of clusters is a net result of the cluster formation and the following cluster coagulation.

Cluster formation, i.e., when two free molecules stack together, increases the number of clusters, while cluster coagulation, i.e., the collision between two clusters to form a bigger one, decreases the number of clusters. The sticking of a free molecule on an existing cluster increases the percentage of clustered molecules but leaves the total number of clusters unchanged. Initially, cluster formation prevails over cluster coagulation, due to the large amount of free molecules in the system and the number of clusters linearly increases. Successively, when cluster coagulation becomes predominant, due to the increase of the number of formed clusters (around 160-180 clusters for all the systems), the number of clusters decreases. The result is

supported by the mean size of the clusters, which increases with time. For all the investigated potentials, the increase in the cluster mean size is more evident in W and VdW cases, after 1.5 ns when the number of clusters starts to decrease due to coagulation process: in fact, the formation of a lower number of bigger clusters results in a larger mean size.

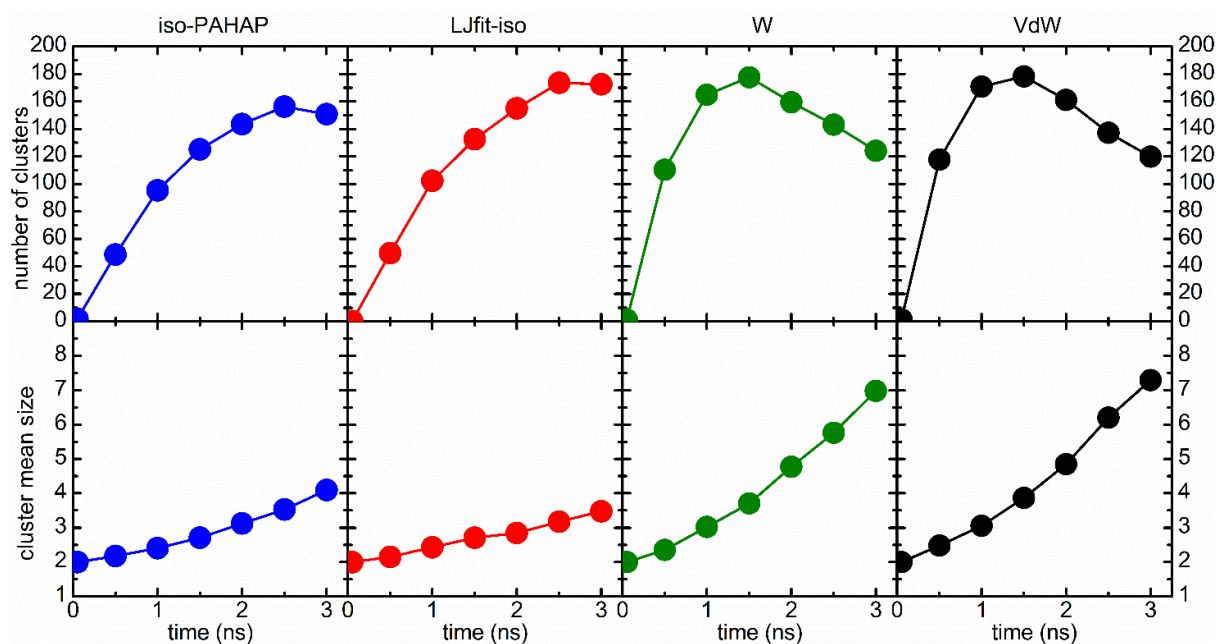


Figure 7.4 Number (top) and the mean size (bottom) of clusters formed vs MD time using iso-PAHAP potential, LJfit-iso potential, W potential and VdW potential at 500 K (the deviation of the data sets from the mean values is less than 8% in all the cases).

In order to better compare results from different potentials, Figure 7.5 reports the number and the mean size of clusters as a function of percentage of clustered molecules for each potential. It is possible to note how the curve collapse on the same master curve for all the investigated potentials up to 60% of cluster formation and only the iso-PAHAP potential shows a slight deviation from the other cases. This suggests that the number and the mean size of clusters are not significantly influenced by the potential intensity used.

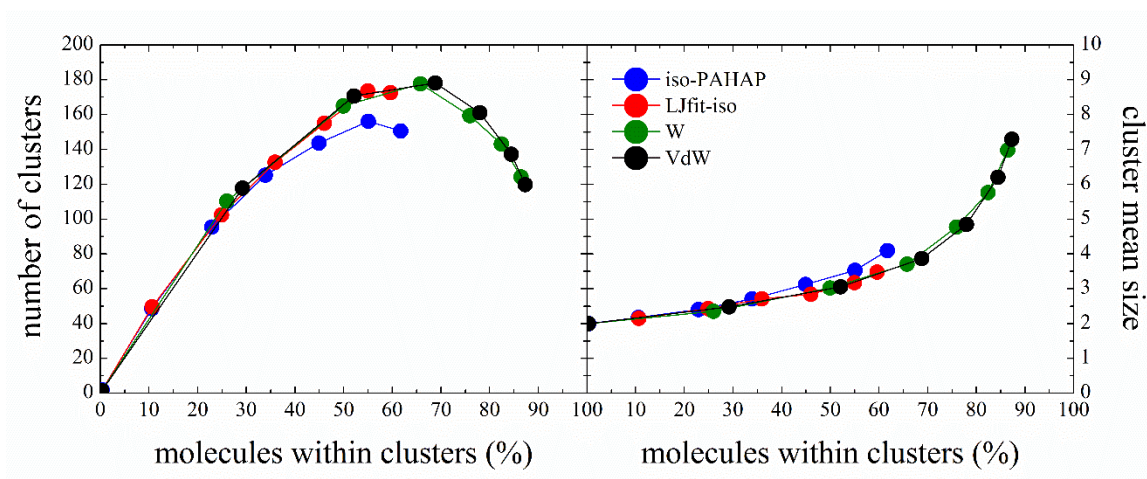


Figure 7.5 Number (left side) and the mean size (right side) of clusters formed as a function of percentage of molecules in clusters using iso-PAHAP potential, LJfit-iso potential, W potential and VdW potential at 500K.

The mean cluster size is not able to capture the detailed evolution of cluster sizes. The cluster size distributions (CSDs), defined as the percentage of clusters with a specific size among total clusters in the system, for the four potential functions and for two different MD times are reported in Fig. 7.6.

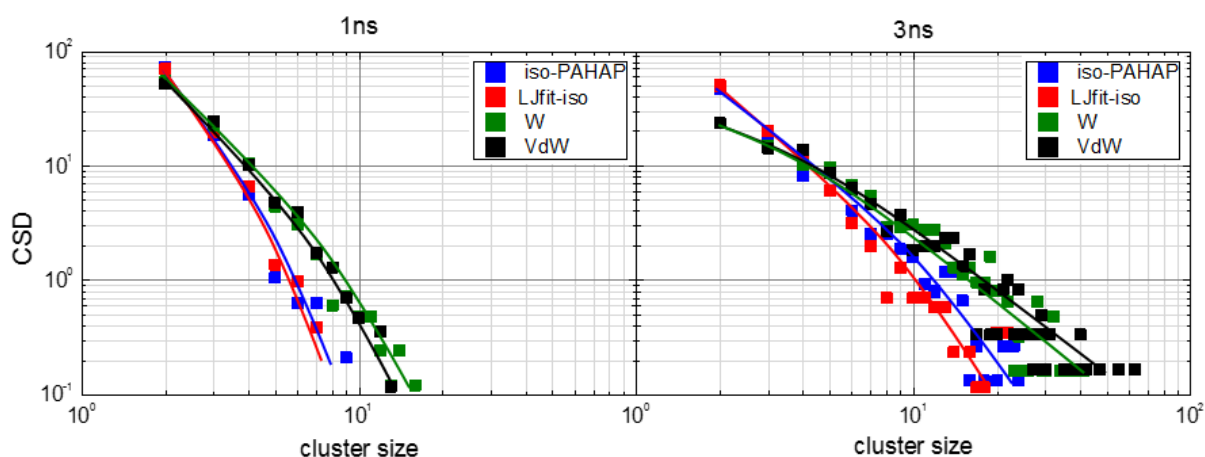


Figure 7.6 CSDs obtained in systems using iso-PAHAP potential, LJfit-iso potential, W potential and VdW potential, at 1 ns (left side) and 3 ns (right side) of MD time at 500 K. Solid guidelines are also reported in the figure.

With all potential functions, CSDs evolve towards the formation of clusters of increasing sizes reaching at 3 ns up to 40 and 60 molecules per cluster in the W and VdW systems, respectively.

This evolution suggests that a more effective coagulation process is taking place, as mentioned before, although a large part of the clusters is mainly constituted by 2-4 molecules. On the contrary, in the iso-PAHAP and LJfit-iso systems, where the number of clusters increases with time (see also Fig. 7.4), CSDs confirm this behaviour showing values significantly smaller compared to strongest potential systems, suggesting that cluster formation rate is always faster than cluster coagulation. It is worth to remind that the number of molecules per cluster indicates the molecular weight and thus the global size of the cluster. However, the size of the cluster is not correlated with the number of stacked molecules within the single cluster. In order to obtain information on the number of stacked molecules within the cluster a further analysis is mandatory.

In fact, additional analyses have been carried out to have a quantitative description of cluster internal structure and shape. Cluster internal structure has been analysed by calculating the distances between centers of mass of molecules in the same clusters. Figure 7.7 reports the internal distance distribution, IDD, of the clusters formed after 3 ns for all the interaction potentials, considering and neglecting the electrostatic interactions.

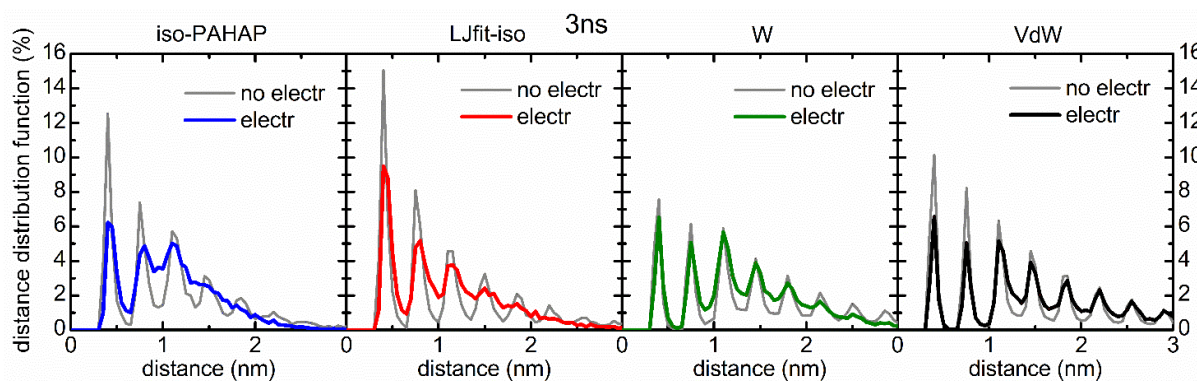


Figure 7.7 IDDs using iso-PAHAP potential, LJfit-iso potential, W potential and VdW potential at 3ns of MD time and at 500K. Coloured and grey lines refer to the case of neglecting and considering the electrostatic term, respectively.

When the electrostatic interactions are neglected (grey lines in Fig. 7.7), the presence of recurring peaks in the IDD is evident in the investigated systems. The distance between adjacent peaks is 0.35 nm, i.e., the distance where the minimum of the interaction potential well is located. The recurring of this distance suggests that molecules within the clusters are quite

ordered. Peaks recur in the IDD with an intensity that decreases with distance (0.35 nm is the most common distance found between two molecules, than 0.70 nm and so on). This suggests that a stacked arrangement of the molecules is prevalent in the cluster structure. Comparing the intensity of the major peaks in different systems, the iso-PAHAP and LJfit-iso show a higher intensity that considerably decreases for the following peaks. This is correlated to the lower size of the clusters in this systems comparing to W and VdW potential systems. Looking at the internal distance distribution for each potential when the electrostatic term is considered (solid lines), broad IDD's can be seen and the peak recurrence, although still visible, is less obvious. In particular, for the iso-PAHAP system, it is still possible to clearly see the main peak due to interaction potential at 0.35 nm, while, even if peaks at 0.7 nm and 1.05 nm can be distinguished, they are less evident than for the other potentials. The decrease of the relative intensity of the two peaks at larger distances suggests that stack of 3-4 molecules well-ordered within the cluster are significantly less common, turning into a more disordered structure. The cluster structure is characterized by the concurrent presence of well-organized regions (clearly identified distances among molecules) and less-organized regions (broad distribution of the IDD). It is possible to see how the number of stacked molecules per cluster does not exceed 4-5 in the iso-PAHAP and LJfit-iso potential and goes up to 8-9 for the W and VdW potential. These values are in line with those found experimentally (Mohan and Manoj, 2012) (Mohan and Manoj, 2017). Finally, it is worth to underline that the electrostatic interactions play a determinant role in order to create disordered zone within the cluster structure.

In order to analyse the morphology of the clusters, the structural parameter P is reported for the clusters formed in all the examined conditions after 3 ns in Fig. 7.8. In the same figure the parameter P calculated for clusters perfectly stacked and hence arranged in a cylindrical shape (solid) and disordered (dashed) clusters are reported to help in discerning the shape of the analysed clusters. The perfectly stacked clusters can be viewed as the most ordered structure possible to achieve; as expected, the parameter P tends to 1 for larger sizes of the clusters, i.e., as H/D increases and the cylindrical approximation is approached. Dashed line represents the maximum value of structural parameter P calculated for all the clusters randomly generated for each cluster size, as described in section 6.2. For a small cluster size (up to 10 molecules) the arrangement can vary in a big range of possible shapes, and P assumes values as large as 0.8. As the size increases, the arrangements approach spherical shapes, and the value of P approaches zero.

Values of P mainly located around the continuous line suggest the main presence of clusters with a cylindrical shape, as for the W and VdW potentials. Differently for iso-PAHAP and for LJfit-iso, both cylindrical and spherical clusters can be found.

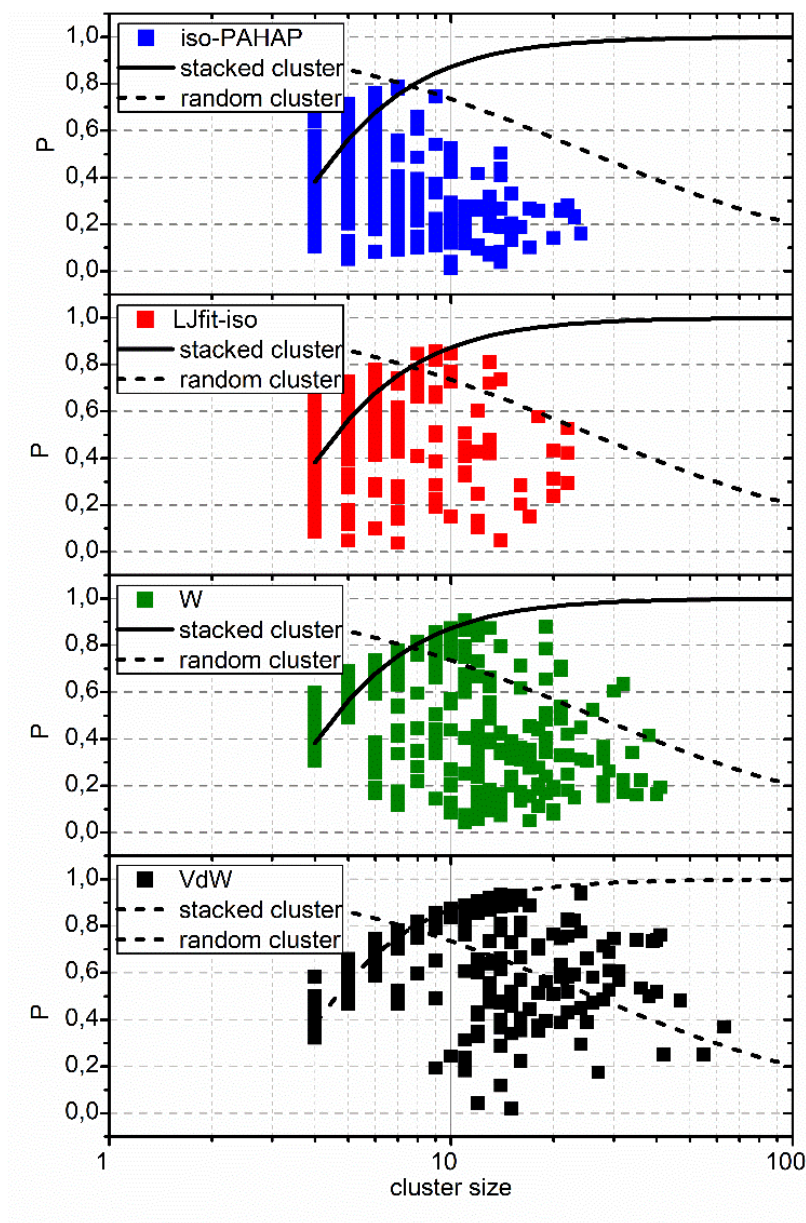


Figure 7.8. Structural parameter P of coronene clusters formed in the system using iso-PAHAP potential, LJfit-iso potential, W potential and VdW potential, at 3ns of MD time at 500K. Solid line represents parameter P for ordered stacked clusters; dashed represents the maximum value of parameter P for randomly generated clusters.

Generally, as the size increases, the presence of cluster far from the continuous line, i.e., ordered configuration, strongly increases. As cluster size increases exceeding 20 molecules, P generally decreases for all the investigated potentials. In the iso-PAHAP and LJfit-iso systems, clusters constituted by 10-20 molecules already show a more disordered structure (lower values of P - below the dashed line of randomly generated clusters). This suggests that their arrangement rapidly approaches a spherical shape. For the W and VdW systems, where large amount of small cylindrical clusters are found, clusters with values of P above the dashed line can be found and have been linked with the presence of elongated structure. These latter are probably a result of coagulation of smaller spherical and/or cylindrical clusters not completely merged.

Simulated images of some representative clusters have been obtained using RasMol software (Sayle and Milner-White, 1995). Figure 7.9 reports images of typical clusters formed using the four potentials considered at 3 ns of MD time.












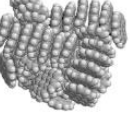




iso-PAHAP	Size 7 P=0.788 	Size 7 P=0.257 	Size 14 P=0.437 	Size 23 P=0.233 
LJfit-iso	Size 9 P=0.819 	Size 9 P=0.225 	Size 13 P=0.811 	Size 22 P=0.525 
W	Size 12 P=0.879 	Size 12 P=0.172 	Size 32 P=0.634 	Size 41 P=0.192 
VdW	Size 14 P=0.883 	Size 14 P=0.118 	Size 30 P=0.747 	Size 63 P=0.368 

Figure 7.9. Images of clusters with different sizes and structural parameters formed using the four investigated potentials at 3 ns of MD time.

Images show that the structural parameter P gives a good description of the cluster shape. In fact, the images confirm that clusters with a P values around 0.8 have approximately a cylindrical shape whereas the cluster shape tends to a sphere as the parameter decreases. The images confirm also the results obtained from the IDD. In the LJfit-iso, W and VDW cases, the recurrence of peaks in the IDD is confirmed by the presence of long stacks up to 10-12 stacked molecules; conversely in the iso-PAHAP case clusters contain stacks of maximum 3-4 molecules. It is worth to evidence that cluster images are here used to confirm the reliability of the P parameter. The use of statistical approach in the analysis of the morphology represents a novelty and a key step in the evaluation of the potentials and their capability to reproduce realistic cluster configurations.

In conclusion, the use of stronger potentials, .i.e., a more intense potential well, as in W and VdW cases, turns not only in a larger percentage of clustered molecules, but also in a more ordered structure, characterized by even more than 10 stacked molecules. The presence of slight differences in the repulsive branch of the intermolecular potential seems having small effect on cluster formation and on the internal order and shape of formed clusters.

When less intense potential interactions are considered, as in the iso-PAHAP and LJfit-iso, a lower number of clusters is formed and these clusters assume a less ordered structure and a shape that more approaches the spherical one. In these cases, the role of the repulsive branch seems to be more evident looking to both the IDD and cluster shape, but it does not affect the clusterization propensity.

For all the investigated potentials, the electrostatic interactions do not affect the total clustering process but changes, even if not considerably, the internal structure and the shape of the formed clusters.

The use in Chapter 6 of a LJ potential parametrization (LJfit-iso) without considering the electrostatic interactions is surely translated in less accurate results. However, the approximation introduced, did not affect remarkably the cluster formation, and it allowed to significantly speed up the simulations that would require many days when the electrostatic interactions are considered.

8. Collision efficiency

Although the possibility of gas-phase PAH stacking in the nucleation process has been largely discussed in the literature and it is regarded as an important process in soot formation (see section 3.2 and Chapter 5), uncertainties remain on the PAHs involved in the process. Pyrene ($C_{16}H_{10}$) stacking, also referred as dimerization, is widely used as the first nucleation step in many soot models (Appel, Bockhorn and Frenklach, 2000) (Richter et al., 2005) (D'Anna and Kent, 2008) (D'Anna, 2008), although MD simulations and/or ab initio calculations indicate that the percentage of clustered molecules at flame temperature is negligible for small PAHs molecules (Chung and Violi, 2011) (Totton, Misquitta and Kraft, 2012). Coronene is also often used as stacking PAH to treat nucleation process in soot models.

As reported in Chapter 5, the inception problem is still mainly modelled by using lumped reactions and a semi-empirical collision efficiency. More detailed treatment of the inception problem has become possible due to more sophisticated approaches, especially MD methods.

In this chapter, the collision efficiency of pyrene and coronene were determined from MD results, in order to relate the MD findings with soot formation models. The homo-molecular pyrene and coronene cluster formation were analysed using a MD software (GROMACS) (Hess et al., 2008). The collision efficiency were calculated in a range of temperature (500 K - 1500 K) and these values were compared with the values used in the soot kinetic model presented by D'Anna and Kent (D'Anna and Kent, 2008).

8.1 Methodology

8.1.1 MD simulations

MD simulations of pyrene and coronene clusterization were performed as described in section 6.1.2. The OPLS-AA (Optimized Potential for Liquid Simulations-All Atom) force field parameters for bonds, angles and dihedrals were used to model the intramolecular interactions (Kaminski et al., 2001), and the iso-PAHAP potential developed by Kraft and co-workers (Totton, Misquitta and Kraft, 2012) were used to model the intermolecular interactions between

molecules. This potential are described in section 6.2 (Table 6.3). Five trajectories of 1 ns for each temperature were run and all the data were averaged over these runs. Clusters were identified as described in section 6.1.4, using a cut-off distance of 1.2 nm and a critical period of time 16 ps. The count of the clusters allowed to track the total clustering vs time and to evaluate the collision efficiency for the given system.

8.1.2 Evaluation of the collision efficiency

As reported in Chapter 5 (see 5.3), the nucleation rate in a homomolecular system can be expressed as:

$$r_{\text{nuc}} = \frac{dN_{\text{dimer}}}{dt} = \gamma K N_{\text{PAH}}^2 = \gamma \pi d_{\text{PAH}}^2 \sqrt{\frac{4\pi k_B T}{m_{\text{PAH}}}} N_{\text{PAH}}^2 \quad (8.1)$$

where N_{dimer} is the dimer number concentration, γ is the collision efficiency, K is the collision frequency, d_{PAH} is the diameter of the PAH molecule, m_{PAH} is the mass of the PAH molecule, N_{PAH} is the PAH number concentration, k_B is the Boltzmann constant and T is the temperature. This quantity is termed the collision efficiency and is defined as the ratio of successful collisions (i.e. collisions which form clusters) to the total number of collisions.

Assuming that N_{PAH} is almost constant during all the simulation and so the number of particle formed during simulation is very low, integrating Eq. (8.1):

$$N_{\text{dimer}}(t) = \gamma \pi d_{\text{PAH}}^2 \sqrt{\frac{4\pi k_B T}{m_{\text{PAH}}}} N_{\text{PAH}}^2 (t - t_0) \quad (8.2)$$

where $(t-t_0)$ is time interval in which the collisions are considered.

In order to relate the MD findings with soot and nanoparticle formation models, we determined the collision efficiency γ of pyrene and coronene from Eq. (8.3).

$$\gamma = \sqrt{\frac{m_{\text{PAH}}}{4\pi k_B T} \frac{N_{\text{cluster}}}{\pi d_{\text{PAH}}^2 N_{\text{PAH}}^2 t}} \quad (8.3)$$

N_{cluster} is the number of stable cluster formed. This assumption is reasonable when every effective collision generates a new cluster in the system, then if the cluster is a dimer.

8.2 Results and discussions

The percentage of clustered molecules and the number of clusters formed as a function of MD time at temperatures of 500 K, 750 K, 1000 K and 1500 K, is reported in Fig. 7.1 (pyrene) and in Fig. 7.2 (coronene).

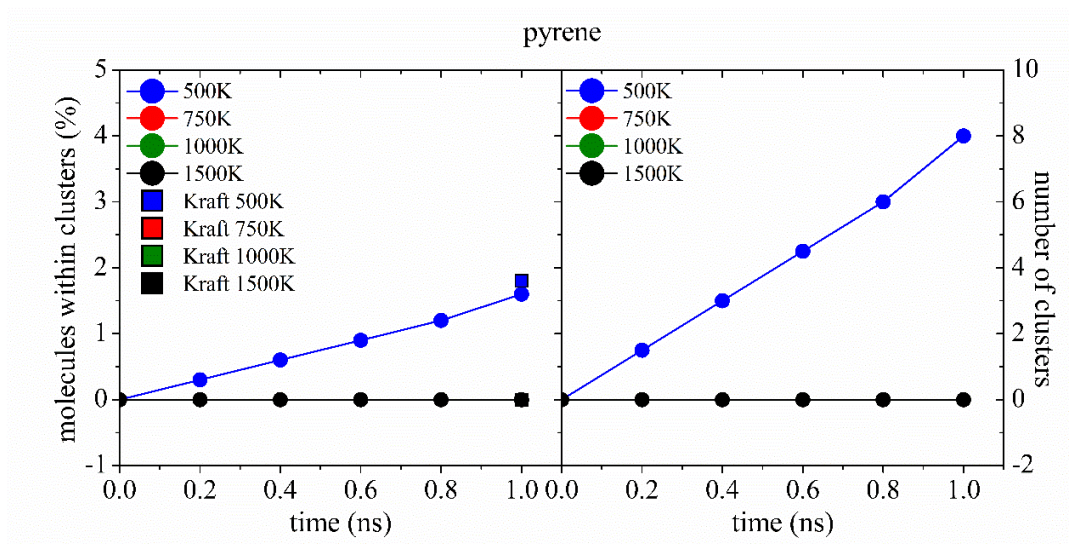


Figure 8.1 Percentage of clustered molecules and number of clusters formed in pyrene systems vs MD time at 500 K, 750 K, 1000 K and 1500 K. Squares refer to the result reported by Kraft and co-workers (Totton, Misquitta and Kraft, 2012) at the same simulation conditions.

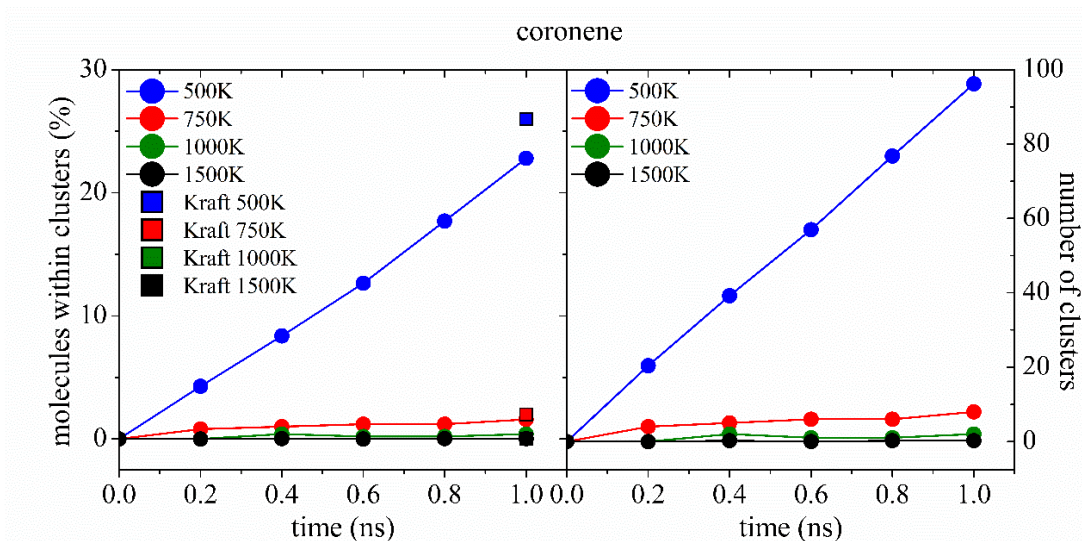


Figure 8.2 Percentage of clustered molecules and number of clusters formed in coronene systems vs MD time at 500 K, 750 K, 1000 K and 1500 K. Squares refer to the result reported by Kraft and co-workers (Totton, Misquitta and Kraft, 2012) at the same simulation conditions.

In the pyrene system, the percentage of clustered molecules is very low also at 500 K (1.6% after 1 ns of simulation) (Fig. 7.1). In the coronene case (Fig. 7.2), this percentage increases with time and it grows approximately linearly up to 23% after 1 ns at 500 K. As temperature increases, the percentage of clustered molecules decreases and it becomes very small at temperature higher than 750 K. Similar considerations can be done on the number of formed clusters.

The results obtained in both case are in good agreement with the results obtained by Kraft and co-workers (Totton, Misquitta and Kraft, 2011) in the same conditions (1000 starting molecules and 5 trajectories for each system) and using the same interaction potential between molecules (squares in Fig 7.1 and 7.2). They conclude that in low-temperature regions of the flame (500 K– 1000 K), physical nucleation may still be a competitive route for particle inception and growth for molecules larger than pyrene and only circumcoronene was found to dimerise at 1500 K (Totton, Misquitta and Kraft, 2011).

To understand if small PAHs (as pyrene and coronene) dimerization is not a competitive route in soot formation at flame temperature, the MD results were related with soot formation models evaluating the collision efficiency of these molecules.

The collision efficiency γ were calculated using Eq. (8.3) at every temperature, assuming that the number of effective collision is equal to the number of clusters formed (n_{clust}). This assumption is reasonable when every effective collision generates a new dimer in the system. This is true for all the systems where the mean and maximum sizes are equal to 2, hence for pyrene systems and when $T > 750$ K for the coronene systems (Table 8.1 and 8.2). The results are displayed in Table 8.1(pyrene) and Table 8.2 (coronene).

Table 8.1 Mean and maximum sizes, number of effective collision and collision efficiencies of pyrene after 1 ns, at 500 K, 750 K, 1000 K and 1500 K.

T	500 K	750 K	1000 K	1500 K
mean cluster size	2	0	0	0
maximum cluster size	2	0	0	0
n_{clust}	8	0	0	0
γ	$2.1 \cdot 10^{-3}$	0	0	0

Table 8.2 Mean and maximum sizes, number of effective collision and collision efficiencies of coronene after 1 ns, at 500 K, 750 K, 1000 K and 1500 K.

T	500 K	750 K	1000 K	1500 K
mean cluster size	2.37	2	2	2
maximum cluster size	7	2	2	2
n_{clust}	96.2	8	2	0.2
γ	$3.5 \cdot 10^{-2}$	$2.5 \cdot 10^{-3}$	$5 \cdot 10^{-4}$	$4 \cdot 10^{-5}$

The collision efficiency is influenced by temperature and molecular mass. Pyrene does not dimerize at high temperature conditions, while the coronene dimerization is more consistent for various temperature conditions. At flame temperature (1500 K), the calculated coronene collision efficiency is of the order of 10^{-5} . This value is lower than the value used by D'Anna and Kent to model soot formation (D'Anna and Kent, 2008). They use a collision efficiency of $2 \cdot 10^{-4}$ at 1500 K for two colliding aromatic compounds with 1 nm of diameter (Fig. 8.3). Collision efficiencies calculated with MD derive from a detailed treatment of the inception problem; for this reason, in a first analysis, these results suggest that the current soot formation models use collision efficiency for small PAH dimerization that overestimate their role in soot formation process ($\gamma_{\text{pyrene}}=1.5 \cdot 10^{-5}$ and $\gamma_{\text{coronene}}=2 \cdot 10^{-4}$) (Fig. 8.3).

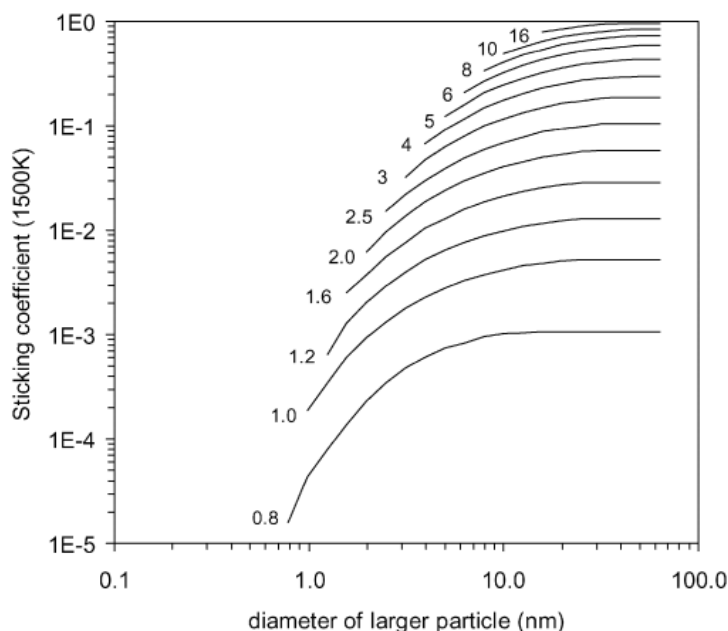


Figure 8.3 Sticking efficiency for sectional particle diameters used by D'Anna and Kent to model soot formation (D'Anna and Kent, 2008). Lines refer to smaller particle diameter (nm).

In a second analysis, looking Table 8.2, the collision efficiency of coronene at 1500 K is calculated using a mean value of the number of formed clusters ($n_{\text{clust}}=0.2$) that is probably obtained with a small statistical sample. In fact, the clustering data was averaged over only five trajectories of 1 ns for each coronene system. All similar papers using MD on PAHs clustering presented in literature use five trajectories for each case (Chung and Violi, 2011) (Totton, Misquitta and Kraft, 2011). The collision efficiency calculated might be the result of an inaccurate statistical analysis. The mean value of clustered formed at 1500 K is reported as example. As it is possible to observe from the results of the different runs reported in Table 8.3, the statistical sample seems not very representative and the statistical analysis seems to suffer for the limited dimension of the sample.

Table 8.3 Number of clusters formed in the coronene system after 1 ns at 1500 K for all the five trajectories.

Trajectory	1	2	3	4	5
Number of cluster	0	0	0	0	1
Mean value	0.2				

In order to have a more detailed and accurate statistical analysis, the clustering data should surely be averaged over a more extended number of trajectories or it should be evaluated starting from a larger number of molecules until having a mean value bigger than 1. The latter case is reported in the next section.

8.2.1 Increase in the number of starting molecules

Five simulations at 1500 K for the coronene system were performed with a number of starting molecules N equal to 10000. The results and the obtained collision efficiency are reported in Table 8.4. Increasing the number of starting molecules, the statistical sample become more representative and the obtained collision efficiency is two times the one obtained previously ($\gamma=8 \cdot 10^{-5}$ respect to $\gamma=4 \cdot 10^{-5}$) and more similar to the collision efficiency value used in current soot models ($\gamma=2 \cdot 10^{-4}$) (Fig. 8.3.).

Although the collision efficiency is still lower than the one used in soot models, the role of coronene dimerization in soot formation cannot be excluded. A more accurate analysis can be still done averaging the results over an extended number of trajectories. However, the computational cost of each trajectory of the system composed by 10000 starting molecules is about 72 h on a 64-processor machine. The high computational cost limits the number of simulations and the feasibility of a much more accurate analysis.

This MD methodology used to obtain more accurate collision efficiencies can be extended to other PAH molecules in order to investigate their role in soot formation.

Table 8.4 Number of clusters and collision efficiencies of coronene after 1 ns at 1500 K for the five trajectories obtained starting from 1000 and 10000 molecules.

Coronene						
N = 1000	Trajectory	1	2	3	4	5
	Number of cluster	0	0	0	0	1
	Mean value	0.2				
	γ	$4 \cdot 10^{-5}$				
N = 10000	Trajectory	1	2	3	4	5
	Number of cluster	2	3	4	4	5
	Mean value	3.6				
	γ	$8 \cdot 10^{-5}$				

9. Mechanical properties of cross-linked PAHs

In Chapter 4 some morphological aspects of soot particles have been reported. Soot particles, observed via high resolution transmission electron microscopy (HR-TEM), have been found to be constituted by aromatic layers generally organized in a turbostratic structure (Palotas et al., 1996) (Chen et al., 2005) (Bhowmick and Biswas, 2011). These layers have been interpreted as the stacking of large polycyclic aromatic hydrocarbons (PAHs). Experimental findings also show that soot extracted in the post-flame region can contain significant amounts of aliphatic components relative to aromatics (Cain et al., 2010) (Cain et al., 2011); it suggests that aliphatic chains or bridge formation between aromatic parts can also play an important role in soot formation.

The aim of this chapter is to find a relation between a possible structure of nanoparticles formed in a combustion environment and its mechanical properties. In fact, mechanical properties of a material are strictly related to its internal structure. Representative boxes of PAHs with varying degree of cross-linking were built using reactive force-field Molecular Dynamics (MD) simulations. MD simulations of uniaxial tensile tests on these PAH boxes were made. Hardness of each sample was calculated and the results compared with nanoindentation experiments of soot particles. The results clearly show that the soot structure must present cross-links between its constituent PAH molecules to have a comparable value of the hardness found experimentally. The results give also information on the possible degree of crosslinking within soot particles.

9.1 Methodology

MD method was employed to simulate the uniaxial tensile deformation of PAH structures. A cross-linking procedure was developed to build the starting geometry. The effects of the degree of crosslinking in the structure on mechanical properties was investigated. The degree of cross-linking (CL) were defined as:

$$CL = \frac{\text{number of cross - links}}{\text{number of starting monomers}} \quad (9.1)$$

The stress–strain curves were plotted and the hardness of the different samples was calculated. The simulation results were compared with existing experimental data.

To achieve the goal the following procedure was adopted:

- 1) Construction of PAH boxes with different degree of cross-linking
- 2) Uniaxial tensile deformation tests and evaluation of yield stress
- 3) Comparison with experimental data

Every part will be described in detail in the next sections. All the MD simulations were carried out using the LAMMPS software (Plimpton, 1995).

9.1.1 Construction of the starting geometry

Pyrene, coronene and ovalene were chosen as starting monomers. Monomers were randomly located in a cubic simulation box with periodic boundary condition using the PACKMOL software (Martínez et al., 2009). The number of molecules were chosen to have a starting box of 43 Å with a density of 1.5 g/cm³, which is the typical value for nascent soot particles (Zhao, Uchikawa and Wang, 2007). The interactions within molecules, were modelled using an updated version of the adaptive intermolecular reactive empirical bond order (AIREBO) potential (Stuart, Tutein and Harrison, 2000), known as AIREBO-M (O'Connor, Andzelm and Robbins, 2015). AIREBO-M uses the same functional form as the hydrocarbon second-generation REBO potential (Brenner et al., 2002), with an additional Morse term to represent the Van der Waals interactions. The Morse potential replaces the Lennard-Jones potential used in the original AIREBO, which has been shown to yield unphysical results for carbon systems subjected to high pressures (O'Connor, Andzelm and Robbins, 2015). The Morse potentials are parameterized by high-quality quantum chemistry calculations and do not diverge as quickly as particle density increases. This allows AIREBO-M to retain accuracy to much higher material densities than AIREBO.

The cross-linking process is complex and requires a great computational effort. It involves hydrogen abstraction, ring open and new bonds formation. However, investigation of this process is beyond the scope of this study, and some assumptions were made to develop a practical and fast cross-linking procedure, which can be used to build a cross-linking structure near to reality. The cross-linking procedure was realized as follows:

- 1) The initial uncross-linked structure was firstly minimize and then equilibrated for 200 ps of simulation in the isothermal and isochoric ensemble (NVT) at 300 K. The corresponding integration time step was 0.5 fs. The constant temperature was controlled by the Berendsen thermostat, with a time constant of 0.1 ps. Due to the periodic boundary conditions, covalent bonds can form not only between the monomers inside the simulation cell, but also between monomers across the periodic boundaries. Therefore, this step is necessary to ensure a good distribution of molecules also in the boundary region (Fig 9.1). It was verified that, avoiding this step, the cross-link density in the boundary region is lower respect to the density in the central region, so that, during the tensile test, the structure fail near the boundaries and the tensile test results less accurate.

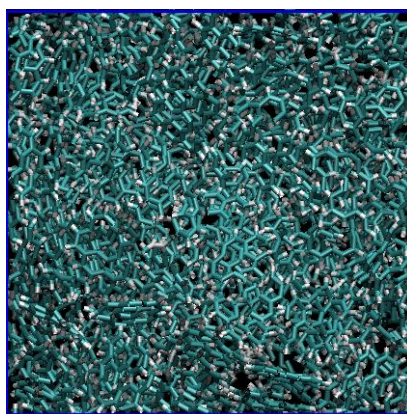


Figure 9.1 The simulation box of uncross-linked monomers after the first equilibration step.

- 2) The cross-link process starts with hydrogen abstraction to a consequent bond creation between molecules. The MD simulation of the hydrogen abstraction would require an excessive computational time. Then, to speed up the process, the reactive sites were created in the simulation boxes by directly removing hydrogen atoms from every second carbon atom around the rim of the monomers, thus obtaining the radical species reported in Fig. 9.2.
- 3) A MD simulation (NVT, 1000 K, 100 ps) was carried out on the new structure, in order to create chemical bonds between pair of reactive sites. The use of a reactive potential allows for chemical bond rupture and bond formation to occur.

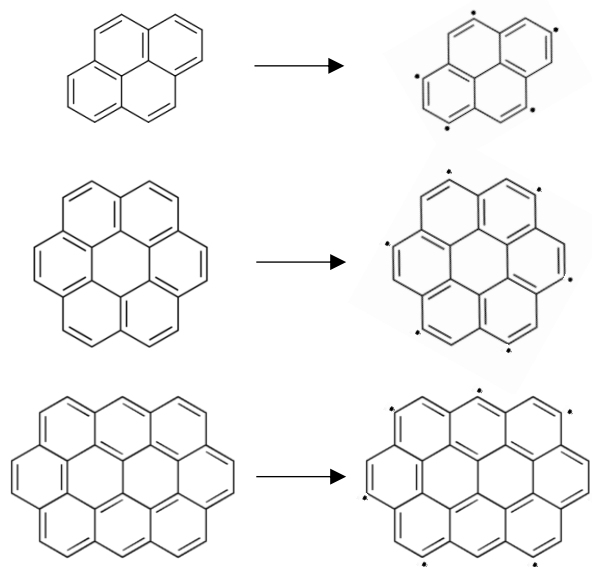


Figure 9.2 The radical species obtained removing hydrogen atoms from every second carbon atom around the rim of the monomers.

The time step of 0.25 fs was adopted for the integration of atom motion equations and the constant temperature was controlled by the Berendsen thermostat, with a time constant of 0.1 ps. These simulation parameters ensure a stable simulation, although the bond formations would lead the system through very high temperature.

The types of crosslinks considered were the most preliminary types of crosslinks where a single aliphatic linkage joined two PAH molecules. This provided geometries which were rotated with respect to each other and allowed for three dimensional cross-linking (Fig. 9.3).

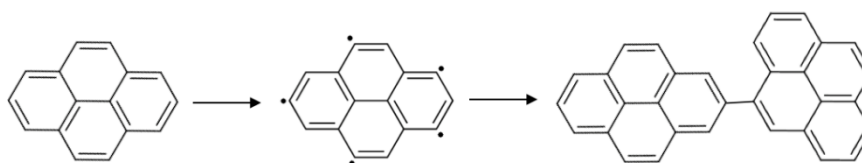


Figure 9.3 Crosslinking strategy to produce aliphatically linked PAHs.

The reactive force-field simulations were halted at different times to provide varying degrees of crosslinking.

- 4) The un-reacted reactive sites were saturated with hydrogen atoms. Finally, an energy minimization was conducted to the system.

9.1.2 Uniaxial tensile test

The systems were equilibrated with dynamic simulation in the isothermal and isobaric ensemble (NPT, 300 K, 1 atm, 100 ps), to make sure the temperature, pressure, and other properties are steady before deformation. The time step was of 1 fs and a Nose-Hoover barostat and thermostat were applied to control the system pressure and temperature during the equilibration step with a time constant of 0.1 ps. Although the starting box expand until it reaches the atmospheric pressure at the desired temperature, the density remains almost the same at the end of the equilibration step. MD simulations at 300 K were used to characterize the mechanical response of the cross-linked PAHs. The systems were deformed in x-direction under uniaxial tensile strain applied at constant strain rate of 10^{10} s^{-1} while the y and z boundaries were controlled using the NPT equations of motion to atmospheric pressure. It was verified that uniaxial tensile tests deforming in y and z directions give almost the same results due to the isotropic behaviour of the process. The stress and strain values were calculated during the simulation. The yield point is defined as the stress at which a material begins to deform plastically. To identify the precise location of the yield point, a numerical unloading procedure was performed at different locations along the loading path. The unloading was performed by incrementally decreasing the deformation gradient applied down to the initial un-deformed configuration. The failure was assigned to the last point that exhibits reversible behaviour on the stress-strain curve and hence does not lead to residual stress at zero strain (Abdolhosseini Qomi et al., 2017).

The tensile property of the systems changes using different strain rate. In particular, the same stress is obtained at higher strain increasing the deformation rate, because the structure is less able to relax in response to faster deformation. Meanwhile, it was verified that the yield stress evaluation is not affected by changing strain rate.

A schematic of the adopted procedure is reported in Fig. 9.4.

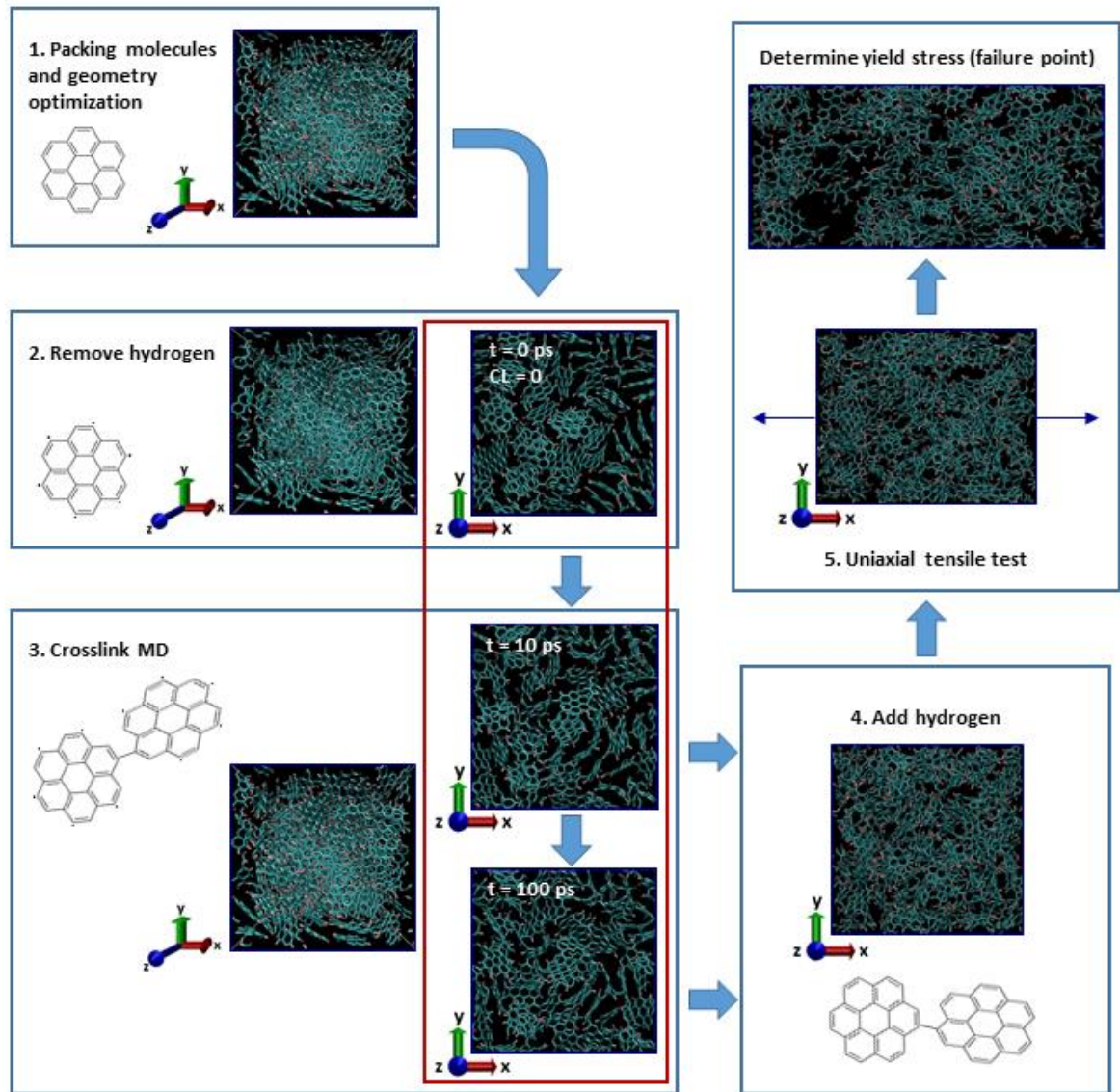


Figure 9.4 The steps involved in the crosslinking simulations: 1. the aromatic molecules are packed into the simulation box; 2. hydrogen atoms are removed from every second carbon atom around the rim of the molecule; 3. a reactive forcefield simulation is run and halted at different times to provide varying degrees of crosslinking; 4. hydrogens are then added back to the sites that have not formed crosslinks; 5. the structure is uniaxially strained until failure.

9.1.3 Comparison with experimental values

Due to impossibility of performing a uniaxial tensile test on a soot particle, the results were compared with nanoindentation experiments on soot particles obtained using an atomic force microscope (AFM). Engine soot have been recognized to contribute to the wear of engine components, and, for this reason, some nanoindentation experiments have been carried out in

order to relate the hardness of soot particles to their morphological aspect, such as particle size, crystallography and shell thickness (Bhowmick and Biswas, 2011). The hardness values obtained for nanoparticles thermophoretically collected from different thermal zones of an ethylene flame have values ranging from 3 to 5 GPa (Table 9.1). Hardness value obtained from nanoindentation experiments of other carbonaceous materials are also reported in Table 9.1.

The calculation of the hardness from the uniaxial yield stress is possible by utilizing an empirical conversion constant K. In fact, for many classes of materials there is a linear correlation between indentation hardness and yield stress (Eq. 9.2) (Zhang, Li and Zhang, 2011) (Koch and Seidler, 2009).

$$H = K\sigma_f \quad (9.2)$$

To convert the yield stress values in hardness, the constant K in Eq. 9.2 was evaluated assuming that cross-linked PAH structures have an intermediate structure between highly oriented pyrolytic graphite (HOPG) and diamond. The procedure described in the previous section has been adopted on HOPG and diamond sample to calculate their yield stresses, and then, using the hardness value reported in Table 9.1, to calculate the empirical conversion constant K.

Table 9.1 Carbon materials hardness values from nanoindentation experiments.

Material	Hardness (GPa)	Reference
Nanocrystalline graphite	0.1-1.0	(Patterson et al., 2000)
HOPG	2.4	(Richter et al., 2000)
Carbon black	3-4	(Bhowmick, Majumdar and Biswas, 2011)
Ethylene soot	3-5	(Bhowmick and Biswas, 2011) (Bhowmick, Majumdar and Biswas, 2011)
Charcoal	3-5	(Zickler, Schoberl and Paris, 2006)
Diesel soot	6-7	(Bhowmick, Majumdar and Biswas, 2011)
Compressed and polymerized C ₇₀	30	(Patterson et al., 2000)
Glassy carbon	30	(Iwashita and Swain, n.d.)
Diamond	100	(Richter et al., 2000)

9.2 Results and discussions

Pyrene, coronene and ovalene systems with varying degree of cross-linking were built using the procedure described in section 9.1.1. The degree of cross-linking (CL), defined as in Eq. 9.1, is reported in Fig. 9.5 as function of MD time. Initially, there are abundant reactive sites available for the cross-linking reaction, which is translated in a rapid increase of the cross-linking degree in the first picoseconds of simulation. As the reaction goes on, less reactive sites are available for the cross-linking reaction and thus, the curve becomes almost steady reaching a value between 3.5 and 4 in all the system. Considering the large computational consumption and a limited improvement in terms of the cross-linking degree, current simulation time (100 ps) can be considered reasonable. A 5 Å slice of the simulation box before and after the cross-linking procedure is shown in Fig. 9.6 for coronene system. In the last configuration (Fig. 9.6b), it is possible to distinguish not only the cross-link network, but also some groups of molecules arranged in parallel planes. C/H ratio as function of MD time is also reported in Fig. 9.5 and it shows the same behaviour of CL. The C/H values are typical of nascent soot (see also 4.2).

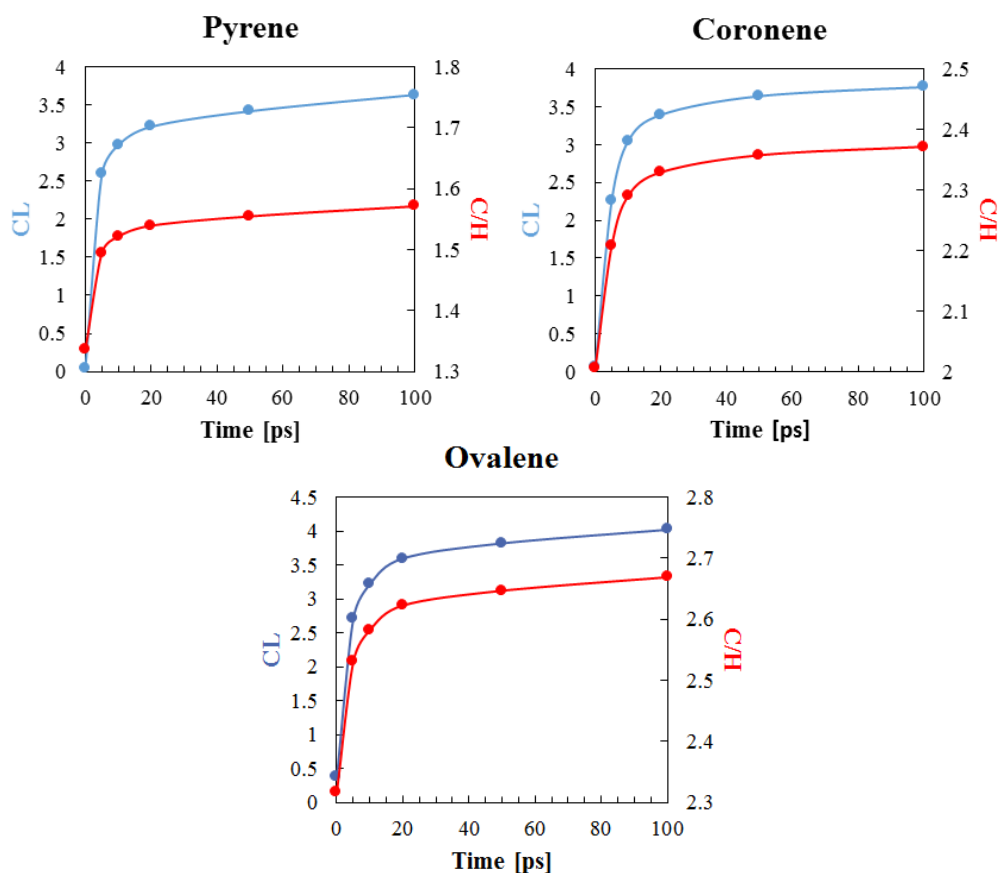


Figure 9.5 Degree of cross-linking (blue lines and left axes) and C/H ratio (red lines and right axes) as function of MD time for pyrene, coronene and ovalene systems.

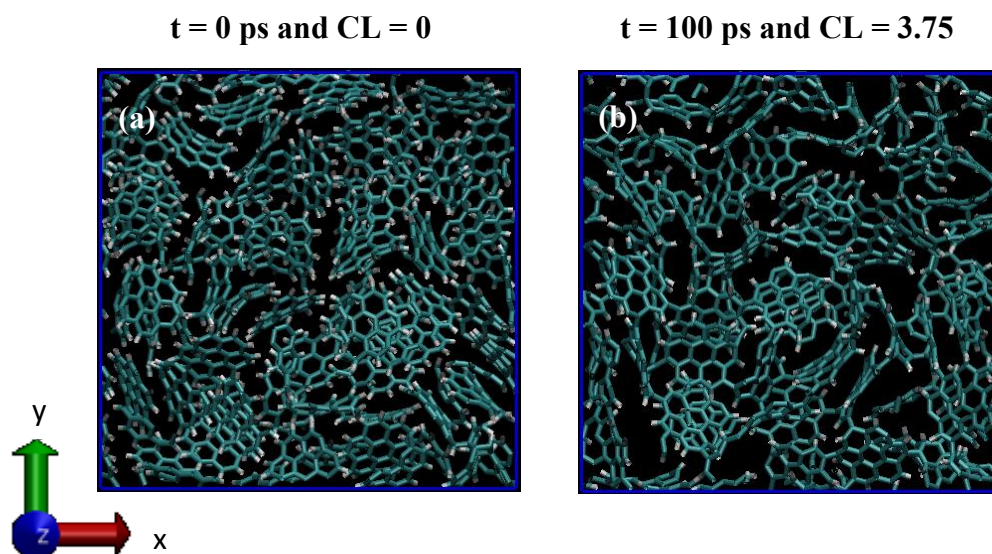


Figure 9.6 A 5 Å slice of the simulation box before (a) and after (b) the cross-linking procedure for coronene system.

Some structures with different degree of cross-linking were selected during the cross-link procedure and MD uniaxial tensile tests were made on these selected structures. Figure 9.7 shows stress versus strain curves for these PAH structures with varying degree of cross-linking at strain rate of $1 \cdot 10^{10} \text{ s}^{-1}$. The simulation results indicate that tensile property increases with the degree of cross-linking. The cross-linking reaction changes some physical interactions to covalent bonds, which strengthens the mechanical properties of the sample. It is interesting to note that the tensile property of the uncross-linked structure (CL=0), i. e. when monomers interact only physically, is very low.

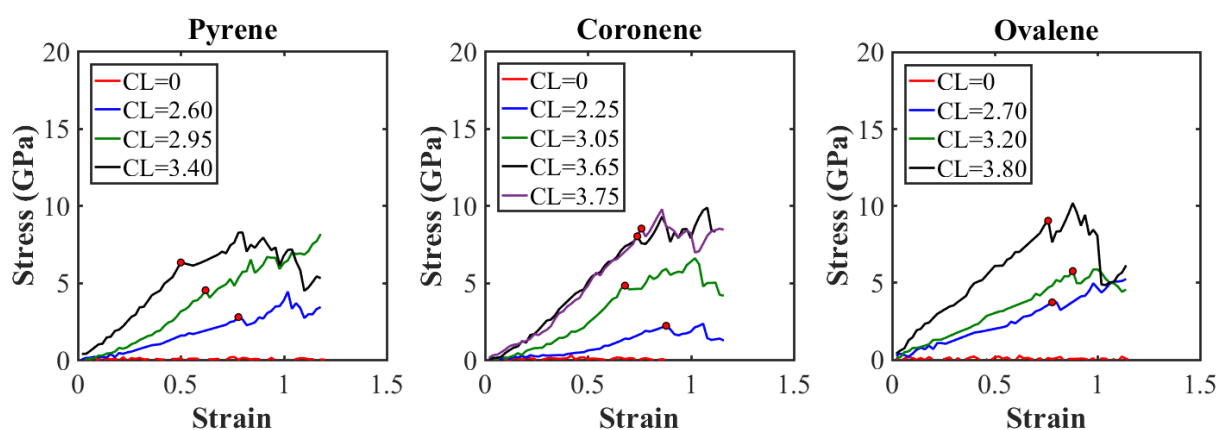


Figure 9.7 Stress–strain curves for pyrene (left), coronene (middle) and ovalene (right) systems with varying degrees of cross-linking (CL). Red circles represent the yield point in each system.

A numerical unloading procedure was performed at different locations along the loading path, to identify the precise location of the yield point. In Fig. 9.8 three loading-unloading paths for the pyrene system with CL=3.40 are reported as example. The unloading paths from point 1 and 2 lead to residual stress at zero strain, indicating that the material deformed plastically during the loading process. The unloading from point 3 goes back to the original configuration with no residual stress. Therefore, point 3 was assigned as yield point in that system.

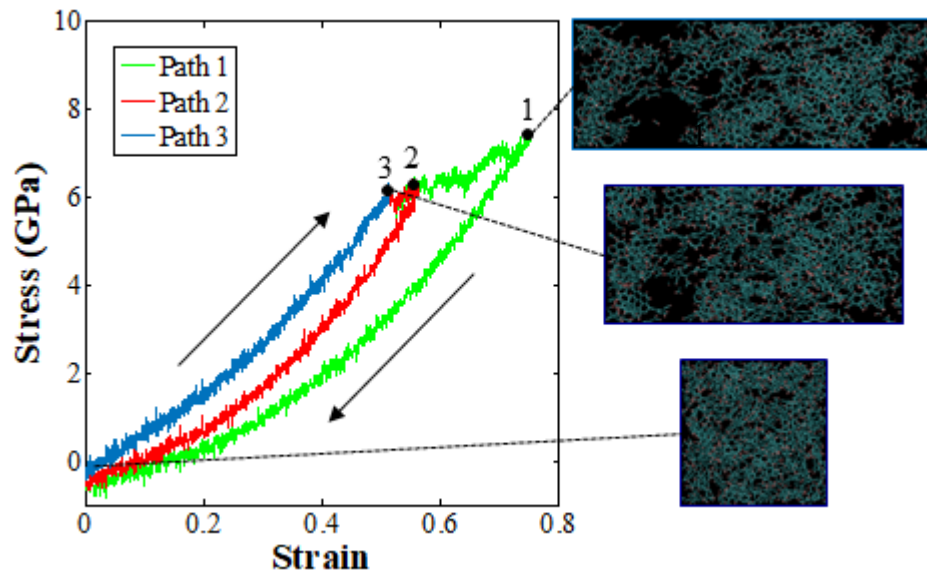


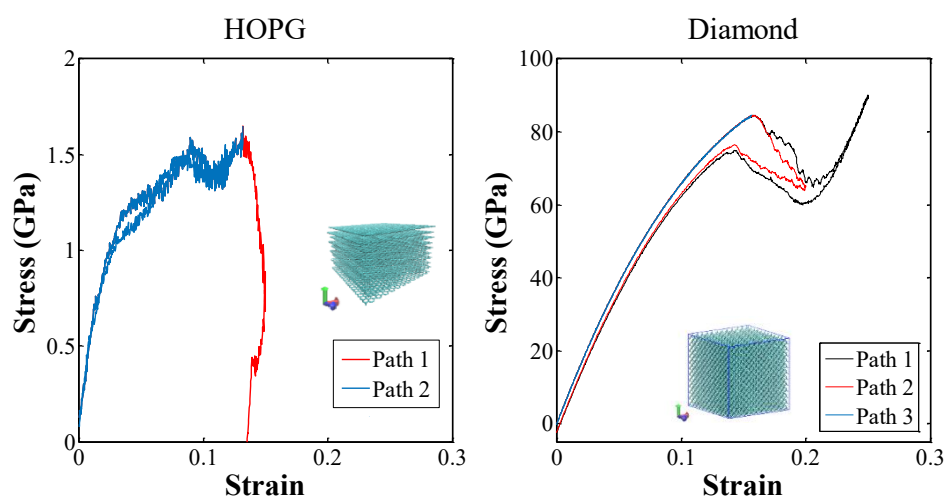
Figure 9.8 Stress-strain loading and unloading curves to determine yield stress for the pyrene system with CL=3.40.

The yield stresses (σ_f) obtained by the load-unload procedure for all the systems investigated are reported in Table 9.2 (red circles in Fig. 9.7).

To convert the yield stress values in hardness, the constant K in Eq. 9.2 was evaluated assuming that cross-linked PAH structures have an intermediate structure between highly oriented pyrolytic graphite (HOPG) and diamond. The yield stress for diamond and HOPG were obtained using the same uniaxial tensile simulation conditions described in section 9.1.2. The tensile direction in the HOPG system is the direction perpendicular to the basal plane, while it is the (100) direction in the diamond system. To identify the precise location of the yield point, a loading-unloading procedure was performed. Results are shown in Fig. 9.9.

Table 9.2 Yield stress and hardness values for the investigated PAHs structures using an empirical conversion constant $K=1.4$.

PAH	CL	σ_f (GPa)	H (GPa)
Pyrene	0.00	0.05	0.07
	2.60	2.75	3.86
	2.95	4.20	5.88
	3.40	6.30	8.82
Coronene	0.00	0.10	0.14
	2.25	2.20	3.08
	3.05	4.90	6.72
	3.65	7.950	11.17
	3.75	8.50	11.90
Ovalene	0.00	0.10	0.14
	2.70	3.70	5.18
	3.20	5.70	7.98
	3.80	9.00	12.60



material	σ_f (GPa)	H (GPa)	K
diamond	83	100	1.2
HOPG	1.5	2.4	1.6

Figure 9.9 Stress–strain curves, yield stress, hardness and empirical conversion constant K for HOPG (left) and diamond (right) systems.

Hardness values were taken from Table 9.1 and the corresponding K values were calculated using Eq. 9.2. Hardness (H) values in Table 9.2 have been calculated using Eq. 9.2 with an empirical conversion constant $K=1.4$, an intermediate value between HOPG and diamond.

Finally, hardness is plotted as a function of the degree of cross-linking in the structure in Fig. 9.10. The hardness grows with the degree of cross-linking in the structure. The cross-linking conversion enhance the mechanical properties of the material tested. There is a weakly dependence on the extension of aromatic molecule used as monomer. For a fixed degree of crosslinking, the pyrene systems assume a lower hardness value respect to coronene and ovalene systems indicating that the physical interactions influence, even if slightly, mechanical properties. However, moving from coronene to ovalene the curves overlap, suggesting an equal contribution of the physical interactions on the hardness value for molecules of sizes greater than or equal to coronene.

The results clearly show that the soot structure must present cross-links between its constituent molecules to have a comparable value of the hardness found experimentally (Table 9.1). The results give also information on the possible degree of crosslinking in soot particles: $CL=2.25$ - 2.75 for ethylene soot and $CL\sim 3$ for diesel soot (Fig. 9.10).

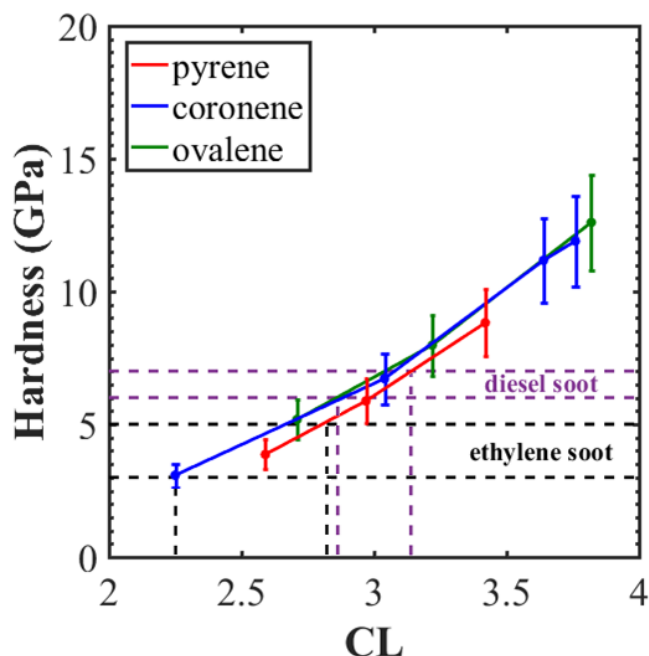


Figure 9.10 Hardness vs degree of cross-linking (CL) in the pyrene (red), coronene (blue) and ovalene (green) systems using $K=1.4$ (with error bars showing $K=1.2$ – 1.6). The hardness values determined for diesel soot and ethylene soot are also shown for comparison (Bhowmick, Majumdar and Biswas, 2011).

10. Summary and conclusions

Nucleation is the least understood process in particle formation mechanism in a combustion environment. Polycyclic aromatic hydrocarbon (PAHs) have been recognized as the precursor molecules because they have been detected, at not-negligible concentrations, in flames and are collected in soot samples as adsorbed material. Although a consensus is found in the literature about the central role of PAHs in the nucleation process, the presence of many different compounds in soot particles gives uncertainties on the exact nature of the gas-phase PAHs involved in the process.

Molecular dynamics (MD) approach allows to describe punctually the physical interaction and evolution of the particles and of their principal constituents, i.e., the PAHs. Monitoring the internal coordinate of atoms in the system over the time, MD allows to predict qualitatively the behaviour of a system at conditions that cannot be accessed experimentally.

The objective of this study was to explore nucleation process and the properties of particles obtained by using MD.

Firstly, the role of different PAHs in the physical nucleation process were investigated using MD in a range of temperatures (500 K-1500 K). Two different types of molecules present in a flame environment were studied: peri-condensed aromatic hydrocarbons (PCAHs), namely pyrene ($C_{16}H_{10}$) and coronene ($C_{24}H_{12}$), and aromatic molecules containing pyrene and coronene connected with a σ -bond, dipyrene ($C_{32}H_{18}$) and dicoronene ($C_{48}H_{22}$), representative of aromatic aliphatic-linked hydrocarbons (AALHs). MD allows to treat the nucleation in a physical way. However, the investigation of AALH evolution permits to treat indirectly also the chemical pathway because every ALLH molecule can be viewed as the result of a chemical reaction between PCAH molecules.

The presence of covalent bonds connecting two aromatic islands improve the inception and growth mechanisms of the clusters in the investigated system. As temperature increases, clusterization becomes less efficient for all the investigated systems and at 1500 K only dicoronene shows a significant clusterization process. At 500 K clusters are formed for all the aromatics, being the σ -bonded molecules more effective than the corresponding PAHs. Moreover, the presence of the σ -bond increases the amount of disorder and the sphericity of the formed particles, making their structure more similar to what found through HR-TEM images.

Therefore, it appears that the chemical structure of precursor PAH molecules influence the cluster formation and control the morphology of the particles, suggesting that AALHs can play an important role in the nucleation process.

In this first part of the thesis, a Lennard-Jones (LJ) parametrization, with parameters calculated by fitting the position and depth of the minima of the iso-PAHAP potential developed by Kraft and co-workers (Totton, Misquitta and Kraft, 2012), was used to describe the intermolecular interactions, while the electrostatic interactions were neglected. This choice is related to the long simulation time performed (6 ns) and to the high computational cost that the calculation of the long-range electrostatic term requires. However, the choice of the intermolecular potential is critical in the MD simulations. Different results are in fact mainly affected by this choice, as it is possible to see in similar works of combustion-generated particle nucleation using MD simulations (Chung and Violi, 2011) (Totton, Misquitta and Kraft, 2012).

For this reason, in the second part of this thesis, four intermolecular potentials used in literature to model interactions between PAHs, which differ for their function forms and parametrizations, were selected in order to analyse the difference in the results obtained in MD simulations of coronene cluster formation at a temperature of 500 K. The internal organization and shape of the clusters were systematically analysed in order to have a better comparison between the potentials and their capability to reproduce realistic configurations.

The results show that the cluster formation is strongly dependent on the magnitude of potential interaction, while appears to be weakly dependent of the kind of the adopted potential functions. The stronger potentials, turns not only in a larger percentage of clustered molecules, but also in a more ordered structure, characterized by even more than 10 stacked molecules. The presence of slight differences in the repulsive branch of the intermolecular potential seems having small effect on cluster formation and on the internal order and shape of clusters formed. When less intense potential interactions are considered, the formed clusters have a less ordered structure and a shape that more approaches the spherical one. In these cases, the role of the repulsive branch seems to be more evident looking both the internal order and cluster shape, but it does not affect the clusterization propensity. For all the investigated potentials, the electrostatic interactions do not affect the total clustering process but changes, even if not considerably, the internal structure and the shape of the formed clusters.

The use in the first part of this work of a LJ potential parametrization without considering the electrostatic interactions is surely translated in less accurate results. However, the

approximation introduced, did not remarkably affect the cluster formation, and it allowed to significantly speed up the simulations that would require many days when the electrostatic interactions are considered.

Finally, the possible presence of covalent bonds between soot aromatic constituents was investigated studying the mechanical properties of cross-linked PAHs using reactive force-field MD simulations. Representative boxes of PAHs with density similar to nascent soot and with varying degree of cross-linking were built. MD simulations of uniaxial tensile tests on these PAH boxes were made. Hardness of each sample was calculated and the results were compared with nanoindentation experiments of soot particles. The results clearly show that the soot structure must present cross-links between its constituent PAH molecules to have a comparable value of the hardness found experimentally. The results give also information on the possible degree of cross-linking in soot particles. Ethylene soot and diesel soot are expected to have cross-linked densities between 2.25–2.75 and ~ 3 , respectively.

In conclusion, the results of this thesis provide insights on combustion-generated particle morphology and on the soot nucleation process, in particular regarding the role of σ -bonded PAHs.

11.References

- Abdolhosseini Qomi, M.J., Ebrahimi, D., Bauchy, M., Pellenq, R. and Ulm, F.J. (2017) 'Methodology for estimation of nanoscale hardness via atomistic simulations', *J. Nanomech. Micromech.*, vol. 7, 4, 04017011.
- Alder, B.J. and Wainwright, T.E. (1957) 'Phase transition for a hard sphere system', *J. Chem. Phys.*, vol. 27, 1208–1209.
- Alfè, M., Apicella, B., Barbella, R., Rouzaud, J.N., Tregrossi, A. and Ciajolo, A. (2009) 'Structure-property relationship in nanostructures of young and mature soot in premixed flames', *Proc. Combust. Inst.*, vol. 32, 697-704.
- Anilkumar, P., Lu, F., Cao, L., Luo, P.G., Liu, J.H., Sahu, S., Tackett, K.N., Wang, Y. and Sun, Y.P. (2011) 'Fullerenes for applications in biology and medicine', *Current Medicinal Chemistry*, vol. 18, 2045-2059.
- Appel, J., Bockhorn, H. and Frenklach, M. (2000) 'Kinetic modeling of soot formation with detailed chemistry and physics: laminar premixed flames of C2 hydrocarbons', *Combust. Flame*, vol. 121, 122-136.
- Balthasar, M. and Frenklach, M. (2005) 'Monte-Carlo simulation of soot particle coagulation and aggregation: The effect of a realistic size distribution', *Proc. Combust. Inst.*, vol. 30, 1467-1475.
- Bashyam, R. and Zelenay, P. (2006) 'A class of non-precious metal composite catalysts for fuel cells', *Nature*, 443, 63–66.
- Bhowmick, H. and Biswas, S.K. (2011) 'Relationship between physical structure and tribology of single soot particles generated by burning ethylene', *Tribol. Lett.*, vol. 44, 139-149.
- Bhowmick, H., Majumdar, S.K. and Biswas, S.K. (2011) 'Dry tribology and nanomechanics of gaseous flame soot in comparison with carbon black and diesel soot', *Proc. IMechE Part C: J. Mechanical Engineering Science*, vol. 226, 2, 394-402.
- Bittner, J.D. and Howard, J.B. (1981) 'Composition profiles and reaction mechanisms in a near-sooting premixed benzene/oxygen/argon flame', *Symposium (International) on Combustion*, vol. 18, 1105-1116.
- Blanquart, G. and Pitsch, H. (2009) 'Analyzing the effects of temperature on soot formation with a joint volume-surface-hydrogen model', *Combustion and Flame*, vol. 156, 1614-1626.
- Bockhorn, H. (1994) *Soot formation in combustion -Mechanisms and models*, Alemania: Springer- Verlag.
- Bockhorn, H., D'Anna, A., Sarofim, A.F. and Wang, H. (2007) *International Workshop on Combustion Generated Fine Carbonaceous Particles*, Anacapri, Italy.

- Brenner, D.W., Shenderova, O.A., Harrison, J.A., Stuart, S.J., Ni, B. and Sinnott, S.B. (2002) 'A second-generation reactive empirical bond order (REBO) potential energy expression for hydrocarbons', *J Physics: Condensed Matter*, vol. 14, 783-802.
- Cain, J.P., Camacho, J., Phares, D.J., Wang, H. and Laskin, A. (2011) 'Evidence of aliphatics in nascent soot particles in premixed ethylene flames', *Proceeding of The combustion Institute*, vol. 33, 533–540.
- Cain, J.P., Gassman, P.L., Wang, H. and Laskin, A. (2010) 'Micro-FTIR study of soot chemical composition - Evidence of aliphatic hydrocarbons on nascent soot surfaces', *Physical Chemistry Chemical Physics*, vol. 12, 5206-5218.
- Camenzind, A., Caseri, W.R. and Pratsinis, S.E. (2010) 'Flame-made nanoparticles for nanocomposites', *Nano Today*, vol. 5, 48-65.
- Car, R. and Parrinello, M. (1985) 'Unified approach for molecular dynamics and density-functional theory', *Phys. Rev. Lett.*, vol. 55, 2471–2474.
- Castaldi, M.J., Marinov, N.M., Melius, C.F., Huang, J., Senkan, S.M., Pit, W.J. and Westbrook, C.K. (1996) 'Experimental and modeling investigation of aromatic and polycyclic aromatic hydrocarbon formation in a premixed ethylene flame', *Symposium (International) on Combustion*, vol. 26, 693-702.
- Chen, Y., Shah, N., Braun, A., Huggins, F.E. and Huffman, G.P. (2005) 'Electron microscopy investigation of carbonaceous particulate matter generated by combustion of fossil fuels', *Energy Fuels*, vol. 19, 1644–1651.
- Choi, B.C. and Foster, D.E. (2006) 'Overview of the effect of catalyst formulation and exhaust gas compositions on soot oxidation in DPF', *Journal of Mechanical Science and Technology*, vol. 20, 1-12.
- Chung, S.H. and Violi, A. (2007) 'Insights on the nanoparticle formation process in counterflow diffusion flames', *Carbon*, 45, 2400–2410.
- Chung, S.H. and Violi, A. (2010) 'Nucleation of fullerenes as a model for examining the formation of soot', *J. Chem. Phys.*, 132, 174502.
- Chung, S.H. and Violi, A. (2011) 'Peri-condensed aromatics with aliphatic chains as key intermediates for the nucleation of aromatic hydrocarbons', *Proc. Combust. Inst.*, 33, 693-700.
- Ciajolo, A., Barbella, R., Tregrossi, A. and Bonfanti, L. (1998) 'Spectroscopic and compositional signatures of pah-loaded mixtures in the soot inception region of a premixed ethylene flame', *Symposium (International) on Combustion.*, vol. 27, 1481–1487.
- Ciajolo, A., D'Anna, A. and Barbella, R. (1994) 'PAH and high molecular weight species formed in a premixed methane flame', *Combust. Sci. Technol.*, vol. 100, 271–281.
- Ciajolo, A., D'anna, A., Barbella, R. and Tregrossi, A. (1994) 'The formation of aromatic carbon in sooting ethylene flames', *Symposium (International) on Combustion*, vol. 25, 679-685.

- Colket, M.B. and Seery, D.J. (1994) 'Reaction mechanisms for toluene pyrolysis', *Symposium (International) on Combustion*, vol. 25, 883-891.
- Commodo, M., De Falco, G., Bruno, A., Borriello, C., Minutolo, P. and D'anna, A. (2015) 'Physicochemical evolution of nascent soot particles in a laminar premixed flame: from nucleation to early growth', *Combust. Flame*, vol. 162, 10, 3854-3863.
- Commodo, M., Violi, A., D'anna, A., D'alessio, A., Allouis, C., Beretta, F. and Minutolo, P. (2007) 'Soot and nanoparticle formation in laminar and turbulent flames', *Comb. Sci. Technol.*, vol. 179, 387-400.
- Cooke, W.F. and Wilson, J.J.N. (1996) 'A global black carbon aerosol model', *J. Geophys. Res.*, vol. 101, D14, 19395 – 19409.
- CRECK Modeling Group Polimi (2017), available: <http://creckmodeling.chem.polimi.it/menu-kinetics/menu-kinetics-detailed-mechanisms>.
- D'Alessio, A., Barone, A.C., Cau, R., D'Anna, A. and Minutolo, P. (2005) 'Surface deposition and coagulation efficiency of combustion generated nanoparticles in the size range from 1 to 10 nm', *Proceeding of the Combustion Institute*, vol. 30, 2, 2595-2603.
- D'Alessio, A., D'Anna, A., D'Orsi, A., Minutolo, P., Barbella, R. and Ciajolo, A. (1992) 'Precursor formation and soot inception in premixed ethylene flames', *Proc. Combust Inst.*, vol. 24, 973-980.
- D'Anna, A. (2008) 'Detailed kinetic modeling of particulate formation in rich premixed flames of ethylene', *Energy Fuels*, vol. 22, 1610-1619.
- D'Anna, A. (2009a) 'Combustion-formed nanoparticles', *Proc. Comb. Inst.*, vol. 32, 593-613.
- D'Anna, A. (2009b) 'Particle inception and growth: experimental evidences and a modelling attempt', in *Combustion generated fine carbonaceous particle*, Karlsruhe: KIT Scientific Publication.
- D'Anna, A., Commodo, M., Sirignano, M., Minutolo, P. and Pagliara, R. (2009) 'Particle formation in opposed-flow diffusion flames of ethylene: An experimental and numerical study', *Proceedings of the Combustion Institute*, vol. 32, 793-801.
- D'Anna, A. and Kent, J. (2008) 'A model of particulate and species formation applied to laminar, nonpremixed flames for three aliphatic-hydrocarbon fuels', *Combust. Flame*, vol. 152, 573-587.
- D'Anna, A., Violi, A., A., D. and Sarofim, A.F. (2001) 'A reaction pathway for nanoparticle formation in rich premixed flames', *Combust. Flame*, vol. 127, 1995-2003.
- D'Anna, A., Violi, A. and D'Alessio, A. (2000) 'Modeling the rich combustion of aliphatic hydrocarbons', *Combust. Flame.*, vol. 121, 418-429.
- Darden, T., York, D. and Pedersen, L. (1993) 'Particle mesh Ewald: An $N \cdot \log(N)$ method for Ewald sums in large systems', *J. Chem. Phys.*, vol. 98, 10089-10092.

- De Candia, A., Del Gado, E., Fierro, A., Sator, N. and Coniglio, A. (2005) 'Colloidal gelation, percolation and structural arrest', *Physica A: Statistical Mechanics and its Applications*, 358, 239–248.
- De Falco, G., Commodo, M., Minutolo, P. and D'Anna, A. (2015) 'Flame-Formed Carbon Nanoparticles: Morphology, Interaction Forces, and Hamaker Constant from AFM', *Aerosol. Sci. Tech.*, vol. 49, 281–289.
- Deutsch, T. and Genovese, L. (2011) 'Wavelets for electronic structure calculations', *Collect. SFN*, vol. 12, 33 - 76.
- Dobbins, R.A. (2007) 'Hydrocarbon nanoparticles formed in flames and diesel engines', *Aerosol Sci. Technol.*, vol. 41, 5, 485-496.
- Dobbins, R.A., Govatzidakis, G.J., Lu, W., Schwartzman, A.F. and Fletcher, R.A. (1996) 'Carbonization rate of soot precursor particles', *Combustion science and technology*, vol. 121, 103-121.
- Dobbins, R.A. and Megaridis, C.M. (1987) 'Morphology of flame-generated soot as determined by thermophoretic sampling', *Langmuir*, vol. 3, 254-259.
- Donchev, A.G. (2006) 'Ab initio quantum force field for simulations of nanostructures', *Physical Review B - Condensed Matter and Materials Physics*, vol. 74, 235401.
- Echavarria, C.A., Jaramillo, I.C., Sarofim, A.F. and Lighty, J.S. (2011) 'Studies of soot oxidation and fragmentation in a two-stage burner under fuel-lean and fuel-rich conditions', *Proc. Combust. Inst.*, vol. 33, 659-666.
- EEA (2015) 'Air Quality in Europe', *European Environment Agency*, Report No 5/2015.
- Frenklach, M. (2002) 'Reaction mechanism of soot formation in flames', *Physical Chemistry Chemical Physic*, vol. 4, 2028-2037.
- Frenklach, M., Bowman, T., Smith, G. and Gardiner Jr, W.C. (2011) *GRI-Mech Home Page*, [Online], Available: <http://combustion.berkeley.edu/gri-mech/>.
- Frenklach, M., Clary, D.W., Gardiner Jr, W.C. and Stein, S.E. (1985) 'Detailed kinetic modeling of soot formation in shock-tube pyrolysis of acetylene', *Symposium (International) on Combustion*, vol. 20, 887-901.
- Frenklach, M. and Harris, S.J. (1987) 'Aerosol dynamics modeling using the method of moments', *Journal of Colloid and Interface Science*, vol. 118, 1, 252-261.
- Frenklach, M., Moriarty, N.W. and Brown, N.J. (1998) 'Hydrogen migration in polyaromatic growth', *Symposium (International) on Combustion*, vol. 27, 1655-1661.
- Frenklach, M. and Wang, H. (1991) 'Detailed modeling of soot particle nucleation and growth', *Symposium (International) on Combustion*, vol. 23, 1559-1566.
- Frenklach, M. and Wang, H. (1994) 'Detailed mechanism and modeling of soot particle formation', *Symposium (International) on Combustion*, vol. 28, 1565-1571.

- Frenklach, M., Yuan, T. and Ramachandra, M.K. (1988) 'Soot formation in binary hydrocarbon mixtures', *Energy and Fuels*, vol. 2, 462-480.
- González, M.A. (2011) 'Force fields and molecular dynamics simulations', *Collection SFN*, vol. 12, 169–200.
- Gorbunov, B., Baklanov, A., Kakutkina, N., Windsor, H.L. and Toumi, R. (2001) 'Ice nucleation on soot particles', *J. Aerosol Sci.*, vol. 32, 199– 215.
- Gratzel, M. (2003) 'Dye-sensitized solar cells', *J. Photochem. Photobiol. C: Photo- chem. Rev.*, 4, 145-153.
- Grotheer, H.H., Pokorny, H., Barth, K.L., Thierley, M. and Aigner, M. (2004) 'Mass spectrometry up to 1 million mass units for the simultaneous detection of primary soot and of soot precursors (nanoparticles) in flames', *Chemosphere*, vol. 57, 124, 1335-1342.
- Grotheer, H.H., Wolf, K. and Hoffmann, K. (2011) 'Photoionization mass spectrometry for the investigation of combustion generated nascent nanoparticles and their relation to laser induced incandescence', *Applied Physics B: Lasers and Optics*, vol. 104, 367-383.
- Hansen, J. and Nazarenko, L. (2004) 'Soot climate forcing via snow and ice albedos', *Proc. Natl. Acad. Sci. USA*, vol. 101, 423–428.
- Harris, S.J. and Maricq, M.M. (2002) 'The role of fragmentation in defining the signature size distribution of diesel soot', *Journal of Aerosol Science*, vol. 33, 935-942.
- Haynes, B.S. and Wagner, H.G. (1981) 'Soot formation', *Prog. Energy Combust. Sci.*, vol. 7, 4, 229-273.
- Herdman, J.D. and Miller, J.H. (2008) 'Intermolecular potential calculations for polynuclear aromatic hydrocarbon clusters', *J. Phys. Chem. A*, vol. 112, 6249–6256.
- Hess, B., Kutzner, C., Van Der Spoel, D. and Lindahl, E. (2008) 'GROMACS 4: algorithms for highly efficient, load-balanced, and scalable molecular simulation', *J. Chem. Theory Comput.*, 4, 435-447.
- Homann, K.H. (1998) 'Fullerenes and soot formation - New pathways to large particles in flames', *Angewandte Chemie - International Edition*, vol. 37, 2434-2451.
- Horvath, H. (1993) 'Atmospheric light absorption—A review', *Atmos. Environ. A*, vol. 27, 293– 317.
- Howard, J.B. (1991) 'Carbon addition and oxidation reactions in heterogeneous combustion and soot formation', *Proc. Combust. Inst.*, vol. 23, 1107-1127.
- Iavarone, S., Pascazio, L., Sirignano, M., De Candia, A., Fierro, A., De Arcangelis, L. and D'Anna, A. (2017) 'Molecular dynamics simulations of incipient carbonaceous nanoparticle formation at flame conditions', *Combust. Theor. Model.*, 21, 49-61.
- Iijima, S. (1991) 'Helical microtubules of graphitic carbon', *Nature*, vol. 354, 56-58.

- Ishiguro, T., Takatori, Y. and Akihama, K. (1997) 'Microstructure of diesel soot particles probed by electron microscopy: first observation of inner core and outer shell', *Combust. Flame*, vol. 108, 231-234.
- Iwashita, N. and Swain, M.V. (n.d) 'Elasto-plastic deformation of glassy carbon by nano-indentation with spherical tipped indenters', *Mol. Cryst. Liq. Cryst.*, vol. 386, 39-44.
- Jang, Y.J., Simer, C. and Ohm, T. (2006) *Mater. Res. Bull.*, vol. 41, 67-77.
- Janowski, T., Ford, A. and Pulay, P. (2010) 'Accurate correlated calculation of the intermolecular potential surface in the coronene dimer', *Molecular Physics*, vol. 108, 249-257.
- Janowski, T. and Pulay, P. (2007) 'High accuracy benchmark calculations on the benzene dimer potential energy surface', *Chemical Physics Letters*, vol. 447, 1-3, 27-32.
- Kaminski, G., Friesner, R.A., Tirado-Rivers, J. and Jorgensen, W.L. (2001) 'Evaluation and reparametrization of the OPLS-AA force field for proteins via comparison with accurate quantum chemical calculations on peptides', *J. Phys. Chem. B*, 105, 6474-6487.
- Karcher, B. (1999) 'Aviation-produced aerosols and contrails', *Survey Geophys.*, vol. 20, 2, 113-167.
- Kay, A. and Gratzel, M. (1996) 'Low cost photovoltaic modules based on dye sensitized nanocrystalline titanium dioxide and carbon powder', *Solar Energy Mater. Solar Cells*, 44, 99-117.
- Kazakov, A., Wang, H. and Frenklach, M. (1995) 'Detailed modeling of soot formation in laminar premixed ethylene flames at a pressure of 10 bar', *Combustion and Flame*, vol. 100, 111-120.
- Kazakov, A., Wang, H. and Frenklach, M. (1995) 'Detailed modeling of soot formation in laminar premixed ethylene flames at a pressure of 10 bar', *Combust. Flame*, vol. 100, 111-120.
- Kennedy, I.M. (2007) 'The health effects of combustion-generated aerosols', *Proc. Combust. Inst.*, vol. 31, 2, 2757-2770.
- Koch, T. and Seidler, S. (2009) 'Correlations between indentation hardness and yield stress in thermoplastic polymers', *Strain*, vol. 45, 26-33.
- Kroto, H.W., Heath, J.R., O'Brien, S.C., Curl, R.F. and Smalley, E. (1985) 'C₆₀: Buckminsterfullerene', *Nature*, vol. 318, 162-163.
- Kubicki, J.D. (2006) 'Molecular simulations of benzene and PAH interactions with soot', *Environmental Science and Technology*, vol. 40, 2298-2303.
- Kumfer, B. and Kennedy, I. (2009) 'The Role of Soot in the Health Effects of Inhaled Airborne Particles', in *Combustion Generated Fine Carbonaceous Particles*, Karlsruhe, Germany: KIT Scientific Publishing, pp. 1-15.
- Li, J., Kazakov, A. and Dryer, F.L. (2004) 'Experimental and numerical studies of ethanol decomposition reactions', *Journal of Physical Chemistry A*, vol. 108, 7671-7680.

- Lin, H. and Truhlar, D.G. (2007) 'QM/MM: What have we learned, where are we, and where do we go from here?', *Theor. Chem. Acc.*, vol. 117, 185-199.
- Madler, L., Gurlo, A., Barsan, N., Pratsinis, S.E., Weimar, U. and Sahm, T. (2004) 'Flame spray synthesis of tin dioxide nanoparticles for gas sensing', *Sens. Actuators B*, vol. 98, 148-153.
- Maricq, M.M. (2004) 'Size and charge of soot particles in rich premixed flames', *Combust. Flame*, vol. 137, 340-350.
- Marinov, N.M., Pitz, W.J., Westbrook, C.K., Vincitore, A.M., Castaldi, M.J., Senkan, S.M. and Melius, C.F. (1998) 'Aromatic and polycyclic aromatic hydrocarbon formation in a laminar premixed n-butane flame', *Combustion and Flame*, vol. 114, 192-213.
- Martin, R.M. (2004) 'Electronic structure: Basic theory and practical methods', *Cambridge University Press*.
- Martínez, L., Andrade, R., Birgin, E.G. and Martínez, J.M. (2009) 'PACKMOL: A package for building initial configurations for molecular dynamics simulations', *J. Comp. Chem.*, vol. 30, 13, 2157-2164.
- Mauss, F., Schafer, T. and Bockhorn, H. (1994) 'Inception and growth of soot particles in dependence on the surrounding gas phase', *Combust.Flame*, vol. 99, 697-705.
- McConnell, J.R., Edwards, R., Kok, G.L. and al., e. (2007) '20th-century industrial black carbon emissions altered arctic climate forcing', *Science*, vol. 317, 1381-1384.
- Melius, C.F., Colvin, M.E., Marinov, N.M., Pit, W.J. and Senkan, S.M. (1996) 'Reaction mechanisms in aromatic hydrocarbon formation involving the C₅H₅ cyclopentadienyl moiety', *Symposium (International) on Combustion*, vol. 26, 685-692.
- Memon, N.K., Tse, S.D., Chhowalla, M. and Kear, B.H. (2013) 'Role of substrate, temperature, and hydrogen on the flame synthesis of graphene films', *Proc. Combust. Inst.*, vol. 34, 2163-2170.
- Messerer, A., Niessner, R. and Poschl, U. (2006) 'Comprehensive kinetic characterization of the oxidation and gasification of model and real diesel soot by nitrogen oxides and oxygen under engine exhaust conditions: Measurement, Langmuir-Hinshelwood, and Arrhenius parameters', *Carbon*, vol. 44, 307-324.
- Metropolis, N., Rosenbluth, A.W., Rosenbluth, M.N., Teller, A.H. and Teller, E. (1953) 'Equation of state calculations by fast computing machines', *J. Chem. Phys.*, vol. 21, 1087-1092.
- Miller, J.H. (1991) 'The kinetics of polynuclear aromatic hydrocarbon agglomeration in flames', *Symposium (International) on Combustion*, vol. 23, 91-98.
- Miller, J.H., Mallard, W.G. and Smyth, K.C. (1984) 'Intermolecular potential calculations for polycyclic aromatic hydrocarbons', *J. Phys. Chem.*, vol. 88, 4963-4970.

- Miller, J.H. and Melius, C.F. (1992) 'The reactions of imidogen with nitric oxide and molecular oxygen', *Symposium (International) on Combustion*, vol. 24, 719-726.
- Miller, J.H., Smyth, K.C. and Mallard, W.G. (1985) 'Calculations of the dimerization of aromatic hydrocarbons: Implications for soot formation', *Symposium (International) on Combustion*, vol. 20, 1, 1139-47.
- Minutolo, P., Commодо, M., Santamaria, A., De Falco, G. and D'Anna, A. (2014) 'Characterization of flame-generated 2-D carbon nano-disks', *Carbon*, vol. 68, 138-148.
- Minutolo, P., D'anna, A., Commодо, M., Pagliara, R., Toniato, G. and Accordini, C. (2008) 'Emission of ultrafine particles from natural gas domestic burners', *Environmental Engineering Science*, vol. 25, 1357-1363.
- Mitchell, P. and Frenklach, M. (1998) 'Monte carlo simulation of soot aggregation with simultaneous surface growth-why primary particles appear spherical', *Symposium (International) on Combustion*, vol. 27, 1507-1514.
- Mohan, and Manoj, B. (2012) 'Synthesis and characterization of carbon nanospheres from hydrocarbon soot', *Int. J. Electrochem. Sci.*, vol. 7, 9537.
- Mohan, A.N. and Manoj, B. (2017) 'Exploration of carbon nano dots in hydro carbon soot and carbon black', *Res. J. Chem. Environ.*, vol. 21, 1-6.
- Moriarty, N.W., Brown, N.J. and Frenklach, M. (1999) 'Hydrogen migration in the phenylethen-2-yl radical', *Journal of Physical Chemistry A.*, vol. 103, 7127-7135.
- Mosbach, S., Celnik, M.S., Raj, A., Kraft, M., Zhang, H.R., Kubo, S. and et al. (2009) 'Towards a detailed soot model for internal combustion engines', *Combustion and Flame*, vol. 156, 1156-1165.
- Neoh, K.G., Howard, J.B. and Sarofim, A.F. (1985) 'Effect of oxidation on the physical structure of soot', *Symposium (International) on Combustion*, vol. 20, 951-957.
- Nosè, S. (1984) 'A molecular dynamics method for simulations in the canonical ensemble', *Mol. Phys.*, 52, 255-268.
- Novoselov, K.S., Geim, A.K., Morozov, S.V., Jiag, D., Katsnelson, M.I., Grigirieva, I.V., Dubunos, S.V. and Firsov, A.A. (2005) 'Two-dimensional gas of massless Dirac fermions in graphene', *Nature*, vol. 438, 197-200.
- O'Connor, T.C., Andzelm, J. and Robbins, M.O. (2015) 'AIREBO-M: A reactive model for hydrocarbons at extreme pressures', *J. Chem. Phys.*, vol. 142, 024903.
- Oberdörster, G., Oberdörster, E. and Oberdörster, J. (2005) 'Nanotoxicology: An Emerging Discipline Evolving from Studies of Ultrafine Particles', *Environ Health Perspect.*, vol. 113, 7, 823-839.
- Oregan, B. and Gratzel, M. (1991) 'A low-cost, high-efficiency solar cell based on dye-sensitized colloidal TiO₂ films', *Nature*, 353, 737– 740.

- Osunsanya, T., Prescott, G. and Seaton, A. (2001) 'Acute respiratory effects of particles: mass or number?', *Occup. Environ. Med.*, vol. 58, 3, 154-159.
- Palotas, A.B., Rainey, L.C., Feldermann, C.J., Sarofim, A.F. and Vander Sande, J.B. (1996) 'Soot morphology: an application of image analysis in high-resolution transmission electron microscopy', *Microsc. Res. Tech.*, vol. 33, 266-278.
- Patterson, J.R., Catledge, S.A., Vohra, Y.K., Akella, J. and Weir, S.T. (2000) 'Electrical and mechanical properties of C70 fullerene and graphite under high pressures studied using designer diamond anvils', *Phys Rev Lett.*, vol. 85, 25, 5364-5367.
- Plimpton, A. (1995) 'Fast parallel algorithms for short-range molecular dynamics', *J. Comp. Phys.*, vol. 117, 1-19, Available: <http://lammps.sandia.gov>.
- Podeszwa, R., Bukowski, R. and Szalewicz, K. (2006) 'Potential energy surface for the benzene dimer and perturbational analysis of π - π interactions', *The Journal of Physical Chemistry A*, vol. 110, 34, 10345-10354.
- Podeszwa, R. and Szalewicz, K. (2008) 'Physical origins of interactions in dimers of polycyclic aromatic hydrocarbons', *Phys. Chem. Chem. Phys.*, vol. 10, 2735-2746.
- Pope, C.J. and Howard, J.B. (1997) 'Simultaneous particle and molecule modeling (SPAMM): an approach for combining sectional aerosol equations and elementary gas-phase reactions', *Aerosol Science and Technology*, vol. 27, 1, 73-94.
- Pope, C.J., Marr, J.A. and Howard, J.B. (1993) 'Chemistry of fullerenes C60 and C70 formation in flames', *Journal of Physical Chemistry*, vol. 97, 11001-11013.
- Pratsinis, S.E. (1998) 'Flame aerosol synthesis of ceramic powders', *Prog. Energy Combust. Sci.*, vol. 24, 197-219.
- Puri, R., Richardson, T.F., Santoro, R.J. and Dobbins, R.A. (1993) 'Aerosol dynamic processes of soot aggregates in a laminar ethene diffusion flame', *Combust. Flame*, vol. 92, 320-333.
- Raj, A., Sander, M., Janardhanan, V. and Kraft, M. (2010) 'A study on the coagulation of polycyclic aromatic hydrocarbon clusters to determine their collision efficiency', *Combustion and Flame*, vol. 157, 3, 523-534.
- Rapacioli, M., Calvo, F., Spiegelman, F., Joblin, C. and Wales, D.J. (2005) 'Stacked clusters of polycyclic aromatic hydrocarbon molecules', *J. Phys. Chem. A*, vol. 109, 2487-2497.
- Remer, L.A., Chin, M., Decola, P., Feingold, G., Halthore, R. and Kahn, R.A. (2009) 'Executive summary in atmospheric aerosol properties and climate impacts'.
- Richter, H., Granata, S., Green, W.H. and Howard, J.B. (2005) 'Detailed modelling of PAH and soot formation in a laminar premixed benzene/oxygen/argon low-pressure flame', *Proc. Combust. Inst.*, vol. 30, 1397-1405.

- Richter, H. and Howard, J.B. (2000) 'Formation of polycyclic aromatic hydrocarbons and their growth to soot-a review of chemical reaction pathways', *Progress in Energy and Combustion Science*, vol. 26, 565-608.
- Richter, A., Riesa, R., Smith, R., Henkel, M. and Wolf, B. (2000) 'Nanoindentation of diamond, graphite and fullerene films', *Diamond and Related Materials*, vol. 9, 170-184.
- Sabbah, H., Biennier, L., Klippenstein, S.J., Sims, I.R. and Rowe, B.R. (2010) 'Exploring the role of PAHs in the formation of soot: Pyrene dimerization', *Journal of Physical Chemistry Letters*, vol. 1, 2962-2967.
- Sayle, R. and Milner-White, J. (1995) 'RASMOL: biomolecular graphics for all', *Trends Biochem. Sci.*, vol. 20, 374.
- Schuetz, C.A. and Frenklach, M. (2002) 'Nucleation of soot: Molecular dynamics simulations of pyrene dimerization', *Proc. Combust. Inst.*, vol. 29, 2307-2314.
- Seipenbusch, M., Erven, J.V., Schalow, T., Weber, A.P., Langeveld, A.D.V., Marijnissen, J.C.M. and Friedlander, S.K. (2005) 'Catalytic soot oxidation in microscale experiments', *Applied Catalysis B: Environmental*, vol. 55, Marijnissen, J. C. M. & Friedlander, S. K., 31-37.
- Service, R.F. (2008) 'Climate change. Study fingers soot as a major player in global warming', *Science*, vol. 319, 1745.
- Sgro, L.A., De Filippo, A., Lanzuolo, G. and D'Alessio, A. (2007) 'Characterization of nanoparticles of organic carbon (NOC) produced in rich premixed flames by differential mobility analysis', *Proc. Combust. Inst.*, vol. 31, 1, 631-638.
- Shaddix, C.R., Harrington, J.E. and Smyth, K.C. (1994) 'Quantitative measurements of enhanced soot production in a flickering methane/air diffusion flame', *Combustion and Flame*, vol. 99, 723-732.
- Shaddix, C.R. and Smyth, K.C. (1996) 'Laser-induced incandescence measurements of soot production in steady and flickering methane, propane, and ethylene diffusion flames', *Combustion and Flame*, vol. 107, 418-452.
- Sheen, D.A., You, X., Wang, H. and Lovas, T. (2009) 'Spectral uncertainty quantification, propagation and optimization of a detailed kinetic model for ethylene combustion', *Proceedings of the Combustion Institute*, 535-542.
- Sirignano, M., Kent, J.H. and D'Anna, A. (2010) 'Detailed modeling of size distribution functions and hydrogen content in combustion-formed particles', *Combust. Flame*, vol. 157, 1211-1219.
- Sirignano, M., Kent, J. and D'Anna, A. (2010) 'Detailed modeling of size distribution functions and hydrogen content in combustion-formed particles', *Combustion and Flame*, vol. 157, 1211-1219.
- Smoluchowski, M.V. (1916) 'Drei Vortrage uber Diffusion, Brownsche Bewegung und Koagulation von Kolloidteilchen', *Physik. Zeit*, vol. 17, 557-585.

- SRI International (2001) *Chemical Economics Handbook*, Merlo Park.
- Stark, W.J. and Pratsinis, S.E. (2002) 'Aerosol flame reactors for manufacture of nanoparticles', *Powd. Technol.*, vol. 126, 103-108.
- Stein, S.E. and Fahr, A. (1985) 'High temperature stabilities of hydrocarbons', *Journal of Physical Chemistry*, vol. 82, 3714-3725.
- Stein, S.E. and Fahr, A. (1985) 'High-temperature stabilities of hydrocarbons', *Journal of Physical Chemistry*, vol. 89, 17, 3714-3725.
- Stewart, J.J.P. (1989a) 'Optimization of parameters for semiempirical methods I. Method.', *Journal of Computational Chemistry*, 10(2):, vol. 10, 2, 209-220.
- Stewart, J.J.P. (1989b) 'Optimization of parameters for semiempirical methods II. Applications', *J. Comp. Chem.*, vol. 10, 221-264.
- Stuart, S.J., Tutein, A.B. and Harrison, J.A. (2000) 'A reactive potential for hydrocarbons with intermolecular interactions', *J. Chem. Phys.*, vol. 112, 6472-6486.
- Teleki, A., Pratsinis, S.E., Kalyanasundaram, K. and Gouma, P.I. (2006) 'Sensing of organic vapors by flame-made TiO₂ nanoparticles', *Sens. Actuators B*, vol. 119, 683-690.
- Tersoff, J. (1988) 'New empirical approach for the structure and energy of covalent systems', *Phys Rev B*, vol. 37, 6991.
- Thompson, B.C. and Fréchet, J.M.J. (2008) 'Polymer-fullerene composite solar cells', *Angewandte Chemie - International Edition*, vol. 47, 58-77.
- Totton, T.S., Chakrabarti, D., Misquitta, A.J., Sander, M., Wales, D.J. and Kraft, M. (2010) 'Modelling the internal structure of nascent soot particles', *Combust. Flame*, vol. 157, 909-914.
- Totton, T.S., Misquitta, A.J. and Kraft, M. (2010) 'A first principles development of a general anisotropic potential for polycyclic aromatic hydrocarbons', *Chem. Theory Comp.*, vol. 6, 683-695.
- Totton, T.S., Misquitta, A.J. and Kraft, M. (2011) 'A transferable electrostatic model for intermolecular interactions between polycyclic aromatic hydrocarbons', *Chem. Phys. Lett.*, vol. 510, 154-160.
- Totton, T.S., Misquitta, A.J. and Kraft, M. (2012) 'A quantitative study of the clustering of polycyclic aromatic hydrocarbons at high temperatures', *Phys. Chem. Chem. Phys.*, 14, 4081-4094.
- Ulrich, G.D. (1984) 'Flame synthesis of fine particles', *Chem. Eng. News.*, vol. 62, 32, 22-29.
- Van de Waal, B.W. (1983) 'Calculated ground-state structures of 13-molecule clusters of carbon dioxide, methane, benzene, cyclohexane, and naphthalene', *J. Chem. Phys.*, vol. 79, 3948-3961.
- van Duin, A.C.T., Dasgupta, S., Lorant, F. and Goddard III., W.A. (2001) 'ReaxFF: A reactive force field for hydrocarbons', *J. Phys. Chem. A*, vol. 105, 9396-9409.

- Vander Wal, R.L. (2000) 'Flame synthesis of substrate-supported metal-catalyzed carbon nanotubes', *Chemical Physics Letters*, vol. 324, 217-223.
- Vander Wal, R.L., Yezerets, A., Currier, N.W., Kim, D.H. and Wang, C.M. (2007) 'HRTEM Study of diesel soot collected from diesel particulate filters', *Carbon*, vol. 45, 1, 70-77.
- Vander Wal, R.L. and Tomasek, A.J. (2003) 'Soot oxidation: Dependence upon initial nanostructure', *Combustion and Flame*, vol. 134, 1-9.
- Verlet, L. (1967) 'Computer "experiments" on classical fluids. I. Thermodynamical properties of Lennard-Jones molecules', *Phys. Rev.*, 159, 98.
- Wagner, H.G. (1979) 'Soot formation in combustion', Seventeenth Symposium (International) on Combustion, Leeds, England, 3-19.
- Wang, H. (2011) 'Formation of nascent soot and other condensed-phase materials in flame', *Proc. Comb. Inst.*, vol. 33, 41-67.
- Wang, H. and Frenklach, M. (1997) 'A detailed kinetic modeling study of aromatics formation in laminar premixed acetylene and ethylene flames', *Combust. Flame*, vol. 110, 173-221.
- Whitby, K.T. (1978) 'The physical characterization of sulfur aerosols', *Atmospheric Environment*, vol. 12, 135-159.
- WHO (2014) *Ambient (outdoor) air quality and health Fact Sheet N°313*, World Health Organization, Updated March 2014, [Online], Available: <http://www.who.int/mediacentre/factsheets/fs313/en/>.
- Williams, D.E. and Starr, T.L. (1977) 'Calculation of the crystal structures of hydrocarbons by molecular packing analysis', *Comput. Chem.*, vol. 1, 173-177.
- Wong, D., Whitesides, R., Schuertz, C.A. and Frenklach, M. (2009) 'Molecular dynamics simulations of PAH dimerization', in Bockhorn, H..D.A..S.A.F..W.H. *Combustion Generated Fine Carbonaceous Particles*, Karlsruhe: KIT Scientific Publishing, pp. 247-257.
- Yazyev, O.V. and Louie, S.G. (2010) 'Electronic transport in polycrystalline graphene', *Nature Materials*, vol. 9, 806-809.
- Zhang, P., Li, S.X. and Zhang, Z.F. (2011) 'General relationship between strength and hardness', *Materials Science and Engineering A*, vol. 529, 62– 73.
- Zhao, B., Uchikawa, K. and Wang, H. (2007) 'A comparative study of nanoparticles in premixed flames by scanning mobility particle sizer, small angle neutron scattering, and transmission electron microscopy', *Proceedings of the Combustion Institute*, vol. 31, 1, 851-860.
- Zhao, B., Yang, Z., Johnston, M.V., Wang, H., Wexler, A.S., Balthasar, M. and Kraft, M. (2003) 'Measurement and numerical simulation of soot particle size distribution functions in a laminar premixed ethylene-oxygen-argon flame', *Combust. Flame*, vol. 133, 173-188.

Zickler, G.A., Schoberl, T. and Paris, O. (2006) 'Mechanical properties of pyrolysed wood: a nanoindentation study', *Philosophical Magazine*, vol. 86, 10, 1373–1386.